DOCTOR OF PHILOSOPHY

Preparation and characterisation of uranium and tungsten borides for applications in the nuclear industry

Martini, Fabio

Award date:
2023

Awarding institution:
Bangor University

Preparation and characterisation of uranium and tungsten borides for applications in the nuclear industry

Candidate

Fabio Martini

Supervisor

Prof. Simon Middleburgh

I hereby declare that this work has not been accepted for any award and is not being submitted concurrently for any award unless as agreed by the University for approved dual awards.

I hereby declare that this thesis was submitted with the agreement of my Supervisor, Prof Simon Middleburgh.

I hereby declare that this thesis is the results of my own investigations, except where otherwise stated. All other sources are acknowledged by bibliographic references. This work has not previously been accepted in substance for any degree and is not being concurrently submitted in candidature for any degree unless, as agreed by the University, for approved dual awards.

Contents

Contents…… iii

List of figures vii

List of tables x

List of acronyms xii

Acknowledgments xiii

1. Summary 1

2. Introduction 3

2.1. Advanced Technology Fuels for fission reactors 3

2.1.1. ATFs: the neutronics approach 4

2.1.2. ATFs: the materials approach 6

2.1.3. Fuel materials combining high heavy metal density and high thermal conductivity 8

2.2. Uranium borides as materials for nuclear fuels for fission reactors 14

2.3. Synthesis of uranium borides 17

2.4. Scope of the thesis: building towards a concept for a UB_2-UO_2 composite fuel pellet 20

3. Methodology 22

3.1. Thermodynamic modelling 22

3.2. Estimation of a lower bound to the reaction time for chemical reactions with gaseous by-products 28

3.2.1. Example calculation 30

3.3. Density Functional Theory (DFT) simulations 31

3.4. Synthesis and characterisation of materials 40

3.4.1. Materials used 40

3.4.2. Preparation of reaction mixtures 40

3.4.3. Production of pellets 42

3.4.4. High-temperature synthesis 42

3.4.5. Analysis of materials through X-ray Diffraction (XRD) 46

3.4.6. Analysis of materials trough Thermo-Gravimetric Analysis (TGA) 48
3.4.7. Synthesis and characterisation of uranium dioxide 50
4. Modelling and experiments on the synthesis of uranium borides 53
4.1. Thermodynamic modelling: synthesis of uranium borides by the borocarbothermic reduction of UO_2 53
4.2. Thermodynamic modelling: synthesis of uranium borides by the direct conversion of uranium fluorides 55
4.2.1. Metallothermic reduction of solid UF_4 and BF_3 57
4.2.2. Hydrogen reduction of gaseous UF_6 and BF_3 58
4.2.3. Direct borothermic reduction of UF_6 with elemental boron 60
4.2.4. Reduction of UF_6 with B_2H_6 60
4.2.5. Remarks on the direct conversion of uranium fluorides into uranium borides 61
4.3. Experiments in the borocarbothermic synthesis of uranium borides from UO_2 62
4.3.1. Synthesis of UO_2-UB_4 mixtures at relatively high partial pressures of CO 62
4.3.2. Synthesis of UB_2 at relatively low partial pressures of CO 64
4.3.3. Synthesis of UB_4 by reaction of UO_2 with B_4C 68
4.3.4. Synthesis of UB_2 from the comproportionation of UO_2 and UB_4 69
4.3.5. Synthesis of UB_{12} 71
5. Modelling and experiments on the synthesis of tungsten borides 74
5.1. Thermodynamic modelling: synthesis of tungsten borides by the borocarbothermic reduction of tungsten oxides 75
5.2. Experiments in the borocarbothermic synthesis of WB_x from WO_3 78
5.2.1. Synthesis of W_2B 79
5.2.2. Synthesis of WB 80
5.2.3. Synthesis of W_2B_5 82
5.2.4. Considerations on the scale-up of the synthetic routes 83
6. Chemical interactions and burnup chemistry of UB_2 85
6.1. Thermodynamic model for the oxidation of UB_2 85

6.2. Volume change associated with the oxidation of UB_2 89
6.3. Simultaneous Thermal Analysis of the oxidation of UB_2 in flowing synthetic air 92
6.4. Assessment of the reactions of UB_2 upon contact with metals and ceramics 99
6.5. Burnup chemistry of UB_2 102
6.5.1. Alkali metals 107
6.5.2. Alkali-earth metals 107
6.5.3. Transition metals 108
6.5.4. Lanthanides 110
6.5.5. Actinides 110
6.5.6. *p*-group metals 111
6.5.7. Halogens 111
6.5.8. Hydrogen and noble gases 113
6.5.9. Systematic classification of irradiation products in UB_2 113
6.5.10. Chemical evolution of UB_2 with burnup 113
6.6. Synthesis of $(U,Zr)B_2$ solid solutions 116
6.7. Simulation of the thermal expansion of UB_2 121
7. Research and development needs 126
7.1. Simulations and modelling 127
7.1.1. Preliminary feasibility studies 127
7.1.2. Advanced modelling and integration of data from experiments and atomic-scale simulations 129
7.1.3. Modelling the front- and back-end of the fuel cycle 129
7.2. Fuel analysis and testing 130
7.2.1. Experiments on powders and sintered shapes of UB_2 130
7.2.2. Analysis of the UB_2 particles 131
7.2.3. Analysis and testing of the composite fuel pellet and of its manufacturing process . 132
7.3. Fuel manufacturing 132

7.3.1. Optimisation of the preparation of UB_2 and evaluation of its industrial scale-up 133
7.3.2. Manufacture of UB_2 and ZrB_2 kernels 135
7.3.3. Coating of kernels 137
7.3.4. Fabrication of composite pellets 139
7.3.5. Quality control and scrap recycling 140
8. Conclusions 141
Appendix A: tables of thermodynamic coefficients 142
References 145

List of figures

Figure 2.1: Calculated improvements in thermal conductivity at 1000 K (left) and uranium density (right) of UO_2 as a function of the volume fraction of dispersed kernels of UB_2, UN, and U_3Si_2. ... 13
Figure 2.2: Phase diagram of the B-U system ... 16
Figure 2.3: Conceptual representation of the proposed ATF pellet. ... 20
Figure 3.1: Typical free energy curves as a function of volume for a series of temperature (left) and V(T) curve, as generated by Phonopy. ... 36
Figure 3.2: Thermodynamic cycle used to calculate the standard enthalpy of formation. ... 37
Figure 3.3: Workflow of the DFT-QHA simulations. ... 39
Figure 3.4: The positive pressure glovebox. ... 41
Figure 3.5: The tube furnace. ... 43
Figure 3.6: The chamber furnace. ... 43
Figure 3.7: Calculated oxygen concentration and temperature profile in the tube furnace during purging and the initial heating phase of a typical run ... 45
Figure 3.8: The X-ray diffractometer. ... 48
Figure 3.9: The Simultaneous Thermal Analyser. ... 49
Figure 3.10: UO_{2+x} prepared from the hydrogen reduction of U_3O_8. ... 51
Figure 3.11: Diffraction pattern of a typical sample of reduced $UO_{2.05}$. ... 51
Figure 3.12: Mass profile of the UO_{2+x} sample (in green) and temperature (in red) during the TG analysis. ... 52
Figure 4.1: Predominance diagram of the thermodynamically stable condensed phases in a stoichiometric reaction mixture intended for the borocarbothermic synthesis of UB_2. ... 54
Figure 4.2: Mixture of UB_4 and UO_2, obtained after firing a reaction mixture intended for UB_2 in the tube furnace ... 63
Figure 4.3: XRD pattern of the grey solid recovered from the UB_2 synthesis attempt in the tube furnace ... 63
Figure 4.4: XRD pattern of the products of synthesis A. ... 65
Figure 4.5: XRD pattern of the products of synthesis B. ... 65
Figure 4.6: XRD pattern of the products of synthesis C ... 66
Figure 4.7: XRD pattern of the products of synthesis D ... 66
Figure 4.8: Typical sample of UB_2 with high purity ... 67
Figure 4.9: Typical sample of UB_2 with impurities of UO_2 ... 67

Figure 4.10: UB_4 (left, grey) and UO_2 (right, brick red) in the jar of the ball mill prior to mixing...70
Fig 4.11: XRD patterns of the products of the synthesis of UB_4 from UO_2 and B_4C (a) and of the synthesis of UB_2 from UO_2, B_4C, and C (b). 71
Figure 4.12: XRD pattern of the products of the UB_{12} synthesis attempt 73
Figure 5.1: Phase diagram of the W-B system....74
Figure 5.2: Equilibrium pressure of CO as a function of temperature for the carbothermic reduction of WO_3 to WO_2 and for the synthesis of W_2B, WB, and W_2B_5.....78
Figure 5.3: XRD pattern of the products of the synthesis of W_2B....79
Figure 5.4: XRD pattern of the products of the synthesis of WB after one firing. 81
Figure 5.5: XRD pattern of the powders resulting from the second heat treatment of the products of the WB synthesis.....82
Figure 5.6: XRD pattern of the products of the synthesis of W_2B_5. 83
Figure 6.1: Variation in Gibbs free energy for relevant reactions in the oxidation of UB_2. 86
Figure 6.2: Calculated composition change associated with the oxidation of UB_2 during its oxidation in oxygen-rich (a) and oxygen-poor (b) conditions 90
Figure 6.3: Calculated volume change associated with the oxidation of UB_2 in oxygen-rich and oxygen-poor conditions....92
Figure 6.4: Typical mass gain during the air oxidation of UB_2 fine powder and fragments. Inset shows oxidation onset temperatures determined from 5% of the final mass gain. 93
Figure 6.5: XRD pattern of the products of oxidation of UB_2. 94
Figure 6.6: DSC profiles during the oxidation of UB_2 fragments and fine powder up to 1173 K 95
Figure 6.7: 1^{st} derivatives of the mass gain profiles compared with the DSC profiles for the oxidation of UB_2 fragments and fine powder. 97
Figure 6.8: Mass gain during the oxidation of UB_2 fragments in air at different heating rates. 98
Figure 6.9: Fuel assembly geometry used in the burnup simulations....104
Figure 6.10: Variation in Gibbs free energy for the reactions of UB_2, Cs, and Rb with I_2 and Br_2 112
Figure 6.11: Estimated B/M ratio of the UB_2 matrix as a function of burnup for three different isotopic abundances of ^{11}B in UB_2....115
Figure 6.12: Detail of the (0 0 2) reflection in the XRD patterns of three $(U,Zr)B_2$ samples with varying Zr content. 118
Figure 6.13:Variations in the lattice parameters of the unit cell of $(U,Zr)B_2$ as a function of Zr content. 120

Figure 6.14: Potential energy surface of the UB_2 cell as a function of the lattice parameters at a temperature of 290 K. 124
Figure 7.1: Flowchart of the proposed pathway towards the evaluation and testing of a UO_2-UB_2 composite fuel. 126

List of tables

Table 2.1: Uranium density and thermal conductivity of several substances compared to UO_2. 9
Table 2.2: Reactions with oxygen, their variations in enthalpy (referred to O_2), and their equilibrium constants for selected uranium substances 10
Table 2.3: Abundances and properties of the two naturally-occurring isotopes of boron. 14
Table 2.4: Crystallographic properties of UB_2, UB_4, and UB_{12} 15
Table 2.5: Relevant properties of unirradiated UO_2, UB_2, UB_4, UB_{12}, and ZrB_2. 16
Table 3.1: Process and thermochemistry data for the sample calculation. 30
Table 3.2: Lattice parameters of the unscaled unit cells of UB_2 and of the resulting expanded supercells. 35
Table 3.3: Calculated standard molar enthalpy of formation and standard molar entropy at 298 K for UB_2 and UB_4 and literature values. 38
Table 3.4: Suppliers and purities of the materials used in the synthesis experiments. 40
Table 4.1: Relevant properties of some proposed reactants for the conversion of UF_6 into UB_2 57
Table 4.2: Composition of the reaction mixture for UB_2 and firing conditions over experiments A, B, C, and D. 64
Table 5.1: Crystallographic properties of W_2B, WB, and W_2B_5. 75
Table 6.1: Specific volume of relevant substances in the U-B-O system in their crystalline form 89
Table 6.2: Heat released and mass gain for two theoretical cases and for two sets of experiments in the oxidation of UB_2. 96
Table 6.3: Qualitative enthalpy change and spontaneity range of selected reactions of UB_2 with materials relevant to the nuclear industry. 99
Table 6.4: Main fission and transmutation products in UB_2 and their possible chemical forms and abundances. 105
Table 6.5: Classes of fission and transmutation products in UB_2 113
Table 6.6: Molar fraction of ZrB_2, time at temperature, purity, and other identified crystalline phases for the $(U,Zr)B_2$ samples 117
Table 6.7: Measured lattice parameters for the solid solution samples and for pure UB_2 and ZrB_2. 118
Table 6.8: Values of the reported and calculated coefficients of thermal expansion of UB_2. 125
Table A.1: thermodynamic coefficients used in the assessments, along with their literature sources. 142

Table A.2: thermodynamic coefficients for carbon (C) used in the assessments. 144
Table A.3: thermodynamic coefficients for uranium dioxide (UO_2) used in the assessments. 144

List of acronyms

AGR – Advanced Gas Reactor

ATF – Advanced Technology Fuel

BOL – Beginning Of Life

BWR – Boiling Water Reactor

CANDU – CANada Deuterium Uranium

CERCER – CERamic-CERamic

CERMET – CERamic-METallic

CSTR – Continuous-flow Stirred-Tank Reactor

CTE – Coefficient of Thermal Expansion

CVD – Chemical Vapour Deposition

DFT – Density Functional Theory

DSC – Differential Scanning Calorimetry

FBR – Fluidised Bed Reactor

I(F)BA – Integral (Fuel) Burnable Absorber

IDLH – Immediately Dangerous to Life and Health

IDR – Integrated Dry Route

LWR – Light Water Reactor

MS – Mass Spectrometry

PFR – Plug-Flow Reactor

PIE – Post-Irradiation Examination

PVD – Physical Vapour Deposition

PWR – Pressurised Water Reactor

QHA – Quasi-Harmonic Approximation

RBMK – Reaktor Bolshoy Moshchnost Kanalnyy (high-power channel-type reactor)

STA – Simultaneous Thermal Analyser

TGA – Thermo-Gravimetric Analysis

TRISO – TRistructural ISOtropic

VASP – Vienna Ab-Initio Simulation Package

XRD – X-Ray Diffractometry

Acknowledgments

This work was funded by the KESS 2 program and by Westinghouse Electric Sweden.

I am grateful to Prof Simon Middleburgh for supervision, guidance, and support.

I am grateful to Dr John Thomas Prabhakar, Dr Iuliia Ipatova, Mr David Williams, and Mr Ben Assinder for the care with which they tended to the laboratory.

I am grateful to Dr Michel Rushton, Dr Marcus Dahlfors, Dr Marat Margulis, Dr Lee Evitts, Dr Antoine Claisse, and Mr Mattias Puide for helpful discussion.

I am grateful to Dr Penny Dowdney, Dr Jon Tate, Ms Emily Robinson, Ms Sediqa Jalali and to the Bangor University Finance Offices for organisational support.

1. Summary

Metal borides are a class of refractory materials with a set of thermomechanical properties that make them well-suited for applications in extreme environments, most notably their high thermal conductivities and their high melting points. In addition to this, the unique nuclear properties of boron make metal borides interesting materials for the nuclear industry as well: boron has two naturally occurring isotopes, with one being a strong neutron absorber (and widely used in this role in the nuclear industry) and the other being substantially neutron-transparent, and with well-established supply chains for its isotopic separation.

Thus, metal borides represent a class of materials with adjustable neutron opacity and which are able to conduct and dissipate heat, including that which is generated inside their bulk by nuclear reactions, with potential applications as fuels or fuel additives for fission reactors, and for shielding materials for fusion reactors.

However, the most established route of preparation of many metal borides is still the direct reactive melting of boron and the respective base metal, in a process that – while conceptually simple – is usually energy-intensive and challenging to scale-up.

In this work, uranium and tungsten borides are discussed, respectively, for use in fission and fusion reactors, in particular uranium diboride (UB_2) and ditungsten pentaboride (W_2B_5). Uranium diboride is envisioned as a component for a composite Advanced Technology Fuel (ATF) concept in which UB_2 particles are dispersed in a UO_2 matrix to improve its thermal conductivity and its uranium density and to act as intrinsic burnable absorbers. Ditungsten pentaboride is envisioned as a potential shielding material for compact fusion reactors of the spherical tokamak-type.

New synthetic routes to uranium and tungsten borides have been tested and optimised with the support of thermodynamic modelling. All known borides of uranium (UB_2, UB_4, UB_{12}) have been prepared from the borocarbothermic reduction of uranium dioxide (UO_2) with boron carbide (B_4C), carbon (C), and diboron trioxide (B_2O_3). The synthesis route has been shown to be capable of reliably producing UB_2 with purities between 90% and 95% (on a heavy metal basis). An analogous process has been used to produce three different borides of tungsten (W_2B, WB, W_2B_5) from

tungsten trioxide (WO_3), obtaining products with purities greater than 99% (on a heavy metal basis) in the case of WB and W_2B_5.

Several thermodynamic models have been used to predict and describe the chemical interactions of UB_2. In particular, contact interactions of UB_2 with materials relevant to the nuclear industry have been assessed and experimental data on the oxidation of UB_2 have been successfully interpreted.

A preliminary assessment of the burnup chemistry of UB_2 was performed using data from neutronic simulations, describing the possible behaviours of major irradiation products and suggesting that excessive fragmentation of boron may challenge the stability of the UB_2 matrix.

Solid solutions of UB_2 and ZrB_2 have been prepared as surrogate materials for UB_2 doped with Zr produced by fission events, measuring the lattice distortion associated with the inclusion of Zr in the crystal lattice.

Finally, a possible path to the preparation and testing of the ATF composite fuel concept is presented, outlining the extant research needs.

2. Introduction

2.1. Advanced Technology Fuels for fission reactors

The goal of Advanced Technology Fuels (ATFs) fuel for fission reactors is to provide enhanced performance in power generation, accident tolerance, or both, when compared to conventional UO_2 fuel, although trade-offs which decrease the current safety margin of UO_2 to increase the performance during normal operation are deemed unacceptable, according to the "do no harm" principle [1]. A widely used metric to define accident tolerance is the coping time, defined as the time that can elapse between a severe accident and outside intervention before the reactor pressure vessel is rendered permanently inoperable by catastrophic failure of the fuel assemblies [2].

As for the improved performance in power generation, minimizing the refuelling downtime of a nuclear reactor is crucial in improving its availability, capacity factor and economics. Most of the current and prospective designs of commercial nuclear power reactors operate on a batch principle, thereby requiring to be periodically shut down to replace the spent fuel assemblies with fresh ones [3]. The CANDU [4], AGR [5], and RBMK [6] designs are notable exceptions in that they allow online refuelling.

The time that can elapse between two refuelling outages is directly linked to the amount of energy that can be safely extracted from a batch of nuclear fuel, which depends in turn on the quantity of fissile atoms contained in the batch itself and on the extent of burn-up that the fuel material and its cladding can withstand before their properties are excessively degraded [7]. Degradation of the fuel may lead to its premature failure and to unplanned outages, which are even more detrimental to the economics of the reactor due to their sudden nature and to the need to procure backup generation on the electrical grid to replace the output of the reactor.

The approach to improving economics must therefore focus on increasing the absolute amount of energy that is available in the fuel and on increasing the durability of the latter with respect to its operating conditions. These effects may be attained, respectively, by acting on the neutronic properties of the fuel, with a greater inventory of fissile material in the fuel assemblies, or by acting on its materials properties, with a fuel-cladding ensemble which is able to withstand more severe damage or which, alternatively, operates in milder conditions.

The two possible approaches in the improvement of the performance of the current nuclear fuels are outlined below, although their separation is far from sharp owing to the intricate interplay of phenomena that characterise the operation of nuclear reactors.

2.1.1. ATFs: the neutronics approach

The possible methods that can be used to increase the amount of fissile material in a given core volume are:

- increasing the enrichment of fissile isotopes in the fresh material;
- increasing the volume fraction that is dedicated to fuel;
- using fuel materials with high densities of fissile atoms;
- increasing the breeding ratio.

The increasing trend in construction costs of nuclear power stations after the Three Mile Island accident in 1979 [8], due to increased plant complexity and regulatory delays, put growing economic pressure on maximising their operability, thus making higher-enrichment fuel economically viable, despite the higher cost. After 2009, moreover, several factors contributed to significantly decrease the cost per SWU (Separative Work Unit) to produce enriched uranium [9], further encouraging the development of fuel and reactor concepts relying on higher enrichments for greater operability: the reduction in general demand due to the 2009 Great Recession; the reduction in nuclear fuel demand due to the Fukushima accident in 2011; the retirement of enrichment plants based on the gaseous diffusion technology in favour of the far less expensive centrifuge technology. The consolidation of Russia as a major supplier of enriched uranium, holding 46% of the global enrichment capacity as of 2022 [10], also played a notable role in driving down the prices, both owing to its state-owned and heavily subsidised enrichment industry and to the downblending of highly enriched weapons-grade uranium through the Megatons to Megawatts program [11]. However, the strong international tensions resulting from the invasion of Ukraine by Russia in 2022 in the context of the Russo-Ukrainian conflict and the Russian strategy of using the energy dependence of other countries to its advantage [10] have resulted in concerns for the security of supply of enriched uranium, with uncertainty fostering speculation and volatility in the uranium enrichment market [12].

From a neutronics perspective, a higher enrichment will result in a greater reactivity of the fuel at the Beginning Of Life (BOL). Integral Burnable Absorbers (IBA) have thus been developed to flatten the reactivity profile of higher-enriched fuel throughout the fuel cycle, which at this point can be longer than the one of its lower-enriched counterpart [13].

Furthermore, high-performing IBAs in PWR fuel may allow for a reduction in the concentration of boron in the primary coolant water and the related issues regarding positive void coefficient [14], neutronic anomalies from the precipitation of borates (such as axial offset anomalies) [15], plant complexity, operating costs, and corrosion of reactor components [16].

IBAs have been introduced in the fuel material as coatings [17], solid solutions [17], or inclusions of secondary phases [18,19]. The neutronic performance of IBAs improves with the extent of their dispersion in the fuel material, until a homogeneous dispersion – in the ideal limit of a solid solution – is reached [20]. In fact, the localization of coating-based IBAs in the high-flux region of the pellet's rim limits the duration and the magnitude of their reactivity-flattening effect [21].

Gadolinium oxide (Gd_2O_3) is widely used as an IBA in solid solution with UO_2 both in PWRs and BWRs [22]. However, mixing of UO_2 and Gd_2O_3 is not without consequences and usually results in a material with a lower thermal conductivity [23] and a lower melting point [24] when compared to pure UO_2 whereas, as shown in Section 2.1.2, a high thermal conductivity is desirable in a nuclear fuel [25]. Moreover, non-fissionable IBAs displace heavy metal atoms and therefore require a higher enrichment to achieve set values of burn-up and power density in a given core design [17].

Coatings are advantageous in that, for a given reactivity modulation, they displace the least amount of fissile material but, being applied to the surface, return a less homogeneous neutron flux profile across the pellet when compared to the other two technologies. A prominent coating technology is the Integral Fuel Burnable Absorber (IFBA) developed by Westinghouse [26], consisting of a zirconium diboride (ZrB_2) coating applied to UO_2 pellets.

Ideally, dispersions of particles would retain at least part of the neutronic homogeneity advantage of the solid solutions, while at the same time avoiding to negatively affect the thermal properties of the UO_2 matrix that surrounds them, although. In fact, depending on the thermal conductivity of the

dispersed phase and on the quality of the thermal contact at the interface, the thermal conductivity of the resulting composite could be increased. This phenomenon justifies the rationale for UO_2 additives such as diamond ($C_{(diamond)}$) [27] and beryllium oxide (BeO) [28], which are chiefly intended as thermal conductivity improvers.

While decreasing in cost as an option, however, increasing the enrichment of nuclear fuel, may require a reassessment of the criticality limits of the existing fuel enrichment and manufacturing plants, as well as fuel handling procedures [29], potentially leading to decreased throughput. Thus, a strategy not involving an increase of the enrichment level would entail modifying the density of fissionable atoms in the volume of the core that is dedicated to the fuel. The density of heavy metal atoms depends on the substances that constitute the fuel material and on its smeared density – that is, the ratio between the mass of fuel that is actually enclosed in the cladding and the mass that could be contained in the same volume without any voids, gaps and pores. It must be noted that, in order to mitigate the adverse effects of fuel swelling under irradiation (which negatively affect fuel durability) [30] and to improve the retention of fission products, [31], less-than-full densification may be desirable in fresh fuel. It is therefore worthwhile to investigate materials with an intrinsically high uranium density.

Moreover, despite the higher concentration of fissile atoms, high-density fuels have a lower beginning-of-life reactivity and do not require as much burnable absorbers as higher-enriched, lower-density fuels thanks to the "fertile poison" effect of ^{238}U, which is in turn present in greater amount as well [32]. The enhanced breeding in the early phase of the burn-up will help in providing increased reactivity in the later stages of the power-generating cycle, thus flattening the reactivity profile. It is also worth noting that the breeding ratio increases with the heavy-metal-to moderator ratio and, for a given core geometry, a higher-density fuel will increase the utilization of the fertile isotopes [33].

2.1.2. ATFs: the materials approach

The possible methods that can be used to enhance the relative durability of the fuel are:

- reducing the severity of the operating conditions;

- changing the material and the thickness of the cladding to increase its thermal, mechanical, and chemical resistance.

The reduction in the severity of the operating conditions is closely linked to an increase in the thermal conductivity of the fuel: a higher thermal conductivity would allow for a shallower temperature gradient for a given value of the heat flux and of the cladding outer temperature (and thus reactor power). The shallower temperature gradient granted by a higher thermal conductivity would allow the fuel to operate at a lower average temperature, leading to a number of desirable effects [34]:

- reduced rate of the temperature-dependent release of fission products;
- reduced rate of chemical corrosion reactions on cladding;
- reduced pellet strain resulting from thermal expansion;
- reduced amount of thermal energy stored inside the fuel;
- increased margin to centre-line melting.

The release of fission gases in the plenum of the fuel rod is highly detrimental to fuel durability, due to pressurisation of the cladding (leading to ballooning, which may cause the obstruction of a coolant channel, or bursting in accident conditions [35]) and to corrosion by chemically reactive fission products, such as iodine [36]. Moreover, the rate of the chemical and physical processes associated with corrosion increases with temperature.

Thermal expansion is also crucial in determining the severity of the Pellet-Cladding Mechanical Interactions (PCMIs) [36], as the expansion of the fuel pellets across the cladding gap and against the inner wall of the cladding determines the pressure that is applied to the cladding. Moreover, differential thermal expansion of the pellets due to the thermal gradient (with the centre expanding more than the rim) will cause cracking, which will decrease the thermal conductivity and further increase the temperature gradient.

The thermal energy stored in the fuel is one of the components of the total energy stored in the core (which also comprises the mechanical energy due to pressurisation and the chemical energy associated with possible chemical reactions among the contents of the core) and should be minimised according to intrinsic safety principles [37].

The margin from the centre-melting of the fuel material is a crucial part of the Defence-In-Depth design strategy [38]: the solid form of the fuel is the innermost barrier of containment for radioactive materials and its efficacy would be drastically diminished by its melting. Furthermore, in its molten state, fuel is generally more mechanically and chemically aggressive towards the cladding that encases it, thereby endangering the second-innermost barrier of containment [39].

It is also worth noting that part of the greater reactivity margin that some fuels may offer (as seen in Section 2.1.1, mostly at BOL for conventional fuels with higher enrichment and throughout the life cycle with high-density fuels) may be expended by accepting a greater neutron penalty from the cladding – either from increasing its thickness or by using materials not as neutron-transparent as zirconium alloys – in exchange for improved thermal, mechanical and chemical resistance [1].

With fewer neutronic constraints, the cladding could be designed to be more resistant in both normal and accident conditions, with a longer useful life, a reduced risk of fuel failures (and thus of unplanned outages), and increased accident tolerance. However, the parasitic neutron absorption may still be detrimental towards the end of the fuel cycle, especially for the fuels relying on increased enrichment rather than high density.

2.1.3. Fuel materials combining high heavy metal density and high thermal conductivity

The currently most used fuel materials for commercial nuclear reactors in the world are based on uranium dioxide (UO_2), featuring exceptional thermal and chemical stability, and the capability to accommodate additives and fission products into its crystal lattice. UO_2-based fuels owe part of their success also to the relative ease with which they may be handled and fabricated. On the other hand, the thermal stability of UO_2 is really invaluable in conjunction with its poor thermal conductivity, which results in steep radial temperature gradients across the fuel pellets and in high centre-line temperatures.

As Section 2.1.1 and 2.1.2 outlined the beneficial effect of high heavy metal density and high thermal conductivity for nuclear fuels, Table 2.1 illustrates a set of uranium-bearing substances which outperform UO_2 under both aspects and which may be candidate materials for the fabrication of ATFs.

Table 2.1: Uranium density and thermal conductivity of several substances compared to UO_2.

Substance	**Uranium density at 298 K (nat. U)**	**Thermal conductivity**			
		298 K	**1000 K**	**1500 K**	**Source**
UO_2	9.66 g/cm$_3$ [40]	8 W/m·K	3 W/m·K	2 W/m·K	[41]
UB_2	11.69 g/cm$_3$ [42]	33 W/m·K	24 W/m·K	27 W/m·K	[43]
UC	12.95 g/cm$_3$ [44]	21 W/m·K	21 W/m·K	22 W/m·K	[45]
UN	13.53 g/cm$_3$ [46]	12 W/m·K	17 W/m·K	20 W/m·K	[45]
U_3Si_2	11.31 g/cm$_3$ [47]	10 W/m·K	22 W/m·K	28 W/m·K	[48]
U	19.10 g/cm$_3$ [40]	24 W/m·K	40 W/m·K	N.A. (melts)	[49]

It must be noted that these values of thermal conductivity refer to the pure, unirradiated substances. The overall thermal conductivity of most materials results from the sum of three components: one associated with heat transfer due to lattice vibrations, one associated with heat transfer due to electronic conduction, and one associated with heat transfer through thermal radiation [50]. The thermal radiation contribution usually only becomes relevant at very high temperatures (for example, the thermal conductivity of UO_2 can be accurately described up to 3120 K by models that consider only the vibrational and electronic contributions [51]), while both the vibrational and electronic contributions can be negatively affected by crystal lattice defects caused by irradiation and by the inclusion of fission and transmutation products in the crystal lattice, both of which are closely associated with fuel burn-up [52]. The advantage in thermal conductivity of the non-oxide fuel material candidates of Table 2.1 over UO_2 must therefore be weighed against the consistency with which such an advantage can be maintained in reactor conditions, requiring extensive irradiation campaigns and post-irradiation examination for an in-depth understanding.

Moreover, in the case of ceramic materials, the vibrational contribution to thermal conductivity usually decreases with temperature owing to phonon scattering, while the electronic contribution increases with it (unlike the case for pure metals, where this terms remains roughly constant), owing to the increased mobility of charge carriers [53,54]. For the uranium ceramics reported in Table 2.1 the combination of these effects results in a convex curve of the thermal conductivity against temperature, with higher values at the temperature extremes and a minimum at intermediate values.

For UB_2 this minimum of thermal conductivity is located at 874 K [43], while for UO_2 it is located at approximately 1900 K [41].

Furthermore, substances with a more closely spaced lattice (inevitably linked to a higher uranium density) usually exhibit higher diffusivities for defects and smaller lattice cavities to host the atoms resulting from fission or decay. This is especially relevant for gaseous species such as He, Kr and Xe, which are poorly accommodated inside metallic fuels and can diffuse to form bubbles or escape the fuel matrix [55]. However, since diffusivity (and thus the rate of release of fission gases) increases with temperature, a fuel with higher uranium density and higher thermal conductivity than UO_2 may actually offer improved performance in the retention of fission gases, as verified experimentally in the case of UN compared to UO_2 [1].

The main obstacle to the usage of non-oxide fuels is their sensitivity to oxidation, which is expected to be significantly greater than that of UO_2 and is reflected both in the exothermicity and in the favourability of their oxidation reactions, as shown in Table 2.2 (the values were calculated as described in Section 3.1)

Table 2.2: Reactions with oxygen, their variations in enthalpy (referred to O_2), and their equilibrium constants for selected uranium substances

Substance	**Reaction**	**$\Delta_R H^{\ominus}$ at 1000 K**	**K_{eq} at 1000 K**
UO_2	$3\ UO_{2\,(s)} + O_{2\,g)} \rightarrow U_3O_{8\,(s)}$	-110.7 kJ/mol O_2	$2.3 \cdot 10^{14}$
UB_2	$UB_{2\,(s)} + 3\ O_{2\,g)} \rightarrow UB_2O_{6\,(s)}$	-774.6 kJ/mol O_2	$2.3 \cdot 10^{99}$
UC	$6\ UC_{\,(s)} + 11\ O_{2\,(g)} \rightarrow 2\ U_3O_{8\,(s)} + 6\ CO_{\,(g)}$	-618.3 kJ/mol O_2	$2.6 \cdot 10^{345}$
UN	$6\ UN_{\,(s)} + 8\ O_2 \rightarrow 2\ U_3O_{8\,(s)} + 3\ N_{2\,(g)}$	-620.2 kJ/mol O_2	$3.6 \cdot 10^{247}$
U_3Si_2	$U_3Si_{2\,(s)} + 6\ O_{2\,(g)} \rightarrow U_3O_{8\,(s)} + 2\ SiO_{2\,(s)}$	-831.7 kJ/mol O_2	$7.6 \cdot 10^{223}$
U	$3\ U_{\,(s)} + 4\ O_{2\,(g)} \rightarrow U_3O_{8\,(g)}$	-823.7 kJ/mol O_2	$7.6 \cdot 10^{164}$

There are two possible routes towards the mitigation of this flaw, with the first one being employing these fuel materials in reactors which do not use oxidising coolants, thus ruling out their application in LWRs; liquid metals and helium may be suitable coolants in this respect and, with many reactor designs using them having fast neutron spectra and higher operating temperatures than LWRs, the

high heavy metal densities and the high thermal conductivity of the candidate fuels would be exploited in full.

However, the development of ATF candidates cannot be separated from considerations on the practicality of their preparation, handling, and disposal and any performance advantages that they may grant must always be weighed against the scalability of their production process and the costs of their development and production [56]. Compatibility with existing or planned reactor designs is also a key requirement to achieve a high Technology Readiness Level [57].

Thus, to attain compatibility with existing LWRs, it could be conceivable to disperse particles of non-oxide uranium ceramics inside a chemically inert matrix that would protect them from the surrounding oxidising environment. This matrix could be constituted by a refractory ceramic (CERamic-CERamic composite, CERCER) [58,59] or by a refractory metal (CERamic-METal composite, CERMET) [60,61].

It is worth noting that the matrices of CERCER and CERMET fuels are often chosen from a range of materials with a relatively high thermal conductivity (e.g. MgO or SiC for CERCERs – 11 W/m·K [62] and 61 W/m·K [63] at 1000 K, respectively [62] – and W or Mo for CERMET – 120 W/m·K [64] and 110 W/m·K [65] at 1000 K, respectively), thus acting as effective heat sinks for the heat-generating particles that they encase. The inert surrounding matrix would also provide an additional barrier layer to the release of radionuclides, an advantage which may be relevant in the preparation of targets for the irradiation and transmutation of highly radiotoxic transuranic isotopes and which may provide a suitable highly stable waste-form for direct geological disposal after irradiation [66]. However, the dilution of the high-density fuel in the inert matrix would defeat the purpose of the high-density ceramic itself by lowering the smeared density of heavy metal in the fuel material. In fact, the main application of the current proposed CERMET or CERCER composites is in fast reactors, where the matrix is used to overcome the limitations in the chemical and physical properties of otherwise neutronically attractive targets [67] and CERCER fuels are often found to compete poorly with the current, highly optimised UO_2-based fuels [68].

However, if UO_2 is chosen as the matrix material, a performance advantage could be gained by a CERCER composite with respect to bulk UO_2. Ideally, the UO_2 matrix would retain its exceptional thermal, mechanical and chemical stability while protecting the particles from the oxidising coolant,

while the particles would increase the overall thermal conductivity and uranium density of the composite. ATF concepts of this kind, with UN [69] and U_3Si_2 [70] dispersed in a UO_2 matrix, have been manufactured for testing. Experiments in flowing synthetic air demonstrated the effectiveness of the UO_2 matrix in protecting uncoated UN particles up to loading fractions of 10% [71].

Using a linear combination approach for the uranium density and the model of elaborated by Maxwell for the thermal conductivity of composites [72], it is possible to gain an approximate understanding of the performance advantage associate with the dispersion of non-oxide uranium ceramics inside a UO_2 matrix.

Maxwell's model for thermal conductivity refers to identical spherical particles of thermal conductivity k_p uniformly dispersed with a volume fraction φ_p in a matrix with thermal conductivity k_m, with the overall thermal conductivity of the composite k_c being described by equation 2.1:

$$k_c = k_m \cdot \left(1 + \frac{3\varphi_p}{\left(\frac{k_p + 2k_m}{k_p - k_m}\right) - \varphi_p} \right) \qquad 2.1$$

Maxwell's model assumes infinite dilution of the dispersed phase (i.e. no thermal interaction between neighbouring particles) and ideal thermal contact at the interface between the guest particles and the host matrix [73]. However, it was found to describe well the behaviour of composites up to values of φ_p up to 25% [72]; furthermore, the limit of infinite dilution makes the model insensitive to the size of the particles, thus making it highly versatile in a preliminary analysis.

It is also worth noting that Maxwell's model can also successfully describe the effect of porosity on a solid matrix by considering the pores as a dispersed phase with negligible thermal conductivity; it is possible to rearrange equation 2.1 by imposing $k_p = 0$ and introducing a shape factor σ to account for non-spherical pores, thus obtaining the Maxwell-Eucken equation [74]:

$$k_c = k_m \cdot \left(\frac{1 - \varphi_p}{1 + (\sigma - 1)\varphi_p} \right) \qquad 2.2$$

Where φ_p is the volume fraction of pores and $\sigma = \frac{3}{2}$ corresponds to the case of spherical pores.

Figure 2.1 shows the theoretical improvements in thermal conductivity at 1000 K (indicative of the smeared fuel temperature in current LWRs [75]) and in uranium density of a composite based on a UO_2 matrix as a function of the volume fraction of the dispersed phase for UB_2, UN, and U_3Si_2, which are assumed to be introduced as kernels, as calculated from equation 2.1 and the values reported in Table 2.1. It is worth noting that other particle shapes may optimise heat transfer and thus increase the overall thermal conductivity of the composite, especially if they are aligned along the expected direction of heat transfer [76,77].

For a loading fraction of 10%, kernels of UB_2, UN, and U_3Si_2 could be expected to increase the thermal conductivity up to 22.6%, 19.4%, and 21.8%, respectively, while the uranium density (assuming the same level of densification between the UO_2 matrix and the guest ceramics) will increase by 2.1%, 4.0%, and 1.7%. Given the highly non-linear nature of nuclear reactors, these seemingly trivial enhancements may actually lead to significant improvements in fuel performance.

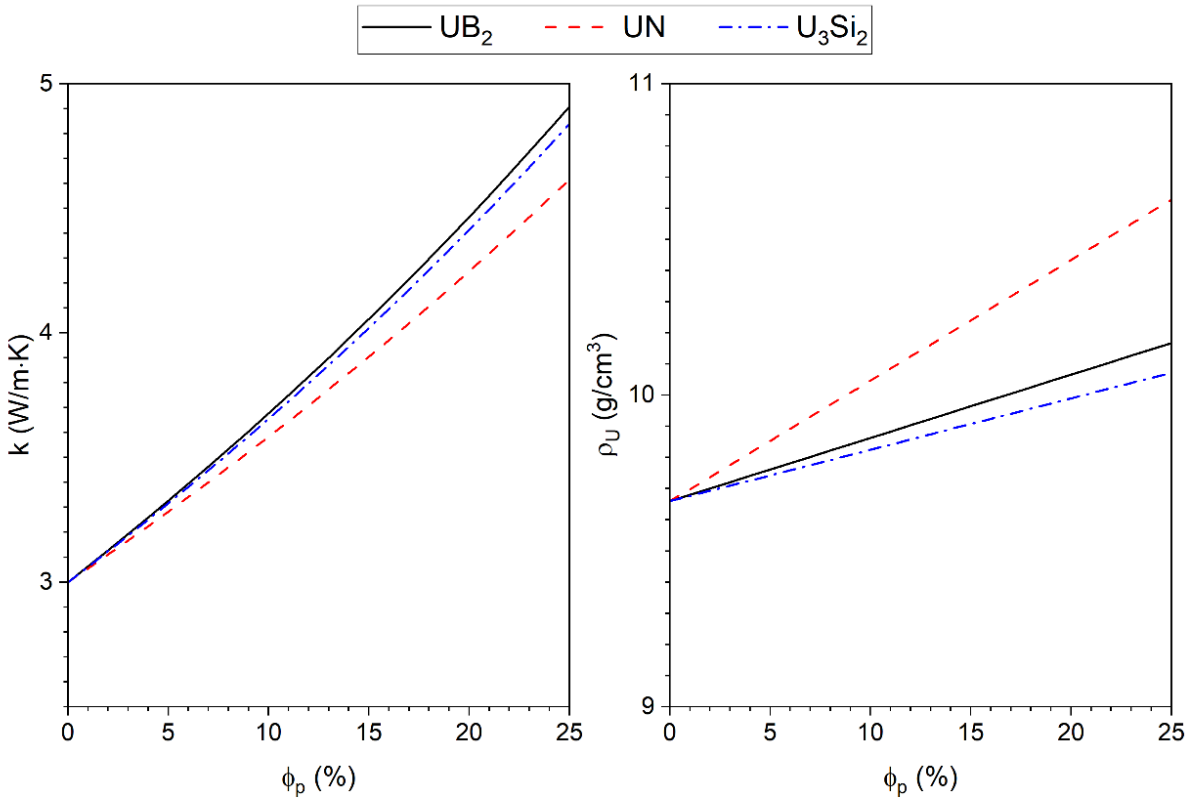

Figure 2.1: Calculated improvements in thermal conductivity at 1000 K (left) and uranium density (right) of UO_2 as a function of the volume fraction of dispersed kernels of UB_2, UN, and U_3Si_2.

2.2. Uranium borides as materials for nuclear fuels for fission reactors

Among the three materials shown in Figure 2.1, UB_2 showed the highest improvement in thermal conductivity and the second-highest improvement in uranium density. Moreover, its content of boron makes UB_2 uniquely suited to act as both a high-performance additive and an IBA [43]. In fact, two main isotopes of boron exist in nature, with the properties outlined in Table 2.3.

Table 2.3: Abundances and properties of the two naturally-occurring isotopes of boron.

Isotope	Abundance	Thermal neutron capture cross section (0.025 eV)
^{10}B	~ 20%* [78]	3870 barn [79] via [80]
^{11}B	~ 80%* [78]	0.0055 barn [79] via [80]

** The isotopic abundance of naturally occurring boron can vary even by a few percent points depending on its geological history*

Having two main natural isotopes in comparable abundances, with notably different neutron absorption properties and established isotopic separation procedures [81], the isotopic composition of the boron in UB_2 may be tailored to tune its properties between those of a high-performance fuel and a high-performance burnable absorber [18].

Three congruently melting uranium-boron compounds are known: uranium diboride (UB_2), uranium tetraboride (UB_4), and uranium dodecaboride (UB_{12}). The phase diagram of the B-U system is presented in Figure 2.2, as reported by Okamoto [82], while the crystal lattice properties of UB_2, UB_4, and UB_{12} are reported in Table 2.4 . The three structural types of UB_2, UB_4, and UB_{12} have been reported to allow for deviations in their stoichiometry, often in the form of a defective boron sublattice. Martel *et al.* reviewed the available literature on uranium borides and prepared samples of the three borides by arc melting of elemental uranium and boron, with the three samples having stoichiometries of $UB_{1.78}$, $UB_{3.61}$, and $UB_{11.19}$, respectively, as measured by mass spectrometry [83]. The tendency to mainly exhibit hypostoichiometry of boron is supported by the computational work of Burr *et al*. [21], which shows a significantly higher energy of formation for uranium vacancy defects (and thus a far less thermodynamically favourable process for their formation) as opposed to boron vacancy defects; in fact, based on the reaction energies reported, it is likely that any excess boron in a UB_{2+x} structure would rather be accommodated by formation of boron-rich sub-phases, such as UB_4 .

Table 2.4: Crystallographic properties of UB_2, UB_4, and UB_{12}.

Substance	**Space group**	***a***	***b***	***c***	**α**	**β**	**γ**	**Formulas per cell**	**Ref.**
UB_2	$P6/mmm$	3.1302 Å	3.1302 Å	3.9878 Å	90°	90°	120°	1	[42]
UB_4	$P4/mbm$	7.0753 Å	7.0753 Å	3.9008 Å	90°	90°	90°	4	[42]
UB_{12}	$Fm\bar{3}m$	7.4750 Å	7.4750 Å	7.4750 Å	90°	90°	90°	4	[42]

The properties of the three uranium borides are summarised in Table 2.5 together with those of ZrB_2, a prominent boron-based IBA, as seen in Section 2.1.1. Uranium tetraboride (UB_4) has already been used as a burnable absorber in the form of particles dispersed in a UO_2 matrix. Fuel pellets containing UB_4-based IBA particles were produced as part of the NERO program, involving research on nuclear marine propulsion for the Otto Hahn merchant ship, with UB_4 being chosen over the other borides owing to its high boron content and high melting point [84].
The fuel pellets containing the UB_4 dispersion were noted to have experienced a lower average temperature, demonstrating the concept of improving the thermal conductivity of UO_2 with borides [84].

When compared to ZrB_2 in their capacity as IBAs, the borides of uranium have the advantage of displacing minimal fuel in the case of UB_4, or even having a net increase in fuel inventory, in the case of UB_2, as shown in Table 2.5 .

It must be noted that the thermal conductivity of boride-based IBAs may also be negatively affected by burnup with the production of intrinsic, compositional and microstructural defects, deriving respectively from radiation damage, the transmutation of U and ^{10}B (the latter fragmenting into ^{7}Li and ^{4}He [85]), and the formation of cracks and gas bubbles [86]. The release of helium would also lead to an increase in the internal pressure of the fuel rods, thus increasing the likelihood of cladding ballooning and failure [35].

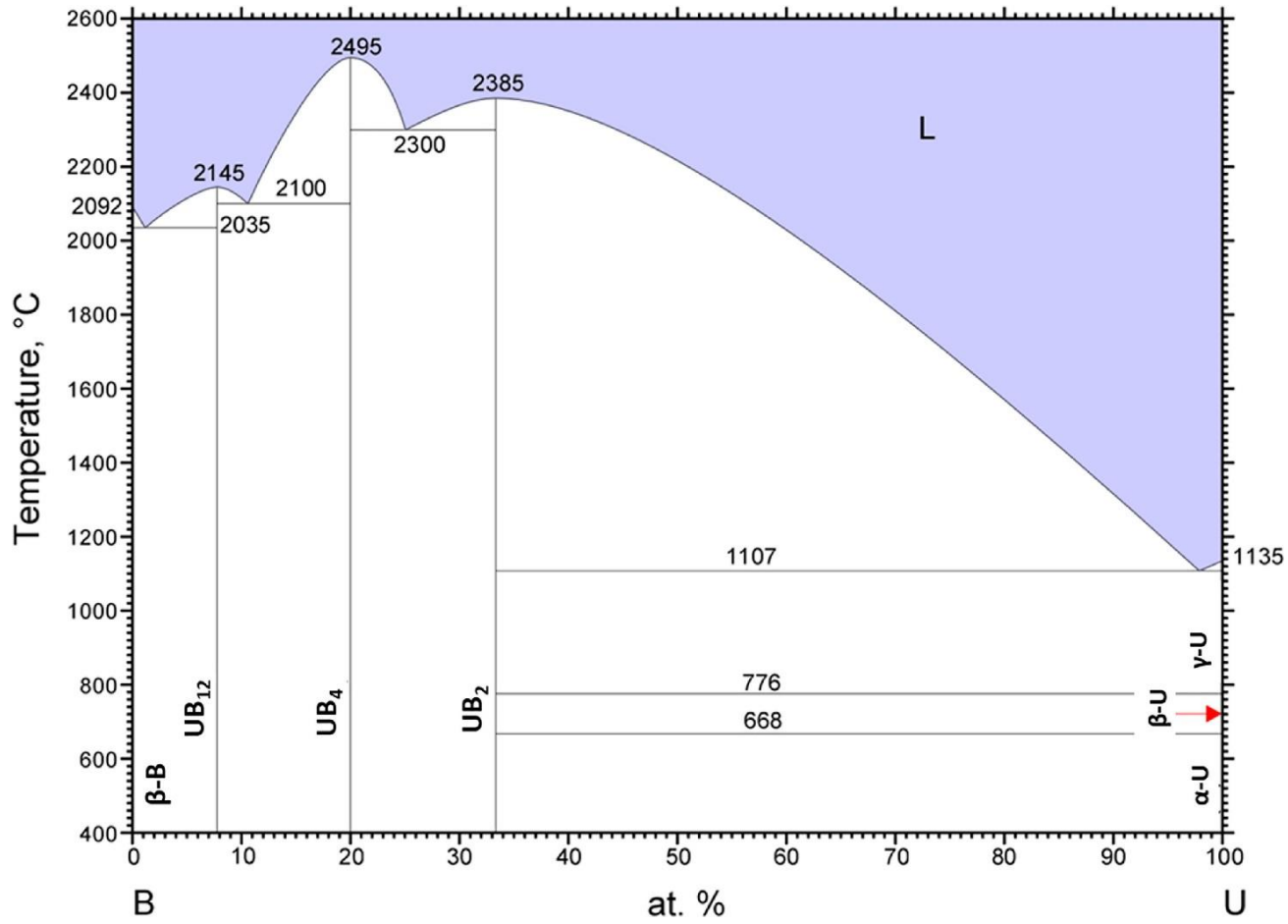

Figure 2.2: Phase diagram of the B-U system

Table 2.5: Relevant properties of unirradiated UO_2, UB_2, UB_4, UB_{12}, and ZrB_2.

Substance	**Uranium density at 298 K (nat. U)**	**Boron density at 298 K (nat. B)**	**Melting point**	**Thermal conductivity (298-1000 K)**
UO_2	9.66 g/cm^3 [40]	-	3120 K [41]	8-3 W/m·K [41]
UB_2	11.69 g/cm^3 [42]	1.06 g/cm^3 [42]	2703 K [87]	33-24 W/m·K [43]
UB_4	8.00 g/cm^3 [42]	1.45 g/cm^3 [42]	2768 K [87]	15-22 W/m·K [43]
UB_{12}	3.79 g/cm^3 [42]	2.06 g/cm^3 [42]	2418 K [87]	13 W/m·K at 298 K [88]
ZrB_2	-	1.17 g/cm^3 [89]	3245 K [90]	127-77 W/m·K [91]

Moreover, since ^{11}B is an excellent neutron moderator [92], having a lower atomic mass than ^{12}C, $U^{11}B_2$ may be potentially unsuitable as a fuel for fast reactors due to excessive softening of the neutron spectrum.

2.3. Synthesis of uranium borides

All uranium borides can be prepared via reactive melting of elemental uranium and boron through reaction 2.3 [42]:

$$U_{(l)} + n\ B_{(s)} \rightarrow UB_{n\,(s)} \qquad 2.3$$

With n = 2, 4, or 12. The process above is indicated for research applications and has the advantage of introducing minimal impurities of elements other than U and B in the final products. However, the industrial scale-up of the process would be quite challenging due to it being energy-intensive and presenting safety concerns regarding the handling of pyrophoric metallic uranium powders [93]. Moreover, while it is possible to achieve good homogeneity of the final product after one single melting cycle [43], with the process being diffusion limited, it is likely that multiple crushing-and-remelting cycles of the products may be required for larger batch sizes [42].
Uranium boride has been obtained by Lupinetti *et al.* [94] through the metathesis of uranium tetrachloride (UCl_4) and magnesium diboride (MgB_2), carried out at a temperature of 850 °C, as described in reaction 2.7:

$$UCl_{4\,(s)} + 2\ MgB_{2\,(s)} \rightarrow UB_{4\,(s)} + 2\ MgCl_{2\,(s)} \qquad 2.4$$

With the resulting magnesium chloride ($MgCl_2$) being removed by washing with water. However, a reaction with a lower-than-stoichiometric ratio of MgB_2 only resulted in an incomplete process with no formation of UB_2, indicating that this process may not be suitable for its production.

Schlesinger *et al.* reported that UB_4 could be one of the decomposition products of uranium borohydride ($U(BH_4)_4$) [95], although no conclusive crystallographic identification was performed. Uranium borohydride is prepared from the reduction of uranium tetrafluoride (UF_4) with aluminium borohydride in reaction 2.7:

$$UF_{4\,(s)} + 2\ Al(BH_4)_{3\,(l)} \rightarrow U(BH_4)_{4\,(s)} + 2\ Al(BH_4)F_{2\,(l)} \quad 2.5$$

With uranium borohydride decomposing exothermically if heated according to reaction 2.6:

$$U(BH_4)_{4\,(s)} \rightarrow UB_{4\,(s)} + 8\ H_{2\,(g)} \quad 2.6$$

It is worth noting that this was likely not investigated as a way to produce UB_4, but, rather, an unintended reaction of uranium borohydride, which, being one of the few volatile uranium substances known in the early 1940s, was envisioned as a possible material to be used in the gaseous enrichment of ^{235}U before the UF_6 process was established [96].

On an industrial scale, metal borides are usually obtained through the reduction at high temperature (> 1000 K) of the corresponding metal oxide with suitable boron compounds and other reductants. Examples include elemental boron (B), boron carbide (B_4C), diboron trioxide (B_2O_3), carbon (C), magnesium (Mg) and their combinations, defining classes of reactions named borothermic (reaction 2.7), borocarbothermic (reactions 2.8 and 2.9), and metallothermic [97–99]. For simplicity, the reactions below refer to the dioxides MO_2 as starting material:

$$MO_{2\,(s)} + (n + 2)\ B_{\,(s)} \rightarrow MB_{n\,(s)} + B_2O_{2\,(g)} \quad 2.7$$

$$MO_{2\,(s)} + \frac{n + x}{4}\ B_4C_{\,(s)} \rightarrow MB_{n\,(s)} + y\ B_2O_{2\,(g)} + z\ B_2O_{3\,(l,g)} + \frac{n + x}{4}\ CO_{\,(g)} \quad 2.8$$

$$MO_{2\,(s)} + \frac{n}{2}\ B_2O_{3\,(l)} + (2 + \frac{3}{2}n)\ C \rightarrow MB_{n\,(s)} + (2 + \frac{3}{2}n)\ CO_{\,(g)} \quad 2.9$$

$$MO_{2\,(s)} + \frac{n}{2}\ B_2O_{3\,(l)} + (2 + \frac{3}{2}n)\ X_{\,(s)} \rightarrow MB_{n\,(s)} + (2 + \frac{3}{2}n)\ XO_{\,(s)} \quad 2.10$$

Where X in reaction 2.10 represents a reducing metal (usually Mg).

Larroque *et al.* prepared UB_4 from reaction 2.8:

$$7\ UO_{2\ (s)} + 8\ B_4C_{\ (s)} \rightarrow 7\ UB_{4\ (s)} + 2\ B_2O_{3\ (l,g)} + 8\ CO_{\ (g)} \qquad 2.11$$

UB_{12} has been prepared by Paderno *et al.* from the borothermic reduction of UO_2 at 1500 °C, performed under vacuum [100]. No details on the status of the volatile products were provided, but it is likely that B_2O_2 was the main species among them, in reaction 2.12

$$UO_{2\ (s)} + 14\ B_{\ (s)} \rightarrow UB_{12\ (s)} + B_2O_{2\ (g)} \qquad 2.12$$

It is apparent how reduced boron species (B, B_4C) act as both sources of boron and as reductants in reactions 2.7 and 2.8. For practical applications, however, the role of reductants should be transferred as much as possible to less expensive materials, such as carbon. Compared to the metallothermic reduction, the reduction with carbon has the advantage of not having to remove the metal oxide that forms, as the by-product of the reaction is gaseous CO.
The potential of the borocarbothermic reaction is well-exploited in the preparation of UB_4 as reported by Guo *et al.* [101], through the modification of reaction 2.8 with the addition of carbon:

$$UO_{2\ (s)} + B_4C_{\ (s)} + C_{\ (s)} \rightarrow UB_{4\ (s)} + 2\ CO_{\ (g)} \qquad 2.13$$

Noting that B_4C can be produced by the reaction between B_2O_3 and C (a process that represents its main industrial production route [102]) in reaction 2.14:

$$2\ B_2O_{3\ (l)} + 7\ C_{\ (s)} \rightarrow B_4C_{\ (s)} + 6\ CO_{\ (g)} \qquad 2.14$$

Reaction 2.13 could then be seen also as a modification of reaction 2.9, where appropriate amounts of B_2O_3 and C have been replaced by B_4C.

UB_2 was prepared by Turner *et al.* [34] with the contribution of the Author via the borocarbothermic reduction of UO_2 to UB_2 in reaction 2.15, mirroring one of the methods by which ZrB_2 is prepared industrially [99]:

$$2\ UO_{2\ (s)} + B_4C_{\ (s)} + 3\ C_{\ (s)} \rightarrow UB_{2\ (s)} + 4\ CO_{\ (g)} \qquad 2.15$$

The understanding and the optimisation of this reaction are one of the main subjects of this thesis.

2.4. Scope of the thesis: building towards a concept for a UB_2-UO_2 composite fuel pellet

One Advanced Technology Fuel (ATF) concept that is envisioned as a potential application of UB_2 consists of a pellet composed of a UO_2 matrix in which particles of UB_2 are dispersed, as illustrated in Figure 2.3. The shape and the size of the pellet would be compatible with current reactor designs (i.e., a cylinder with its diameter and height in the 8-12 mm range) and the particles would have dimensions in the 0.5-1.5 mm range.

The particles of UB_2 may be coated with refractory metals or ceramics [18] in order to reduce their chemical reactivity towards the matrix and the inner wall of the cladding during normal operation and towards the coolant during severe accident conditions. While adding complexity to the manufacturing process and a neutronic penalty during reactor operation, the coating would nonetheless also provide an additional barrier for the containment of part of the fuel's radioisotope inventory.

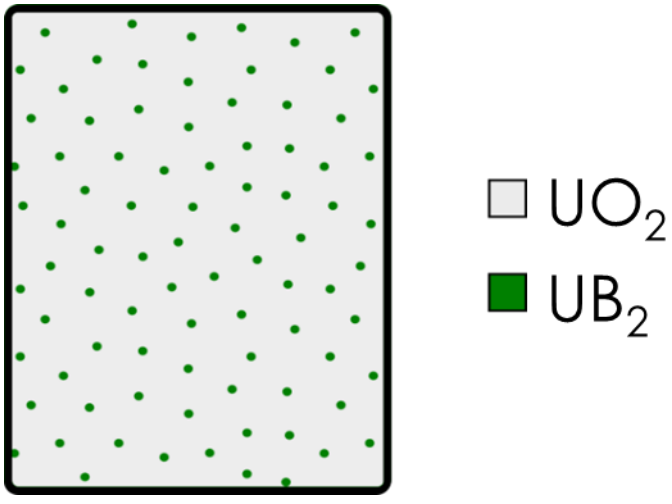

Figure 2.3: Conceptual representation of the proposed ATF pellet.

This thesis aims to address several of the knowledge gaps in the development of the composite fuel pellet, i.e.:

- Is it possible to prepare UB_2 from UO_2 with an industrially scalable and economical process?
- What is the chemical reactivity of UB_2 towards common materials in the nuclear industry and in oxidising environments?
- What is the chemical behaviour of fission products in UB_2?
- Does the thermal expansion coefficient of UB_2 allow for its integration in the UO_2 matrix?

3. Methodology

3.1. Thermodynamic modelling

The thermodynamic modelling of a chemical process is crucial in exploring and optimising possible pathways towards the synthesis of a chemical compound.
The variation in Gibbs free energy $\Delta G_{RXN}(p,T)$ associated with a chemical process is a widely used metric to evaluate its thermodynamic behaviour and is defined as follows:

$$\Delta G_{RXN}(p,T) = \Delta H_{RXN}(p,T) - T \cdot \Delta S_{RXN}(p,T) \quad 3.1$$

Where $\Delta H_{RXN}(p,T)$ and $\Delta S_{RXN}(p,T)$ are the associated variations in enthalpy and entropy, respectively, both depending on pressure p and temperature T [103]. A chemical process with a negative variation in Gibbs free energy is thermodynamically favourable and should occur spontaneously if allowed by reaction kinetics.

The variations in enthalpy and entropy can be calculated as follows through equations 3.2 and 3.3:

$$\Delta H_{RXN}H(p,T) = \sum c_i \cdot \Delta H_{f,i}(p,T) \quad 3.2$$

$$\Delta_{RXN}S(p,T) = \sum c_i \cdot S_i(p,T) \quad 3.3$$

Where c_i is the stoichiometric coefficient of the i-th species in the reaction being considered, $\Delta H_{f,i}(p,T)$ is its molar enthalpy of formation and $S_i(p,T)$ its molar entropy. Products have positive coefficients, while reactants have negative coefficients.

The available values for the molar enthalpy of formation and the molar entropy of chemical substances are usually referred to a temperature of 298 K and a pressure of 1 bar, meaning that corrections are required in order to account for their dependence on temperature and pressure should the process being considered occur in different conditions. The thermodynamic state

corresponding to 1 bar is referred to as the “standard state” and the thermodynamic functions are denoted by the superscript "$^{\ominus}$" (e.g. $H^{\ominus}(T)$, $S^{\ominus}(T)$, $G^{\ominus}(T)$).

Enthalpy and entropy are defined by the following equations in differential form:

$$dH = dQ + Vdp \tag{3.4}$$

$$dS = \frac{dQ_{rev}}{T} \tag{3.5}$$

Where Q_{rev} is the reversibly exchanged heat, V is the volume of the system and p its pressure. Many chemical reactions occur at constant pressure, so that dp is equal to zero. This means that, for a given pure substance, the reversibly exchanged heat in an infinitesimal step going from state A to state B is equal to its heat capacity at constant pressure C_p multiplied by the infinitesimal variation in temperature dT. This allows us to rewrite equations 3.4 and 3.5 as:

$$dH = C_p dT \tag{3.6}$$

$$dS = \frac{C_p dT}{T} \tag{3.7}$$

At constant pressure, H and S – and therefore G – only depend on temperature. Integration of equations 3.6 and 3.7 between states A and B affords equations 3.8 and 3.9, respectively:

$$H(T_B) - H(T_A) = \int_{T_A}^{T_B} C_p(T) \cdot dT \tag{3.8}$$

$$S(T_B) - S(T_A) = \int_{T_A}^{T_B} \frac{C_p(T)}{T'} \cdot dT \tag{3.9}$$

C_p depends on temperature, as explicitly stated in the equations above. While such a dependence could be neglected in the case of a small variation in temperature, it might become significant over broader ranges of temperature.

Enthalpy H and entropy S are thermodynamic functions of state, meaning that the change in their value only depends on the initial and final states and not on the path taken to go from one to the other (i.e., kinetic considerations are excluded).

Assuming that pressure is set at 1 bar (and therefore $H(p,T)$ and $S(p,T)$ are at their standard value) and the temperature of the initial state is 298 K, the corrected values for $H^{\ominus}(T)$ and $S^{\ominus}(T)$ can be obtained through equations 3.10 and 3.11:

$$H^{\ominus}(T) = H^{\ominus}_{298\,K} + \int_{298\,K}^{T} C_p(T') \cdot dT' \tag{3.10}$$

$$S^{\ominus}(T) = S^{\ominus}_{298\,K} + \int_{298\,K}^{T} \frac{C_p(T')}{T'} \cdot dT' \tag{3.11}$$

The $C_p(T')$ function for a given substance can be obtained by fitting the measurements of the molar heat capacity of a pure sample at different temperatures. In order to avoid ambiguity between the upper bound of integration at temperature T, the integration variable has been denoted as T'.

There are various possible expressions for the fitting function $C_p(T')$, with a class of them being represented by Shomate's equation and its variants. The original equation was devised in 1954 and only had three parameters due to computational limitations at the time [104]. In a very general form, the associated variations in standard enthalpy $H^{\ominus}(T)$ and standard entropy $S^{\ominus}(T)$ as functions of temperature can be calculated as follows from equations 3.12 and 3.13:

$$\Delta H^{\ominus}_{RXN}(t) = \sum c_i \left(A_i \cdot t + \frac{1}{2} B_i \cdot t^2 + \frac{1}{3} C_i \cdot t^3 + \frac{1}{4} D_i \cdot t^4 - \frac{E_i}{t} + F_i + M_i \ln(t) - \frac{N}{(2 \cdot t^2)} - \frac{P}{(3 \cdot t^3)} \right) \tag{3.12}$$

$$\Delta S^{\ominus}_{RXN}(t) = \sum c_i \left(A_i ln(t) + B_i \cdot t + \frac{1}{2} C_i \cdot t^2 + \frac{1}{3} D_i \cdot t^3 - \frac{E_i}{(2 \cdot t^2)} + J_i - \frac{M_i}{t} - \frac{N_i}{(3 \cdot t^3)} - \frac{P_i}{(4 \cdot t^4)} \right) \tag{3.13}$$

Where c_i is the stoichiometric coefficient of the i-th species. Products have positive coefficients, while reactants have negative coefficients.

Temperature is used in a reduced form t, which is equal to $T/1000$, where T is the thermodynamic temperature expressed in kelvins. This is done so that the coefficients are kept in a reasonable range of orders of magnitude and are readily comparable to understand their relative weights. The numerical values resulting from the calculations have units of kJ/mol for enthalpies and of J/mol·K for entropies.

The numerical values of coefficients A through P for all the chemical species were collected from the available literature and adapted as needed (e.g., by converting the coefficients into the appropriate units or combining data from multiple sources). The sources and the numerical values used in the calculations are detailed in tables of thermodynamic coefficients.

When one of the reactants or of the products is not in its the standard state, its Gibbs free energy changes according to equation 3.14:

$$\Delta G_i(\boldsymbol{K_i}, T) = \Delta G_i^{\ominus}(T) + RT \cdot \ln\left(a_i(\boldsymbol{K_i}, T)\right) \qquad 3.14$$

Where R is the universal gas constant expressed in the appropriate units (e.g. 8.314 J/mol·K [103]), $\boldsymbol{K_i}$ is a vector the components of which define the thermodynamic state of species i (i.e. total pressure, concentration of i, and concentrations of any other species that may interact with i) and a_i is a function of the thermodynamic state called the activity of i.

For ideal gases, the activity is equal to the ratio between the pressure of the gas and the standard pressure, as shown in equation 3.15:

$$\Delta G(p_i, T) = \Delta G^{\ominus}(T) + RT \cdot \ln\left(\frac{p_i}{p^{\ominus}}\right) \qquad 3.15$$

For real gases, pressure is replaced by fugacity by multiplying the pressure ratio by the fugacity coefficient, which is derived from empirical measurements.
For pure solids and liquids, the activity in the standard state is set at 1, so that the logarithm in equation 3.14 becomes zero. The effect of pressure on the activity of condensed phases is usually very small and can be neglected (i.e. < 1%) at pressures below 10 bar [105]. For ideal mixtures of solids and liquids (i.e., solid solutions and liquid solutions), the activity of a component is equal to its molar fraction in the mixture, while for non-ideal mixtures coefficients derived from empirical measurements are used to multiply the activity.

In this work all reactions are expected to occur at relatively low pressure and all condensed phases are assumed to be pure or to behave as ideal solutions.

Combining together equations 3.1, 3.2, 3.3, and 3.14 we obtain equation 3.16:

$$\Delta G_{RXN}(\boldsymbol{K}, T) = \Delta G^{\ominus}_{RXN}(T) + \sum c_i \cdot RT \cdot \ln\left(a_i(\boldsymbol{K_i}, T)\right) \tag{3.16}$$

Which can be transformed into equation 3.17 using the properties of logarithms:

$$\Delta G_{RXN}(\boldsymbol{f}, T) = \Delta G^{\ominus}_{RXN}(T) + RT \cdot \ln\left(\prod \left(a_i(\boldsymbol{K_i}, T)\right)^{c_i}\right) \tag{3.17}$$

The product inside the logarithm is called quotient of reaction and is usually indicated with *Q*. It represents the ratio between the product of the activities of the products and those of the reactants, each raised to the modulus of its stoichiometric coefficient. Considering a process of the type

$$n\ \mathrm{A} + m\ \mathrm{B} \rightarrow d\ \mathrm{X} + e\ \mathrm{Y} \tag{3.18}$$

Q can be written as:

$$Q = \frac{a_X^d \cdot a_Y^e}{a_A^n \cdot a_B^m} \tag{3.19}$$

At chemical equilibrium, the Gibbs free energy of reaction is zero, so that equation 3.17 can be rearranged as:

$$\Delta G^{\circ}_{RXN}(T) = -RT \cdot \ln\left(K_{eq}\right) \tag{3.20}$$

Since the value of Q is univocally defined at equilibrium, this value is called the equilibrium constant of the reaction, K_{eq}. Recalling equation 3.17 and combining it with equation 3.20 we can write:

$$\Delta G_{RXN}(\boldsymbol{f}, T) = RT \cdot \ln\left(\frac{Q}{K_{eq}}\right) \tag{3.21}$$

So that the variation in Gibbs free energy will be negative (and the reaction will be thermodynamically favourable) if $Q < K_{eq}$.

For a reaction occurring among condensed phases but with a single gaseous product, of the type indicated in reaction 3.22:

$$n\ \mathrm{A}_{(s)} + m\ \mathrm{B}_{(s)} \rightarrow d\ \mathrm{X}_{(s)} + e\ \mathrm{Y}_{(g)} \tag{3.22}$$

The expression of the reaction quotient is equal to the activity of the gaseous product Y if the condensed phases are assumed to behave ideally. Thus, it is possible to calculate the equilibrium partial pressure of species G above a reaction mixture. The reaction will proceed if the instantaneous partial pressure is below the equilibrium value.

3.2. Estimation of a lower bound to the reaction time for chemical reactions with gaseous by-products

Condensed-phase reactions are of paramount importance in the preparation of ceramic materials. Many of the chemical processes involved in the preparation of ceramics release gases which must be removed in order to drive the reaction forward. While the kinetics of such processes can usually be fully understood after a thorough empirical investigation, simple thermodynamic and mass balance considerations allow an estimate of lower bound for the time at temperature of a chemical synthesis of this kind.

In fact, these reactions cannot proceed faster than the gaseous by-products are removed. While the removal of said products may not be the rate-limiting step in such a process, its rate defines the upper bound of the overall reaction rate – and therefore, for a given amount of material, the lower bound of the required reaction time.

Let us consider a process of the type described in reaction 3.22. Thermodynamics govern the process and determine the equilibrium partial pressure of the gaseous species Y. Applying equation 3.20, the equilibrium partial pressure of Y at a given temperature can be calculated as

$$p_Y(T) = p^{\ominus} \cdot \exp\left(-\frac{\Delta G^{\ominus}}{e \cdot RT}\right) \qquad 3.23$$

Where $p_Y(T)$ is the partial pressure of Y, $p^{\ominus}$ is the standard pressure (i.e. 1 bar), $\Delta G^{\ominus}$ is the standard variation in Gibbs free energy associated with the process, R is the universal gas constant and T is the thermodynamic temperature at which the process occurs.
As the reaction proceeds, a flow of gas Y with a molar flow rate $\dot{n}_Y$ will be established from the reaction system to the volume of the furnace.

Let us assume that a flow of inert gas IG, with a molar flow rate $\dot{n}_{IG}$ is used to remove Y from the reaction environment and that the total pressure in the reaction environment is approximately 1 bar. These conditions are representative of those of a tube furnace operating with an atmospheric outlet and a slow-moving carrier gas.

Let us also assume ideal mixing between Y and the carrier gas and that a quasi-steady state is established, with the reaction rate being constant and the partial pressure of Y constantly equal to its maximum allowed value (i.e., the thermodynamic limit) throughout the whole reaction. These assumptions represent the case in which the inert gas stream is completely saturated with Y, so that the reaction can proceed as soon as a volume of saturated gas leaves from the outlet and is replaced from fresh inert gas from the inlet.
It is worth noting that the assumption of ideal mixing between Y and the carrier gas maximises the effectiveness of the removal of Y, thus making this case the upper bound to the reaction rate.

At the quasi-steady state, the molar fraction of Y in the outlet gas, X_Y, is equal to the ratio of the molar flow rate of Y to the total molar flow rate

$$X_Y = \frac{\dot{n}_Y}{\dot{n}_Y + \dot{n}_{IG}} \tag{3.24}$$

Under the assumptions above, the total pressure in the furnace or reaction vessel used for the synthesis is approximately equal to the atmospheric pressure (1 bar), so that the partial pressure of Y can be written as the product between its molar fraction of Y and the total pressure p_{atm}

$$p_Y = X_Y \cdot p_{atm} \tag{3.25}$$

Combining and rearranging equations 3.24 and 3.25 we obtain equation 3.26, describing $\dot{n}_Y$ as a function of $\dot{n}_{IG}$, p_Y, and p_{atm}

$$\dot{n}_Y = \dot{n}_{IG} \cdot \frac{p_Y}{p_{atm} - p_Y} \tag{3.26}$$

For the reaction to proceed to completion, referring to reaction 3.22, *e* moles of Y must be released per *c* moles of product C obtained. If n_C is the molar amount of product C that is expected from the process, the lower bound to the reaction time t_{MIN} is

$$t_{MIN} = \frac{e}{c} \cdot \frac{n_C}{\dot{n}_Y} = \frac{e}{c} \cdot \frac{n_C \cdot (p_{atm} - p_Y)}{\dot{n}_{IG} \cdot p_Y} \tag{3.27}$$

3.2.1. Example calculation

Let us consider the synthesis of zirconium diboride ZrB_2 in a tube furnace at 1200 °C under a flow of argon, according to the following reaction:

$$2\ ZrO_{2\,(s)} + B_4C_{\,(s)} + 3\ C_{\,(s)} \rightarrow 2\ ZrB_{2\,(s)} + 4\ CO \qquad 3.28$$

The details of the process are reported in Table 3.1. The value of $\Delta G^{\ominus}$ was calculated as detailed in Section 3.1, while the partial pressure of CO at equilibrium was calculated with equation 3.23.

Table 3.1: Process and thermochemistry data for the sample calculation.

Process data	**Thermochemistry data**
Temperature: 1200 °C	$\Delta G^{\ominus}$ at 1200 °C: + 142 kJ/formula
Furnace volume: 5 L	CO equilibrium partial pressure: 0.055 bar
Q_{Ar} = 20 L/h at 20 °C (0.832 mol/h)	Expected amount of ZrB_2: 1.5 g (13.3 mmol)

The minimum reaction time at 1200 °C can then be calculated applying equation 3.27:

$$t_{MIN} = \frac{4}{2} \cdot \frac{13.3\ mmol \cdot (1 - 0.055)\ bar}{832 \frac{mmol}{h} \cdot 0.055\ bar} = 0.55\ h = 33\ min \qquad 3.29$$

For the process conditions that we are considering, complete reaction cannot be achieved in less than 33 minutes (neglecting any reactions that may occur during temperature ramping from room temperature).

The methodology outlined above can be adapted to consider actively pumped vacuum furnaces if the flow rate and the ultimate vacuum of the vacuum pump are known.
The methodology has been used in all synthesis work in Sections 4, 5, and 6.

3.3. Density Functional Theory (DFT) simulations

The Vienna Ab-Initio Software Package (VASP) [106,107] and the Phonopy [108] package were used to simulate the thermodynamic properties of crystalline structures of interest using Density Functional theory (DFT). The thus-obtained properties were used in order to supplement the values available in the literature, with special attention to modelling the thermal expansion of UB_2.

VASP simulations were used to optimise the geometry of the crystalline structures of several substance of interest and to calculate their binding energy per formula unit. For the VASP calculations, the projector augmented wave (PAW) potentials [109] were used in conjunction with the generalised gradient approximation (GGA) exchange correlation functional described by Perdew, Burke and Ernzerhof [110].
In all calculations a convergence threshold of 10^{-8} eV was set for electronic minimisation, and a threshold of 10^{-7} eV/Å was set for geometric optimisation. The cut-off energy, representing the highest energy of the plane wave in the basis set used to describe the overall electronic wavefunction, was set to 550 eV for all calculations. A Γ-centred k-point mesh, indicating the sites at which the wavefunction is sampled in reciprocal space [111], was automatically generated for each cell with VASP, specifying a constant k-point separation of approximately 0.04 $Å^{-1}$ in reciprocal space. Convergence tests were carried out with respect to the cut-off energy and to the k-point density until subsequent increases resulted in changes that were smaller than 1 meV/atom. A Gaussian smearing of 0.08 eV was used in the calculations. The smearing parameter σ simulates the electronic temperature of the material (expressed in eV) and is used to define the occupancy of electron states close to the Fermi level, facilitating numerical integration and convergence of the VASP calculation, but at the price of slightly altering its result [112]. Representing a trade-off between calculation speed and accuracy, σ was chosen with a convergence test in which its value was increased up to the point at which the difference between the total electronic energy and the electronic free energy (with the difference being representative of the alteration caused by the smearing) was smaller than 1 meV/atom.

The crystalline structures of α-U [113], B [114], UB_2 [42] and UB_4 [42] were taken from the literature and relaxed under a constant pressure of 1 bar, allowing cell size, shape and volume to change.

No Hubbard correction was applied to account for electron localisation in U, UB_2 and UB_4, since elemental uranium is metallic and experimental and computational data show UB_2 [115,116] and UB_4 [116] to have no gap between the valence and the conduction band. While the absence of the band gap alone would not be sufficient to justify setting the value of the Hubbard parameter to 0 eV, the lack of electron localisation in UB_2 is also confirmed by the experimental observations of Yamamoto *et al*., which found that many of the magnetic and electric properties of UB_2 – including its being a Pauli paramagnet [117] – are characteristic of those of a material with itinerant 5*f* electrons [115,118] This methodology is consistent with the one used by Burr *et al*. [21] and by Evitts *et al*. in their simulation work on UB_2 [119].
No Hubbard correction was applied for boron, either, since its effect is usually negligible for elements containing only *s* and *p* electronic states [120].

The binding energy as calculated by VASP at 1 bar can be assimilated to the absolute standard enthalpy of the substance at a temperature of 0 K, since no lattice vibrations are included in the calculations.
Let E_i be the binding energy per mole of a given compound *i* as calculated by VASP; its enthalpy of formation at 0 K as derived by DFT, $\Delta H^{\circ}_{f-i,DFT}$, can therefore be calculated as the difference between the binding energy of the substance and the sum of those of its constituent elements

$$\Delta H^{\circ}_{f-i,DFT}(0\ K) = E_i - \sum c_j E_j \qquad 3.30$$

Where c_j and E_j are, respectively, the stoichiometric coefficient with which substance *j* features in compound *i* and its binding energy in its standard substance state.

The Phonopy package allows to include dependency on temperature in the calculations above by using the quasi-harmonic approximation (QHA). Under the QHA, the potentials to which the atoms in the crystal lattice are subjected are assumed to be harmonic for all values of the lattice parameters, so that the force constants (on which the energy stored in the vibrational degrees of freedom depends) can be calculated from a quadratic fit of the potentials against the relevant degrees of freedom. The frequencies of the phonons depend in turn on the force constants and on the wave vector associated to the vibrational mode through a dispersion relation of the general form of equation 3.31:

$$(\mathbf{C}, \mathbf{q}) \rightarrow \omega_i(\mathbf{q}) \qquad 3.31$$

Where $\mathbf{C}$ is a vector containing all the relevant force constants as its components, $\mathbf{q}$ is the wave vector, and $\omega_i(\mathbf{q})$ is the frequency of the *i*-th vibrational mode associated with wave vector $\mathbf{q}$. The dependency of the frequency on the force constants is omitted, as they are assumed to be constant throughout the crystal lattice.

The dispersion relation of equation 3.31 cannot be classed as a function, since a single $(\mathbf{C}, \mathbf{q})$ pair can be associated with multiple oscillation modes, with each mode corresponding to a phonon. Phonons can be classed into acoustic and optical phonons, with acoustic phonons involving the in-phase oscillation of the alternating nodes of the crystal lattice, while the oscillation is out of phase in optical phonons. Optical phonons are thus named because in lattices composed of particles with opposite charges (such as those of ionic solids) they generate dipoles in the material, allowing it to emit and absorb electromagnetic radiation [121].

The energy E_i associated with a single phonon vibrational mode of frequency ω_i associated with a wave vector $\mathbf{q}$ is then calculated through equation 3.36 as that of a quantum harmonic oscillator:

$$E_i(\mathbf{q}) = \left(n + \frac{1}{2}\right)\hbar\omega_i(\mathbf{q}) \qquad 3.32$$

Where n is the number of phonons occupying the vibrational mode and $\hbar$ is the reduced Planck constant.

The total vibrational energy $E_{vib,tot}(T)$ of an extended lattice containing a large number of oscillators and averaged over a long time (relative to the microscopic fluctuations) can then be calculated as a function of temperature T through equation 3.33 as the sum of all the energies of each phonon mode over all wave vectors $\mathbf{q}$, with each wave vector being able to support multiple modes (or branches), denoted with the subscript i, and with each vibrational mode being weighted by its occupancy averaged over time, denoted as $\langle n\rangle(\omega_i(\mathbf{q}), T)$:

$$E_{vib,tot}(T) = \sum_{\mathbf{q}}\sum_{i}\left(\langle n\rangle(\omega_i(\mathbf{q}), T) + \frac{1}{2}\right)\hbar\omega_i(\mathbf{q}) \qquad 3.33$$

The average occupancy of each mode depends in turn on the energy of the mode itself as written in equation 3.36 and on the temperature of the system, according to the Bose-Einstein statistic described in equation 3.34:

$$\langle n \rangle(\omega_i(\mathbf{q}), T) = \frac{1}{e^{\frac{\mathrm{E}_i(\mathbf{q})}{k_B T}} - 1} \qquad 3.34$$

Where k_B is Boltzmann's constant.

It must be noted that, while harmonic potentials are reasonable approximations of the local shape of a potential well in the immediate surroundings of its minimum, they are not able to accurately reproduce the shape of heavily distorted potential wells or to capture the effects of asymmetry, including – notably – that which is associated with crystal defects [122]. The QHA is therefore unable to accurately reproduce the phenomenon of phonon-defect scattering, which shortens the average lifetime of phonons in a material. With the phonon lifetime being correlated to thermal conductivity, simulations of materials neglecting the phonon-defect scattering tend to overpredict the thermal conductivity when compared to experimental data, as reported by Evitts *et al*. in their study of the thermal conductivity of UB_2 [119].

In order to determine the force constants as functions of cell size, the relaxed unit cells obtained from the first step were first uniformly rescaled along their dimensions to obtain a collection of crystal cells with lattice parameters with lengths ranging between (1-*x*) and (1+*x*) times the original ones. A value of *x* of 0.05 and a step size of 0.01 were used in the present work, obtaining a total of 11 scaled, relaxed unit cells, including the non-rescaled one (scaling factor = 1). The explicit, manual alteration of the lattice parameters is required to simulate the phenomenon of thermal expansion, as a molecular dynamic simulation of a harmonic potential would not result in the change of the atomic positions in the lattice.

The rescaled unit cells were then expanded to build 4x4x3 supercells in the case of UB_2 and 1x1x2 supercells in the case of UB_4, containing respectively 144 and 60 atoms (referring to Table 2.4 for lattice parameters and formulas per unit cell), from which the force constants were calculated with VASP in constant-volume calculations by perturbing the position of individual atoms in the supercell and thus sampling the potential. Performing this operation on supercells as opposed to unit cells allows to reduce the effect of the perturbation on the overall simulated crystal lattice when periodic boundary conditions are applied [123].

The expansion factors used to build the supercells and were chosen so that the values of the lattice parameters of the supercell in the *a* and *c* directions would be roughly equal (as exemplified in

Table 3.2 in the case of UB_2). The length matching between the *a* and *c* directions allows to maximize the minimum distance between periodic images in all directions for a given supercell volume, and thus minimize finite-size effects [123].

Table 3.2: Lattice parameters of the unscaled unit cells of UB_2 and of the resulting expanded supercells.

	***a* direction**	***c* direction**
Unit cell lattice parameter (non-rescaled)	3.1302 Å	3.9878 Å
Expansion factor	4	3
Supercell lattice parameter (non-rescaled)	12.5208 Å	11.9634 Å

The force constants were input into Phonopy, which uses QHA to determine the energy of the phonons associated with the lattice vibrations, which depends on the geometry of the crystal lattice and on the average energy of the vibrating atoms (i.e., on temperature).

For a given substance, the calculated Gibbs free energy of its simulated cell or supercell will then contain a term depending on the binding energy of the static lattice, $E_{lattice}(V)$, which in turn depends only on the volume of the cell, and a term that depends on the phonon energy, $E_{phonons}(V,T)$, as described in equation 3.33, which instead depends on the volume of the cell (through the shape of the potential wells in which atoms sit and on their force constants) and on the temperature of the system:

$$G(V,T) = E_{lattice}(V) + E_{phonons}(V,T) \qquad 3.35$$

The Phonopy package uses the collection of rescaled supercells to sample the Gibbs free energy as a function of cell volume and temperature. Fitting of the Gibbs free energy of the sampling points as a function of volume and minimisation of the fitting function allows to determine the equilibrium cell volume as a function of temperature.

A typical output of the Phonopy package is shown in Figure 3.1, where the free energy curves as a function of volume for a series of temperatures are presented on the left, while the curve representing the cell volume as a function of temperature (obtained by connecting the minima of the curves on the left) is presented on the right.

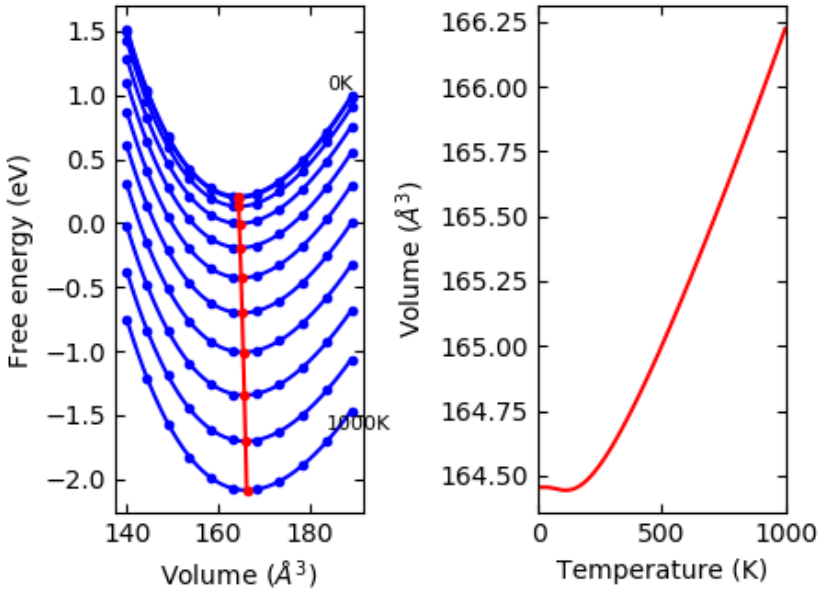

Figure 3.1: Typical free energy curves as a function of volume for a series of temperature (left) and V(T) curve, as generated by Phonopy.

The phonon properties can be calculated from the equilibrium volume at each temperature, including the heat capacity of the substance. The data points of the heat capacity values at different temperatures can then be fitted to obtain a $C_p(T)$ function analogous to those used in Section 3.1.

Applying equation 3.8 to equation 3.30 it is possible to calculate the enthalpy of formation at 298 K of any simulated compound through equation 3.36, remembering that the heat content of its constituent elements in their elemental form must calculated as well and subtracted from the result, as shown in the qualitative thermodynamic cycle in Figure 3.2, where q_R is the heat content of the reactants and q_P is the heat content of the products (the elements and the compound, respectively, in the case of equation 3.36).

$$\Delta H^{\ominus}_{f-i,DFT}(298\ K) = \Delta H^{\ominus}_{f-i,DFT}(0\ K) + \int_{0\ K}^{298\ K} C_{p,i}(T) \cdot dT - \sum c_j \cdot \int_{0\ K}^{298\ K} C_{p,j}(T) \cdot dT \qquad 3.36$$

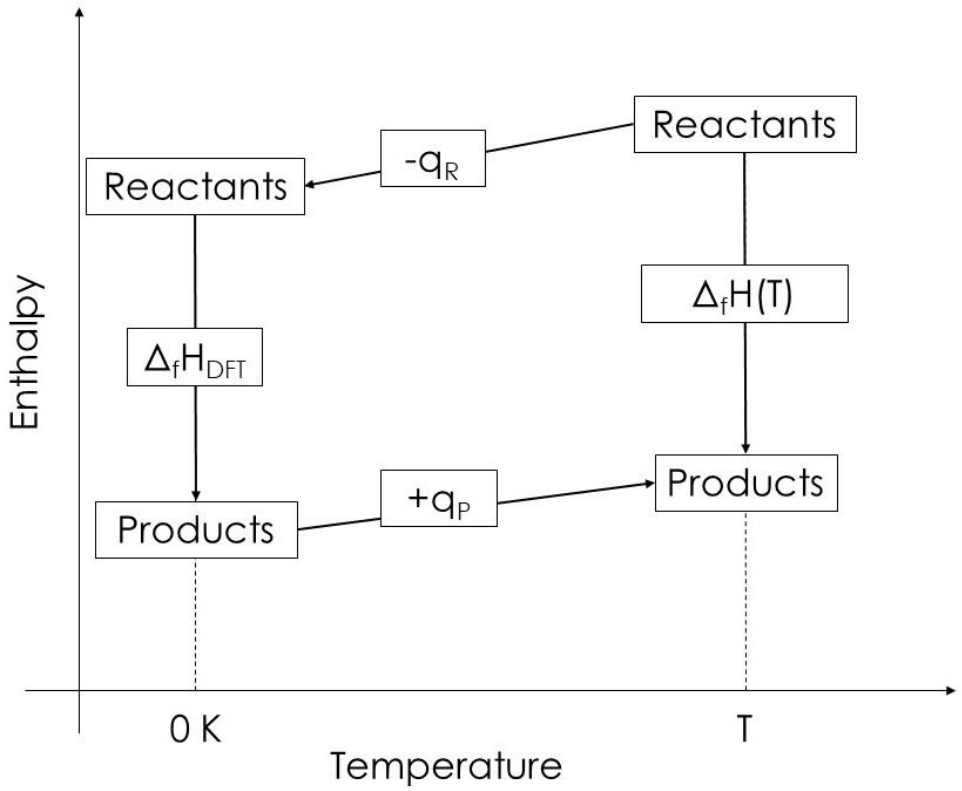

Figure 3.2: Thermodynamic cycle used to calculate the standard enthalpy of formation.

Equation 3.11 can be rearranged to obtain equation 3.37, which allows to calculate the standard entropy at 298 K of the simulated substances:

$$S^{\ominus}_{298\,K} = S^{\ominus}_{0\,K} + \int_{0\,K}^{298\,K} \frac{C_p(T)}{T} \cdot dT \qquad 3.37$$

Knowing that the entropy of perfect crystals at 0 K is zero, according to the Third Principle of Thermodynamics [103]:

$$S^{\ominus}_{0\,K} \overset{\text{def}}{=} 0 \qquad 3.38$$

The method above was used to calculate the values of molar enthalpy of formation and molar entropy of UB_2 and UB_4 through DFT and QHA. The values were then benchmarked against the available literature values, finding good agreement, as shown in Table 3.3. The agreement suggested that other properties of the compounds were simulated reliably.

Table 3.3: Calculated standard molar enthalpy of formation and standard molar entropy at 298 K for UB_2 and UB_4 and literature values.

Substance	$\Delta H^{o}_{f,\ 298\ K}$ **(kJ/mol)**		$S^{o}_{298\ K}$ **(J/mol·K)**	
	DFT	**Literature**	**DFT**	**Literature**
UB_2	-169.6	-164.4 [124]	55.8	54.5 [124]
UB_4	-245.7	-234.2 [124]	67.8	68.4 [124]

Finally, the data points providing the equilibrium volume of the cell as a function of temperature can be fitted to obtain a $V(T)$ function, which can be differentiated to obtain the volumetric expansion coefficient, $\alpha_V(T)$ according to equation 3.39:

$$\alpha_V(T) = \frac{1}{V}\left(\frac{\partial V}{\partial T}\right)_p \qquad 3.39$$

Where subscript p denotes that the partial derivative with respect to temperature is taken at constant pressure.

The DFT-QHA method described above assumes that the thermal expansion occurs isotropically, as the lattice parameters of the cells are scaled uniformly. However, this treatment may not be representative of the anisotropic, layered structure of UB_2. The results of the isotropic thermal expansion calculations are presented and discussed in Section 6.7, together with a modified approach that allows for anisotropy.

The workflow of the DFT-QHA simulations is summarised in Figure 3.3, which shows how the potentials and the crystal structures available in the literature are processed to obtain several thermodynamic properties of the selected substances.

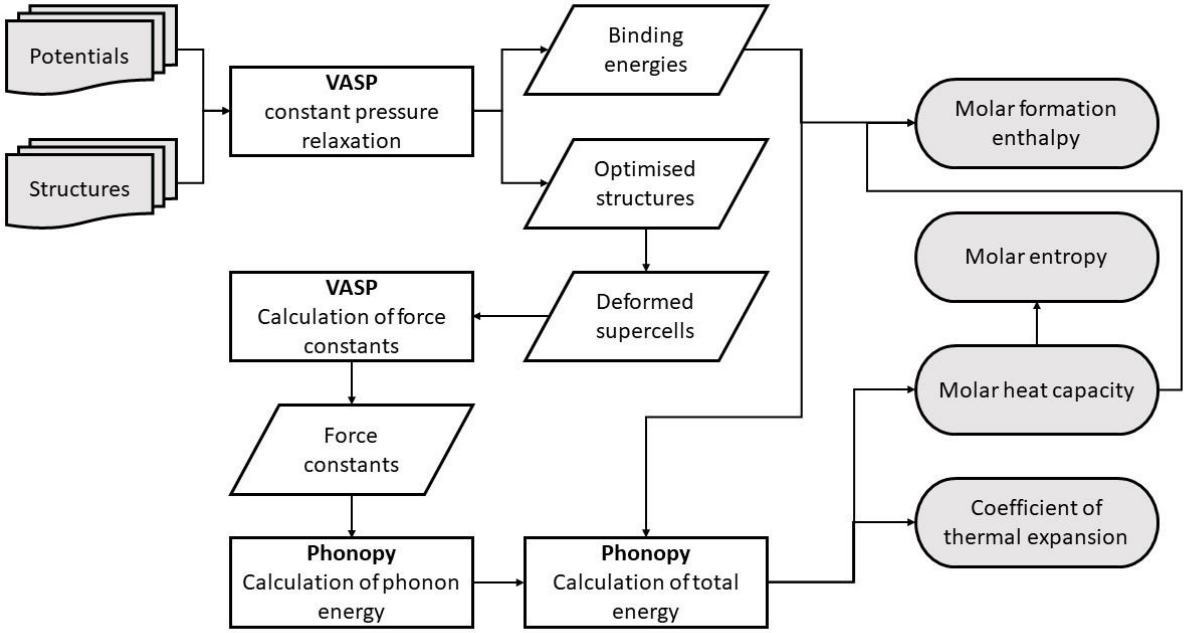

Figure 3.3: Workflow of the DFT-QHA simulations.

3.4. Synthesis and characterisation of materials

The experiments entailed the preparation of tungsten, uranium, and zirconium compounds via, high-temperature, solid-state reactions. The reactants were mixed in powder form, reacted at high temperature in furnaces, and mainly characterised via X-ray diffractometry (XRD).

3.4.1. Materials used

The reactants and auxiliary gases used in the synthesis experiments are detailed in Table 3.4.

Table 3.4: Suppliers and purities of the materials used in the synthesis experiments.

Material	Supplier	Purity
U_3O_8	British Drug Houses Ltd (now Merck)	99.9% (metals basis)
WO_3	Sigma	99.9% (metals basis)
B_4C	Sigma	98%
B_2O_3	Sigma	99.98%
C	Merck	99.5%
N_2	BOC	99.998% (incl. Ar traces)
Ar	BOC - Pureshield	99.998%
H_2 in Ar (5% mixture)	BOC- Specshield	99.9%
Synthetic air	BOC	21.49% O_2 in N_2
Zinc stearate spray	CRC Industries Ltd	N.A.

3.4.2. Preparation of reaction mixtures

The reactants were weighed on analytical balances (division: 0.1 mg) in batches with a total mass of approximately 1-5 g. Uranium work was carried out in an argon-filled, positive pressure glovebox (Δp = 3 mbar; $[O_2] < 0.5$ ppm; $[H_2O] < 0.5$ ppm, shown in Figure 3.4), while tungsten work was carried out on an open bench.

The reactant with the smallest required mass was weighed first, so that the weights of the others could be adjusted with greater relative precision to maintain the stoichiometric ratio.

For the uranium work, the reactant powders were pre-mixed in an agate mortar with an agate pestle and subsequently dry-milled in a tungsten carbide jar using tungsten carbide balls (4 mm diameter, with a powder-to-balls mass ratio approximately 1:15) at 150 rpm for 1 hour 30 minutes using a Retsch PM100 planetary ball mill.

For tungsten work, the reactants were hand-ground together in an agate mortar with an agate pestle.

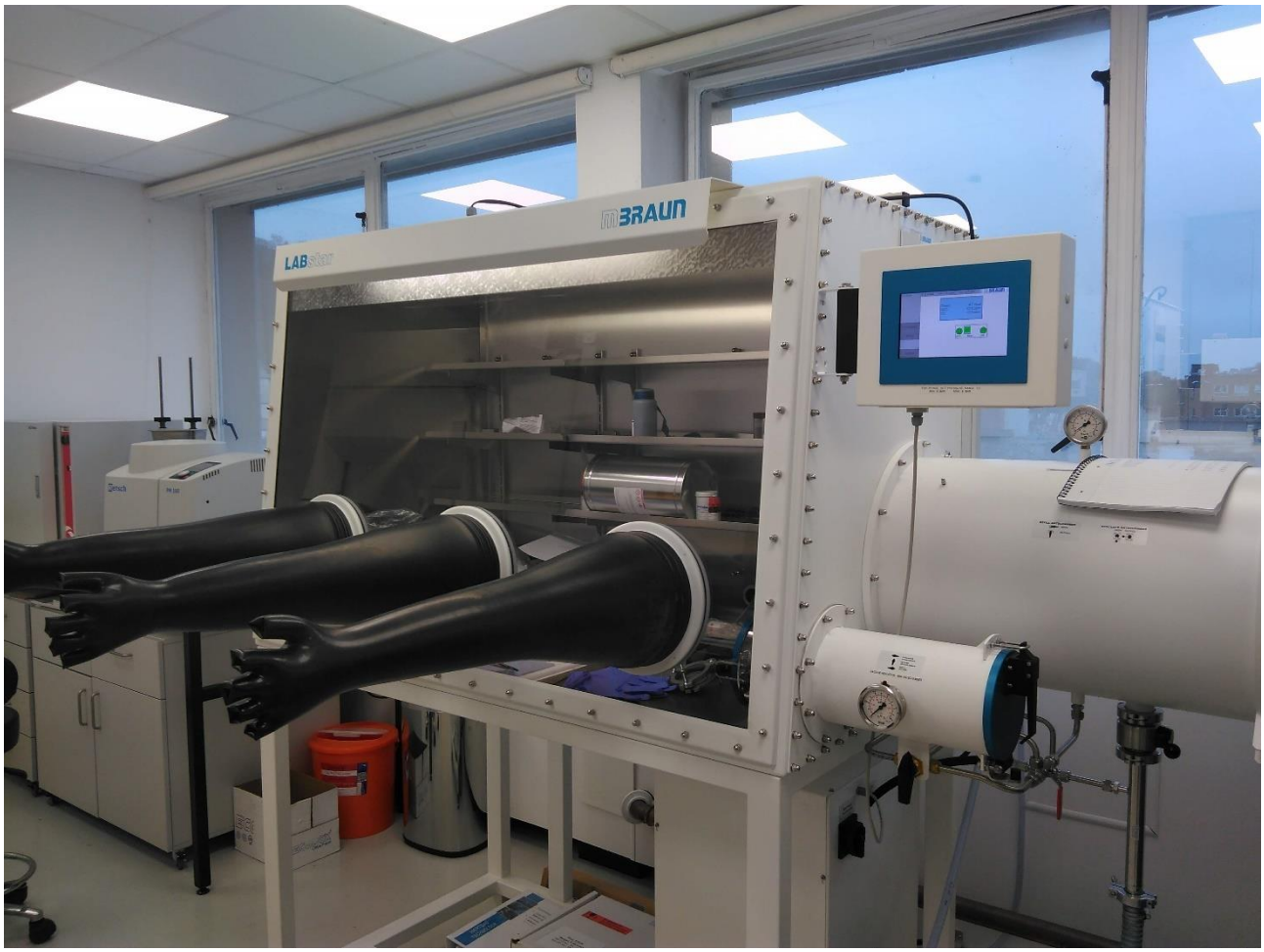

Figure 3.4: The positive pressure glovebox.

3.4.3. Production of pellets

The powder mixtures of solid reactants for synthesis work were reduced into pellets for ease of handling, to improve contact among the solid reactants, and, for radioactive materials, for ease of containment and to reduce the risk of surface contamination and suspension in air from loose powders.

For uranium work, the solid mixtures of reactants were then uniaxially compacted into pellets at a pressure of 250 MPa in a 10 mm diameter stainless steel die (compacting force: 2 ton-force) lubricated with zinc stearate spray.

For tungsten work, the solid mixtures of reactants were uniaxially compacted into pellets at a pressure of 500 MPa in an 8 mm diameter stainless steel die (compacting force: 2.5 ton-force) lubricated with zinc stearate spray.

3.4.4. High-temperature synthesis

The synthesis experiments were carried out in a Carbolite Gero alumina tube furnace (shown in Figure 3.5) and in a Carbolite Gero tungsten-molybdenum-lined chamber furnace (shown in Figure 3.6). Both furnaces are electrically heated and can be run in atmospheres with low oxygen potentials (inert or reducing gas for the tube furnace; inert or vacuum for the chamber furnace).

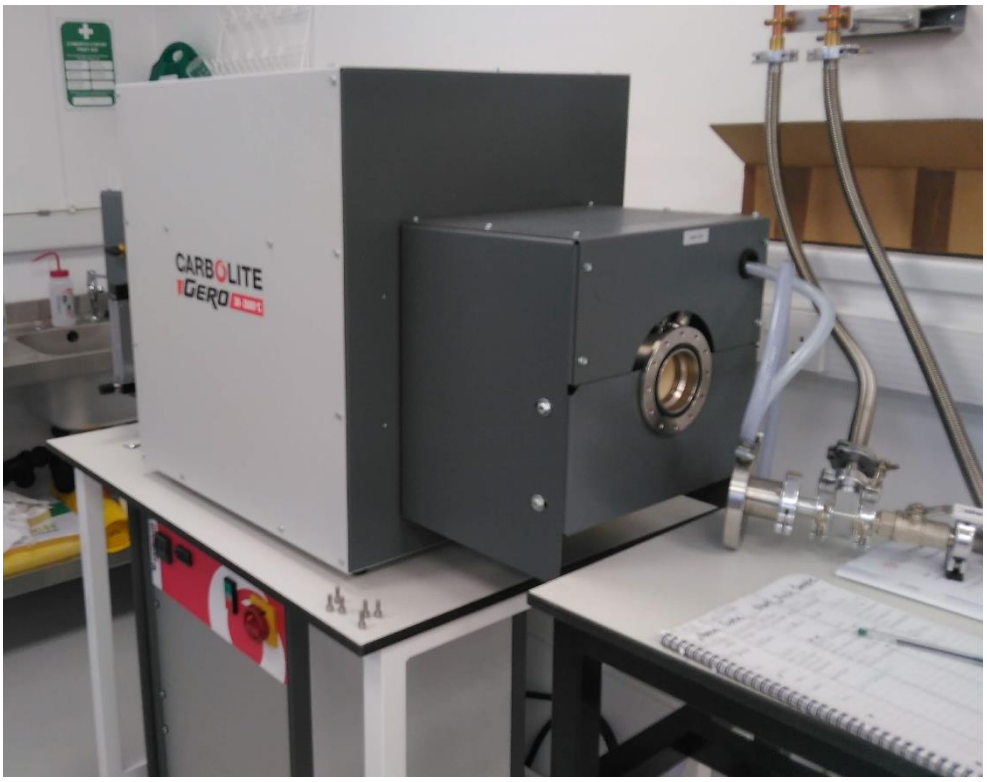

Figure 3.5: The tube furnace.

Figure 3.6: The chamber furnace.

3.4.4.1. Tube furnace

The carrier gas in the alumina tube furnace could be chosen between high-purity argon or 5% H_2 in argon (see Table 3.4). The inner volume of the tube was estimated to be 5 L based on its linear dimensions (80 mm inner diameter; 1000 mm length) and the flow rate of the carrier gas could be adjusted by means of a flow regulator between 5 L/h and 20 L/h. Before each synthesis the furnace was flushed for 1 h 30 m with carrier gas at room temperature at a flow rate of 20 L/h, meaning that 6 equivalent volumes of gas were delivered to displace the air. Treating the furnace like a Continuous-flow Stirred-Tank Reactor (CSTR) [125], assuming ideal mixing in the tube and no backflow through the exhaust, the residual oxygen content at the beginning of the temperature ramp can be estimated as 0.054%, or 540 ppm using equation 3.40

$$[O_2](t) = [O_2]_{AIR} \cdot e^{-\frac{t}{\tau}} + [O_2]_{IG} \cdot \left(1 - e^{-\frac{t}{\tau}}\right) \quad 3.40$$

Where $[O_2](t)$ is the concentration of oxygen in the furnace at time *t*, $[O_2]_{AIR}$ is the concentration of oxygen in air (assumed to be 21% [126]), $[O_2]_{IG}$ is the concentration of oxygen in the inert gas (assumed to be 20 ppm, according to Table 3.4), and τ is the average residence time in the furnace, which is defined as the ratio between the volume of the furnace and the volumetric flow rate of the gas and which has a value of 0.25 h in the present case. Equation 3.40 can be rearranged as follows:

$$[O_2](t) = ([O_2]_{AIR} - [O_2]_{IG}) \cdot e^{-\frac{t}{\tau}} + [O_2]_{IG} \quad 3.41$$

The concentration of oxygen as a function of time, as calculated by equation 3.41, is plotted in Figure 3.7 (in blue), together with the typical temperature profile of the early stages of a synthesis experiment in the tube furnace (in red).

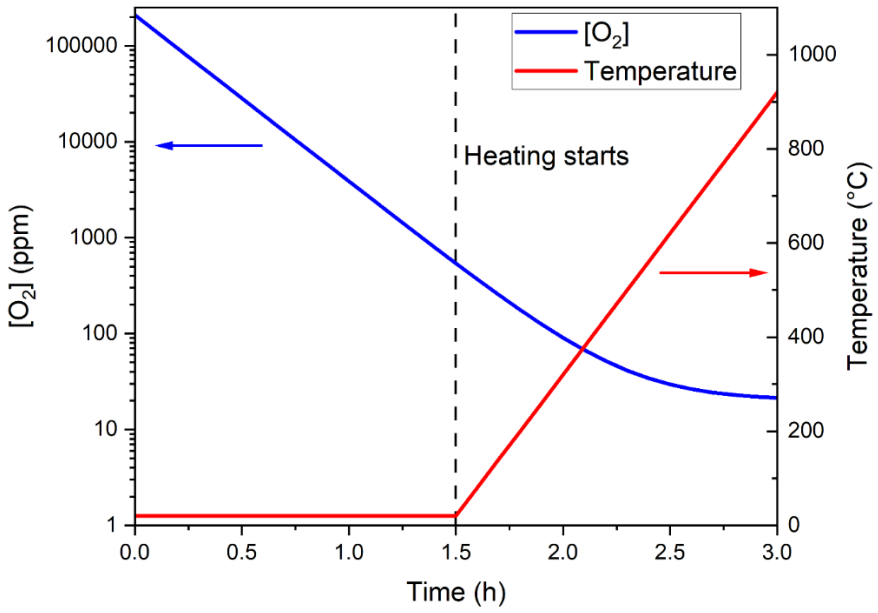

Figure 3.7: Calculated oxygen concentration and temperature profile in the tube furnace during purging and the initial heating phase of a typical run

It is worth noting that the model above represent the worst case for the residual oxygen content, as it models the tube as a continuously-stirred tank reactor (CSTR); the other bounding case is the approximation of the plug flow reactor (PFR), in which a single equivalent volume of gas would be sufficient to completely displace the original air contained in the tube [125]. The CSTR model was deemed more realistic owing to the long mixing time that the slow flow of gas allows.

For synthesis work in the tube furnace, ascending and descending ramp rates of 10 °C/min were used across the whole temperature range.

Alumina crucibles (Almath Crucibles Ltd) were used for synthesis work in the alumina tube furnace.

3.4.4.2. Chamber furnace

The chamber furnace was fitted with a vacuum pump capable of providing an ultimate vacuum pressure of $6 \cdot 10^{-5}$ bar. The pressure in the chamber was monitored by means of a digital pressure gauge with a division of 1 mbar. The accuracy of the pressure gauge was then estimated as half of

the division, or $5 \cdot 10^{-4}$ bar. The residual pressure inside the vacuum chamber was therefore estimated to lie between $6 \cdot 10^{-5}$ and $5 \cdot 10^{-4}$ bar.

Before each synthesis, three vacuum-nitrogen cycles were performed to remove air from the furnace; in each cycle, an additional pumping time of 1 minute was applied after the pressure gauge read 0 mbar. Assuming that the impurities in the nitrogen purge gas are due to oxygen (see Table 3.4) and based on the ultimate vacuum of the pump, the residual concentration of oxygen at the beginning of a synthesis in actively pumped vacuum was estimated to be between 1 and 10 ppb.

For synthesis work in the chamber furnace, ascending and descending ramp rates of 10 °C/min were used below 1500 °C, while ramp rates of 5°C/min were used above 1500 °C.

A molybdenum crucible (Goodfellow) was used for synthesis work of UB_2 in the vacuum furnace, given reports of adverse reactions of uranium diboride with alumina [127]. A zirconia crucible (Almath Crucibles Ltd) was used as a barrier layer between the molybdenum crucible and the Mo-W alloy of the bottom plate of the furnace in order to prevent diffusion bonding from occurring between the two.

During early experiments, one UB_2 sample reacted with the bottom of the molybdenum crucible and completely fused with it, leaving a coating which proved to be remarkably stable with respect to prolonged contact with uranium borides. Based on the literature and thermodynamic data discussed in Section 6, it is likely that the bottom layer of the crucible was composed of uranium molybdenum boride ($UMoB_4$).
Based on thermodynamic considerations again reported in Section 6, other crucible materials (e.g. tantalum, graphite) were ruled out because of interactions either with their contents or with the vacuum furnace's tungsten lining and the thus-coated crucible was used for the synthesis of UB_2.

3.4.5. Analysis of materials through X-ray Diffraction (XRD)

Solid materials were analysed via X-ray diffractometry (XRD) using a Malvern Panalytical Aeris Research Edition X-ray diffractometer, shown in Figure 3.8.
The powders to be analysed were ground in an agate mortar with an agate pestle and were placed on a silicon zero-background holder. For uranium-bearing powders, the grinding of the powders and

the loading of the sample holder were performed in the glovebox (see Section 3.4.2) and a Malvern inset for air-sensitive samples was used, with a Kapton film separating the powder from the environment.

The acquisition parameters were as follows:

- Cu anode – K_α wavelength, with $\lambda = 1.5406$ Å;
- step size: 0.01 ° 2θ;
- acquisition time: 49.725 seconds per step.

Phase analysis of the diffraction patterns was performed with the Malvern Panalytical HighScore Plus software.

The relative uncertainty on the diffraction spacing d of the crystalline phases as measured by XRD was calculated according to equation 3.42, obtained by differentiating Bragg's law [128]:

$$\left|\frac{\Delta d}{d}\right| = \frac{\cos(\theta)}{\sin(\theta)} \cdot \Delta\theta \qquad 3.42$$

Where θ is the angle at which the maximum of the diffraction peak occurs and $\Delta\theta$ is one half of the step size of the diffractometer (expressed in ° 2θ).

The measurements of the lattice parameter were assumed to be uniformly distributed in the $(d - \Delta d; d + \Delta d)$ interval, giving rise to a rectangular distribution, for which the standard deviation can be calculated according to equation 3.43 [129]:

$$\sigma = \frac{1}{\sqrt{3}} \cdot \left|\frac{\Delta d}{d}\right| \qquad 3.43$$

Quantitative phase analysis, performed by the Malvern Panalytical HighScore Plus software, was used to determine the composition of samples. Considering the limitations associated with the quantitative analysis of mixtures containing substances with widely varying X-ray extinction coefficients, only the relative composition of phases of similar chemical makeup was assessed; in particular, only the heavy-metal containing phases were considered for quantification [128] and phases containing only light elements (in particular boron oxides, boron carbide, and elemental carbon) were excluded from the analysis when detectable.

3.4.6. Analysis of materials trough Thermo-Gravimetric Analysis (TGA)

The mass change associated with chemical and physical changes of the materials was measured by means of Thermo-Gravimetric Analysis (TGA) using a Netzsch Jupiter 449A F3 STA (Simultaneous Thermal Analyser), shown in Figure 3.9.

An instrument-specific alumina cup with a volume of 3.4 mL (Netzsch) was used in the experiments.

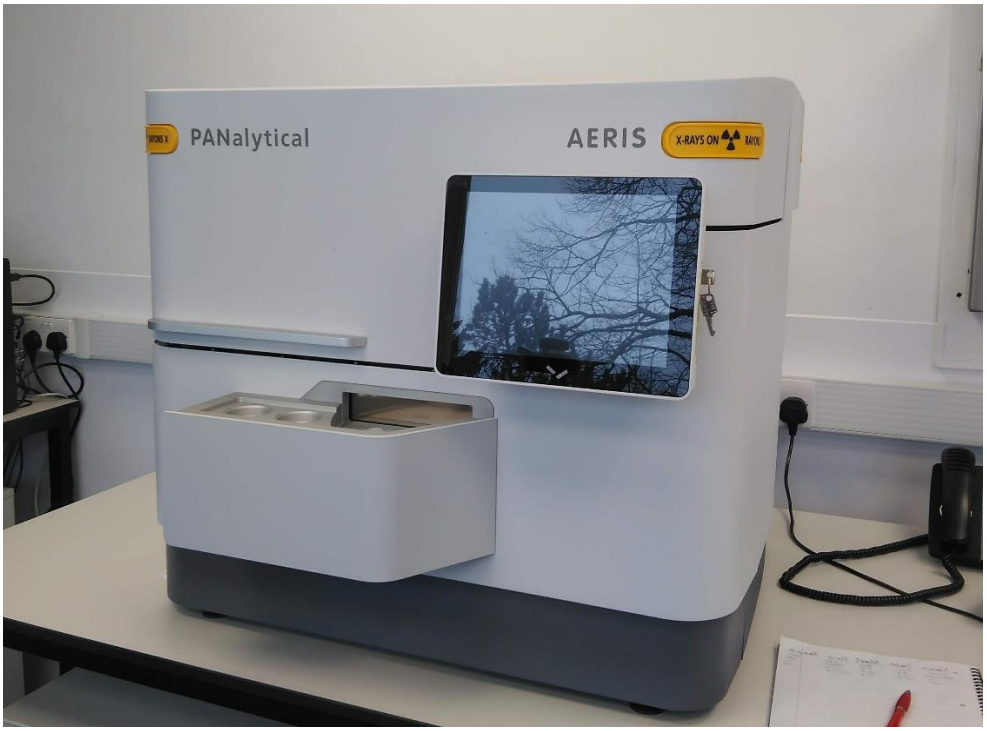

Figure 3.8: The X-ray diffractometer.

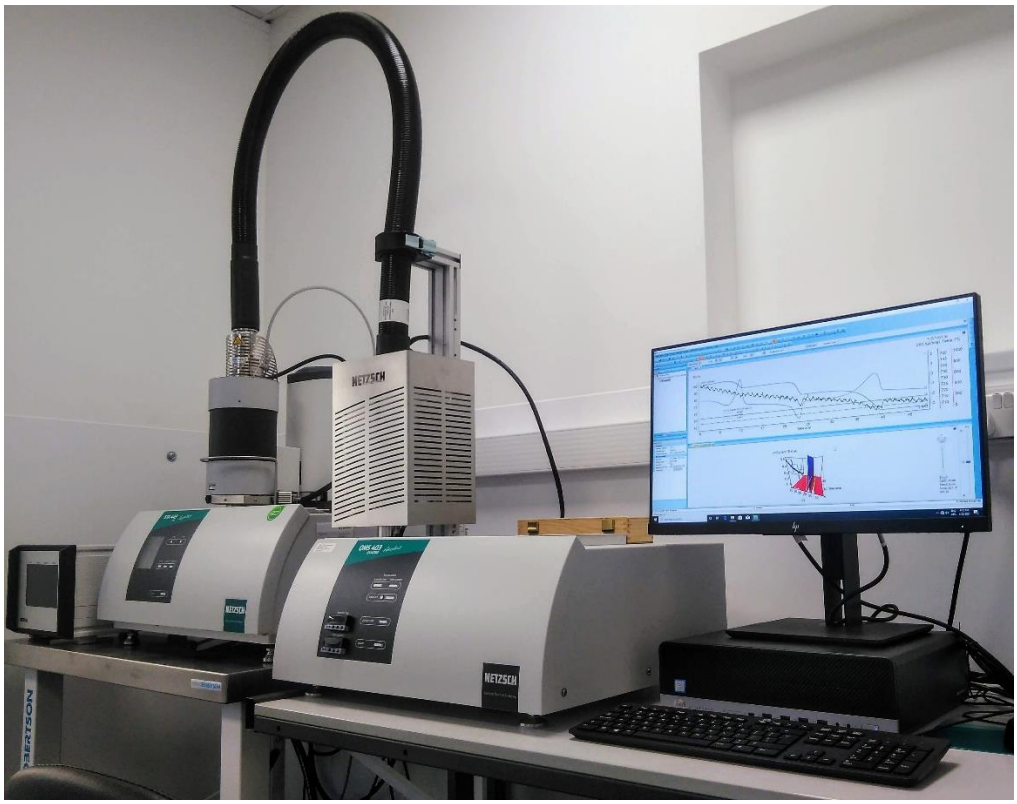

Figure 3.9: The Simultaneous Thermal Analyser.

3.4.7. Synthesis and characterisation of uranium dioxide

Uranium dioxide (UO_2) was used as a feedstock in uranium work and was prepared from the hydrogen reduction of U_3O_8 powder (see Table 3.4). The U_3O_8 powder was hand-ground in an agate mortar in an Ar glove box and then pressed into a pellet with the method described in Section 3.4.3. The pellet was then placed in an alumina crucible and fired in the tube furnace (700 °C, 2-hour dwell, 10 °C/min ramping rate) under a flow of 5% H_2 in argon at near-atmospheric pressure. A brick-red solid was obtained, as shown in Figure 3.10.

Only crystalline UO_{2+x} ($Fm\bar{3}m$)was detected by XRD analysis of the products, as shown in Figure 3.11. The lattice parameter of UO_{2+x} was calculated to be 5.466 Å from the Rietveld analysis.
The correlation between lattice parameter and hyperstoichiometry reported by Elorrieta *et al.* [130] allowed to estimate its stoichiometry as $UO_{2.05}$. The slight oxygen hyperstoichiometry was accounted for in the subsequent synthesis experiments; all written reactions refer to UO_2 for simplicity and readability purposes.

The estimate of the degree of hyperstoichiometry was corroborated by TGA, with a sample of UO_{2+x} being oxidised in flowing synthetic air up to 400 °C. A flow rate of 100 mL/min of synthetic air (BOC – see Table 3.4) and a heating rate of 5 °C/min were used.

The UO_{2+x} sample was analysed in powder form, with a mass of 1.4860 g. The mass profile, shown in Figure 3.12, registered a two-step mass increase, with the first step likely corresponding to oxidation to U_4O_9 and the second and final one to U_3O_8 [131]. Only the mass plateau associated to U_3O_8 (corresponding to a mass gain of 54.35 mg, or 3.66% of the original mass) was used to estimate the degree of hyperstoichiometry of the initial sample, due to the plateau of U_4O_9 not being fully developed. The calculations returned a value of x = 0.05, considering reaction 3.44 as the overall process:

$$3\ UO_{2+x\ (s)} + \left(1 - \frac{3}{2}x\right) O_{2\ (g)} \rightarrow U_3O_{8\ (s)} \qquad 3.44$$

Figure 3.10: UO_{2+x} prepared from the hydrogen reduction of U_3O_8.

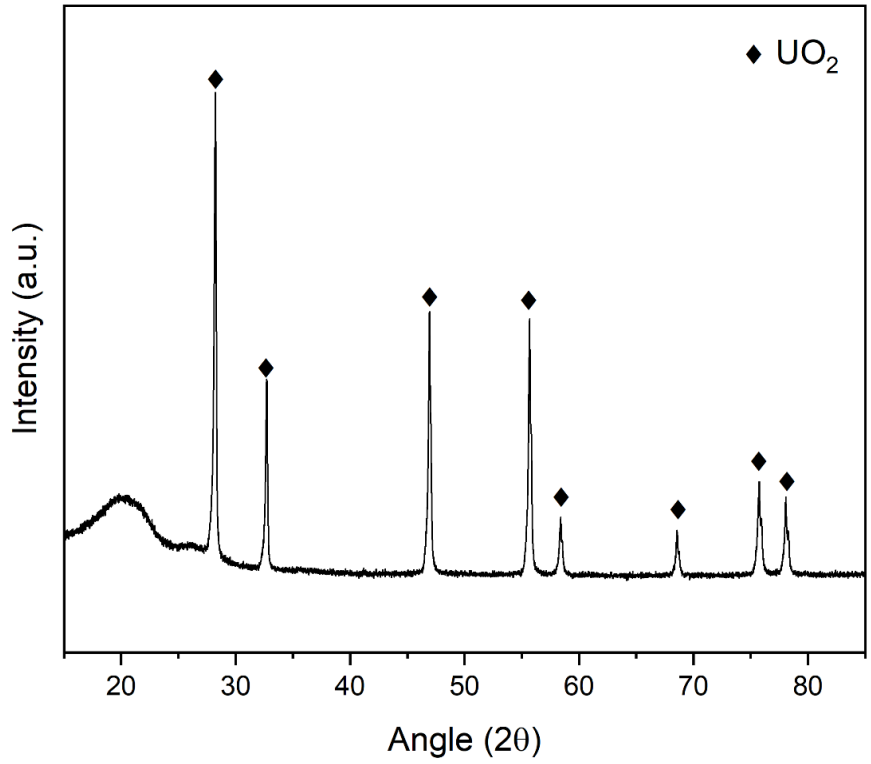

Figure 3.11: Diffraction pattern of a typical sample of reduced $UO_{2.05}$.

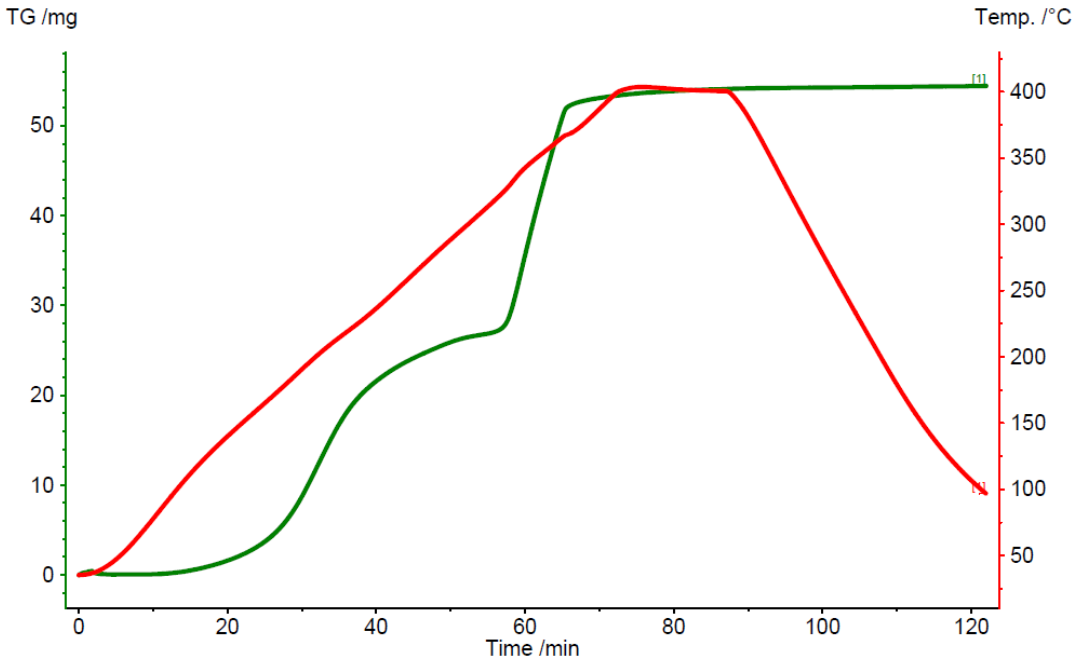

Figure 3.12: Mass profile of the UO_{2+x} sample (in green) and temperature (in red) during the TG analysis.

4. Modelling and experiments on the synthesis of uranium borides

The possibility of being manufactured on a large scale and at relatively low cost is critical for the success of a nuclear fuel. In this chapter, several possible synthetic pathways towards UB_2 from uranium hexafluoride (UF_6) and uranium dioxide (UO_2) have been assessed for their feasibility.

UO_2 and UF_6 were chosen as starting points for their ubiquitousness in the nuclear industry. Thermodynamic predictions on the favourability of the pathways (formulated with the methods described in Section 3.1) and practical considerations on the possible industrial implementation were considered in the assessment.

The thermodynamic assessment on the synthesis of UB_2 through the borocarbothermic reduction of UO_2 was featured in a publication by Turner *et al.* [34].
The chapter contains the results of the experiments in the synthesis of the known borides of uranium (UB_2 UB_4, and UB_{12}) through the borocarbothermic reduction of UO_2.

4.1. Thermodynamic modelling: synthesis of uranium borides by the borocarbothermic reduction of UO_2

As seen in Section 2.2, like other metal diborides, UB_2 may be prepared from the borocarbothermic reduction of the corresponding metal oxide.

$$2\ UO_{2\,(s)} + B_4C_{\,(s)} + 3\ C_{\,(s)} \rightarrow 2\ UB_{2\,(s)} + 4\ CO_{\,(g)} \qquad 4.1$$

The Gibbs free energy of reaction 4.1 and any related sub-reactions depends on temperature T and on the partial pressure of carbon monoxide p_{CO} in the reaction headspace. Using chemical thermodynamics (see Section 3.1) it was possible to plot the composition landscape of a reaction mixture intended for reaction 4.1 as a function of T and p_{CO} (Figure 4.1 – arrows only serve as a guide to the eye).

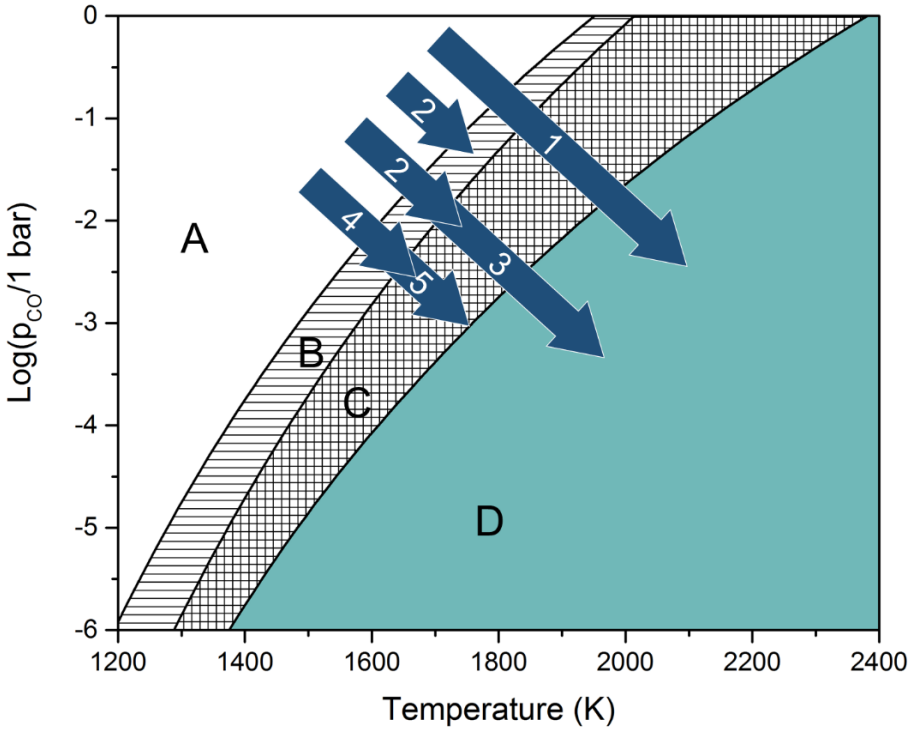

Figure 4.1: Predominance diagram of the thermodynamically stable condensed phases in a stoichiometric reaction mixture intended for the borocarbothermic synthesis of UB_2.

Starting from a reaction mixture containing UO_2, B_4C, and C (Figure 4.1, zone A), as T is increased and p_{CO} is lowered, UB_4 is first produced according to reaction 4.2 (Figure 4.1, zones B and C) and subsequently reacts with the remainder of the reaction mixture according to reaction 4.3 to afford UB_2 (Figure 4.1, zone D).

$$UO_{2\,(s)} + B_4C_{\,(s)} + C_{\,(s)} \rightarrow UB_{4\,(s)} + 2\,CO_{\,(g)} \qquad 4.2$$

$$UB_{4\,(s)} + UO_{2\,(s)} + 2\,C_{\,(s)} \rightarrow 2\,UB_{2\,(s)} + 2\,CO_{\,(g)} \qquad 4.3$$

It has been reported that an excess of boron carbide improved the purity of the resulting product in both the synthesis of UB_2 and UB_4 [101,127], suggesting that evaporation of volatile boron compounds occurs. Such a behaviour is common to the synthesis of borides and is usually ascribed to volatile boron oxides [132]. To justify their presence in the reaction system, reaction 4.2 was thought to be split in the following reactions:

$$7\ UO_{2\ (s)} + 8\ B_4C_{\ (s)} \rightarrow 7\ UB_{4\ (s)} + 2\ B_2O_{3\ (l,g)} + 8\ CO_{\ (g)} \quad 4.4$$

$$2\ B_2O_{3\ (l)} + 7\ C_{\ (s)} \rightarrow B_4C_{\ (s)} + 6\ CO_{\ (g)} \quad 4.5$$

Once reaction 4.4 becomes favourable (Figure 4.1, zone C), it kinetically competes with reaction 4.2 and produces B_2O_3 which may be lost to evaporation instead of taking part in reaction 4.5.

Alternatively, reaction 4.4 may be a necessary step in reaction 4.2, which may appear artificially more favourable than its sub-reactions by being considered as the combination of two individually favourable elementary steps. In fact, free transfer of free energy among different elementary processes is not always (if seldom) allowed and their lumping may lead to inaccurate predictions.

The thermodynamic model predicts reaction 4.5 to be always favourable in the conditions in which reaction 4.4 can occur; any B_4C that forms will then react again according to reactions 4.2 and 4.4. The work of Turner *et al.* demonstrated the feasibility of reaction 4.1, producing UB_2 with a purity of 90-92% [34]. The work of Guo *et al.* [101] demonstrated the feasibility of reaction 4.2 by using it to prepare UB_4, while Larroque *et al.* used reaction 4.4 and its analogues to prepare UB_4, NpB_4, and PuB_4 [133]. Reaction 4.5 represents the main method for producing B_4C on an industrial scale [134].

In this work, reaction 4.1 is further optimised, reaction 4.4 is replicated, and reaction 4.3 is explored in detail for the first time.

4.2. Thermodynamic modelling: synthesis of uranium borides by the direct conversion of uranium fluorides

Preparing UB_2 directly from uranium hexafluoride (UF_6) would be considerably attractive from the standpoint of commercial process simplification, as it would allow to avoid the production of UO_2 as an intermediary. A few reactions are considered below to assess the feasibility of using as a feedstock uranium hexafluoride or uranium tetrafluoride (UF_4), which can be readily obtained from UF_6 through reduction with hydrogen in reaction 4.6:

$$UF_{6\,(g)} + H_{2\,(g)} \rightarrow UF_{4\,(s)} + 2\,HF_{\,(g)} \quad 4.6$$

Reaction 4.6 is typically conducted at a temperature of 1500-2000 K, achieved by the concurrent injection of H_2 and F_2 in the reaction environment, which combust exothermically in reaction 4.7 [135]:

$$H_{2\,(g)} + F_{2\,(g)} \rightarrow 2\,HF_{\,(s)} \quad 4.7$$

Three sources of boron were considered in the following assessment: boron trifluoride (BF_3), elemental boron (B), and diborane (B_2H_6), with the respective reactions outlined below:

$$UF_{4\,(s)} + 2\,BF_{3\,(g)} + 5\,M_{\,(s)} \rightarrow UB_{2\,(s)} + 5\,MF_{2\,(s)} \quad 4.8$$

$$UF_{6\,(g)} + 2\,BF_{3\,(g)} + 6\,H_{2\,(s)} \rightarrow UB_{2\,(s)} + 12\,HF_{\,(g)} \quad 4.9$$

$$UF_{6\,(g)} + 4\,B_{\,(s)} \rightarrow UB_{2\,(s)} + 2\,BF_{3\,(g)} \quad 4.10$$

$$UF_{6\,(g)} + 2\,B_2H_{6\,(g)} \rightarrow UB_{2\,(s)} + 6\,HF_{\,(g)} \quad 4.11$$

Some relevant properties of the reactants are noted in Table 4.1, namely their melting and boiling points, their IDLH (Immediately Dangerous to Life and Health) thresholds, and any other notable hazards.

The assessment for reactions 4.9, 4.10, and 4.11 was oriented towards reactions occurring in a fluidised bed reactor (FBR) with the reactants in either gaseous form or as finely divided solids, in conditions comparable to the current, well-established Integrated Dry Route (IDR) process used to convert UF_6 into UO_2 [136]. This was done to maximise the transferability of technology between the two processes.

Table 4.1: Relevant properties of some proposed reactants for the conversion of UF_6 into UB_2

Substance	Melting point	Boiling point	IDLH toxicity threshold	Other hazards
B	2360 K [137]	> 3930 K [138]	592 mg/m^3 of B in B_2O_3 [139]	Explosive as a fine powder [140]
BF_3	146.5 K [141]	173.2 K [141]	70 mg/m^3 [141]	Corrosive, reacts with water [141]
B_2H_6	108.5 K [142]	180.3 K [142]	17 mg/m^3 [142]	Explosive, reacts with water [142]
UF_6	337.2 K at 152 kPa (triple point) [143]	329.6 K (sublimes) [143]	15 mg/m^3 [144]	Corrosive, radioactive, reacts with water [143]

In the IDR process, UF_6 is reacted in two stages with dry steam and with hydrogen to produce UO_2 powder through reactions 4.12 and 4.13, conducted respectively at 673 K and 973 K [136]:

$$UF_{6\,(g)} + 2\ H_2O_{\,(g)} \rightarrow UO_2F_{2\,(s)} + 4\ HF_{\,(g)} \qquad 4.12$$

$$UO_2F_{2\,(s)} + H_{2\,(s)} \rightarrow UO_{2\,(s)} + 2\ HF_{\,(g)} \qquad 4.13$$

The equilibrium constants for reactions 4.9, 4.10, and 4.11 were assessed at a temperature of 1000 K, as this temperature could be considered representative of the capabilities of existing plants processing UF_6 and its derivatives. The upper bound of the IDR route temperature was chosen as a best-case assumption, as the equilibrium constants of the examined reactions increases with temperature.

4.2.1. Metallothermic reduction of solid UF_4 and BF_3

In reaction 4.8, metals may be used as reductants for UF_4 and BF_3, in a partially condensed phase reaction. However, while the reaction is very thermodynamically favourable, its practical application presents several potential problems.

In analogy to the preparation of uranium metal from UF_4, Mg or Ca may be used as M in reaction 4.8 [145]. In the preparation of uranium metal the less-dense, light-metal fluorides MgF_2 and CaF_2 would form a slag floating on top of liquid uranium metal, enabling the facile separation of the two and the recovery of pure uranium metal [145].

In the case of the synthesis of UB_2, instead, the intended product would not be liquid and would have to be separated from the fluorides in a later step. Moreover, with BF_3 being gaseous, it would have to be blown through the reaction zone with an external apparatus or be included in the desired amount in a sealed pressure vessel from the outset.

Furthermore, the metallothermic reduction as written above may not be representative of the process and of its kinetic limitations: most likely, elemental U and B would be produced separately from the metallothermic reduction of UF_4 and BF_3 and would then have to combine from molten uranium and very fine powders of boron. This process would therefore have similar disadvantages in terms of final homogeneity as reactive melting of elemental U and B.

4.2.2. Hydrogen reduction of gaseous UF_6 and BF_3

In Reaction 4.9, gaseous hydrogen (H_2) was chosen as a reductant for its convenience, since it is relatively inexpensive, leaves no solid impurities in the final product and allows for a homogeneous gaseous reaction, thus improving mixing and reaction kinetics. However, the reaction is extremely unfavourable from the thermodynamic standpoint. The reaction has an equilibrium constant of $3.8 \cdot 10^{-28}$ at 1000 K (increasing with temperature), meaning that only a very low conversion per pass may be achieved in a chemical reactor [146] unless the concentration of HF is kept to extremely low levels in the reaction environment.

Furthermore, HF may react with newly formed UB_2 through a very favourable reaction occurring with an even lower HF:UB_2 ratio (6:1 as opposed to 12:1 for the reverse of reaction 4.9) and an equilibrium constant of $7.8 \cdot 10^{16}$ at 1000 K:

$$UB_{2\,(s)} + 6\,HF_{\,(g)} \rightarrow U_{(s)} + 2\,BF_{3\,(g)} + 3\,H_{2\,(g)} \qquad 4.14$$

The concentration of HF may be kept low enough for the reaction to proceed and for its product not to be immediately consumed in reaction 4.14 by adding scavengers for HF such as finely dispersed Mg or Ca, which would form remarkably stable fluorides.

$$M_{(s)}\ 2\ HF_{(g)} \rightarrow 2\ MF_{2\ (s)} + H_{2\ (g)} \qquad 4.15$$

Where M in reaction 4.15 can be Mg or Ca. The equilibrium constants for reaction 4.15 with Mg and Ca at 1000 K are, respectively, $3.5 \cdot 10^{20}$ and $1.3 \cdot 10^{26}$, as a testament to their effectiveness as scavengers for HF.

In the extreme case where all of the produced HF is captured by the scavengers, the overall process described by reaction 4.16 becomes very similar to the direct metallothermic reduction of reaction 4.8:

$$UF_{6\ (s)} + 2\ BF_{3\ (g)} + 6\ M_{\ (s)} \rightarrow UB_{2\ (s)} + 6\ MF_{2\ (s)} \qquad 4.16$$

Where M can be Mg or Ca. The equilibrium constants for reaction 4.16 with Mg and Ca at 1000 K are, respectively, $7.5 \cdot 10^{95}$ and $1.5 \cdot 10^{129}$.

However, as in the case of reaction 4.8, the metallothermic reduction as written above would not be representative of the process and of its kinetic limitations: most likely, elemental U and B would be produced separately from the metallothermic reduction of UF_6 and BF_3 and would then have to combine from very fine powders (or liquid droplets, depending on the process temperature) suspended in the gaseous phase to form UB_2.

Moreover, the presence of HF scavengers would come with several disadvantages: not only this solution would add costs and complexity to the process, but the finely divided metals may also form explosive mixtures [147]; finally, they would also compete with uranium in the formation of borides (with Mg being able to form diborides [94] and Ca being able to form a hexaboride [148]) and they would also represent a source of solid impurities in the final product – thus negating one of the main advantages of the route.

4.2.3. Direct borothermic reduction of UF_6 with elemental boron

In reaction 4.10, elemental boron is used directly both as a reductant and as a source of boron. The reaction is highly favourable, with an equilibrium constant of $8.7 \cdot 10^{22}$ at 1000 K, but boron would have to be introduced as a finely divided solid. This may not only hinder the kinetics of the process when compared to a purely gaseous, monophasic process, but it may also render stoichiometry control more difficult. In fact, if deposition of UB_2 occurs on the solid boron particles, the locally boron-rich environment may lead to thermodynamically favourable reactions such as reaction 4.17:

$$UB_{2\,(s)} + 2\,B_{\,(s)} \rightarrow UB_{4\,(s)} \qquad 4.17$$

Leading to UB_4 being formed instead of UB_2. Furthermore, elemental boron is relatively expensive and part of it would be lost as BF_3. While BF_3 may be recycled to reobtain elemental boron (e.g. by hydrolysis to B_2O_3 and subsequent reduction to B via electrolysis, or by direct reduction of BF_3 [149]), the complexity of the coupled process would likely negate any advantages coming from the elimination of the UO_2 conversion steps.

4.2.4. Reduction of UF_6 with B_2H_6

Reaction 4.11 is very favourable from a thermodynamic standpoint, with an equilibrium constant of $6.4 \cdot 10^{9}$ at 1000 K, but diborane is highly toxic and chemically reactive, requiring special precautions for its handling. In particular, it will spontaneously ignite in air [142], with the potential to enlarge any leaks from the vessels that contain it and to cause cascading failures. Diborane is usually stored as a liquid at temperatures lower than -20 °C, with higher temperatures causing its decomposition into hydrogen and higher borides such as pentaborane, with a higher toxicity [150]. Storage tanks and transfer pipes must also be always kept at a positive pressure, in order to avoid ingress of air and moisture from the environment [150]. Diborane is compatible with polytetrafluoroethylene and with nickel alloys such as Monel [150], thus making it compatible with equipment used for the handling of UF_6 [151].

While the use of diborane may be warranted if the process were found to be extremely convenient, two significant limitations are readily apparent:

- The first one is related to the production of HF, which may react again with UB_2 via reaction 4.14 and the reverse of reaction 4.9, as seen above.
- The second disadvantage is the possibility of further boridation of the produced UB_2 via reaction 4.18, in analogy to reaction 4.17:

$$UB_{2\,(s)} + 2\,B_2H_{6\,(g)} \rightarrow UB_{4\,(s)} + 3\,H_{2\,(g)} \qquad 4.18$$

Reaction 4.18 has an equilibrium constant of $9.7 \cdot 10^{15}$ at 1000 K, making it a formidable competing reaction in the preparation of UB_2 via this process.

4.2.5. Remarks on the direct conversion of uranium fluorides into uranium borides

The readily apparent chemical challenges presented by the reaction pathways starting directly from uranium fluorides, compounded by the technical precautions required for their handling, discouraged further research on the topic for this work, and focus remained on the relatively controllable and convenient conversion of uranium dioxide to uranium diboride presented in Section 4.1.

4.3. Experiments in the borocarbothermic synthesis of uranium borides from UO_2

As seen in Figure 4.1, the partial pressure of CO is a key parameter in defining the thermodynamically preferred products. In the synthesis work, the overhead partial pressure of CO was controlled by changing the method by which gaseous products are removed. For synthesis work carried out in the alumina tube furnace under flowing argon, early attempts to conduct reaction 1 at 1750 °C yielded a mixture of UB_4, UBC, and UO_2 instead of UB_2. Based on Figure 4.1, the partial pressure of CO in synthesis conditions was estimated to be greater than 0.03 bar.

As a result of these initial findings, synthesis work under lower CO partial pressures was carried out within the tungsten-lined furnace under actively pumped vacuum. During all runs, the vacuum gauge of the furnace consistently indicated a value of 0 mbar. Based on the ultimate vacuum that the pump could provide and on the division of the pressure gauge, the pressure of CO in the synthesis conditions was estimated to lie between $6 \cdot 10^{-5}$ and $5 \cdot 10^{-4}$ bar (see Section 3.4.4.2).

It was not possible to track consistently and reliably the mass change of the pellets before and after firing, as the mechanical stability of the yet-unfired pellets of reactants was often poor and led to fragmentation, chipping, and fretting.

4.3.1. Synthesis of UO_2-UB_4 mixtures at relatively high partial pressures of CO

B_4C, C and UO_2. powders were mixed together in stoichiometric amounts according to reaction 4.1. The powder was not pelletised for this experiment. The powder mixture was then fired in the tube furnace (1750 °C, 1 hour dwell) under a flow of 20 L/h of argon at near-atmospheric pressure. The product was a mixture of steel-grey and brick-red solids, as shown in Figure 4.2.
Phase analysis of the diffraction patterns, shown in Figure 4.3 allowed to identify crystalline UB_4 ($P4/mbm$, a = 7.0578 Å, c = 3.9008 Å) and UBC ($Cmcm$, a = 3.5915 Å, b = 11.9962 Å, c = 3.3458 Å) in the grey solid, while crystalline UO_{2+x} ($Fm\bar{3}m$, a = 5.4701 Å) appeared as the only crystalline phase in the red material.

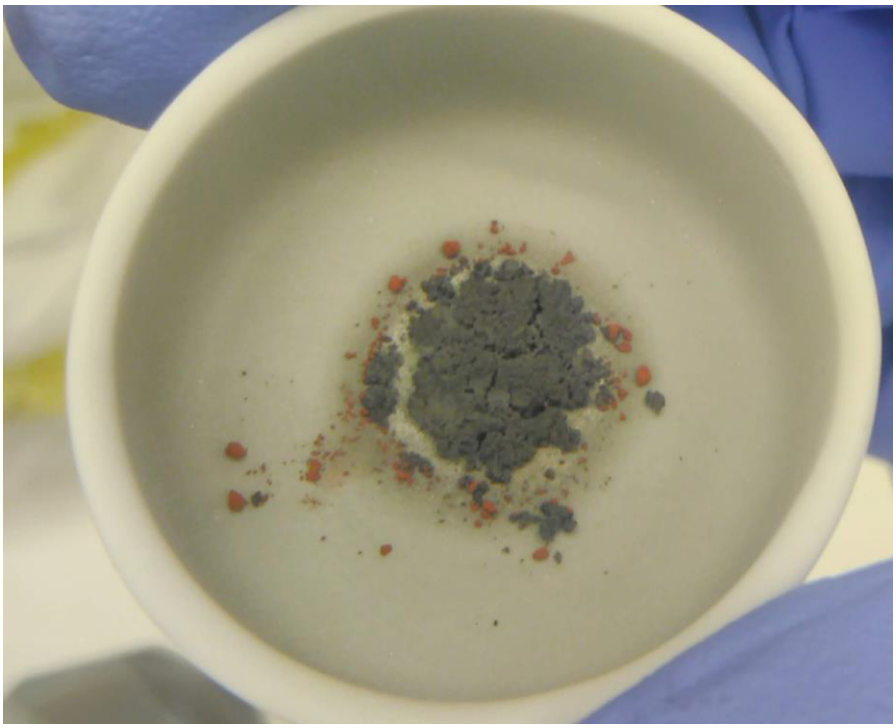

Figure 4.2: Mixture of UB_4 and UO_2, obtained after firing a reaction mixture intended for UB_2 in the tube furnace

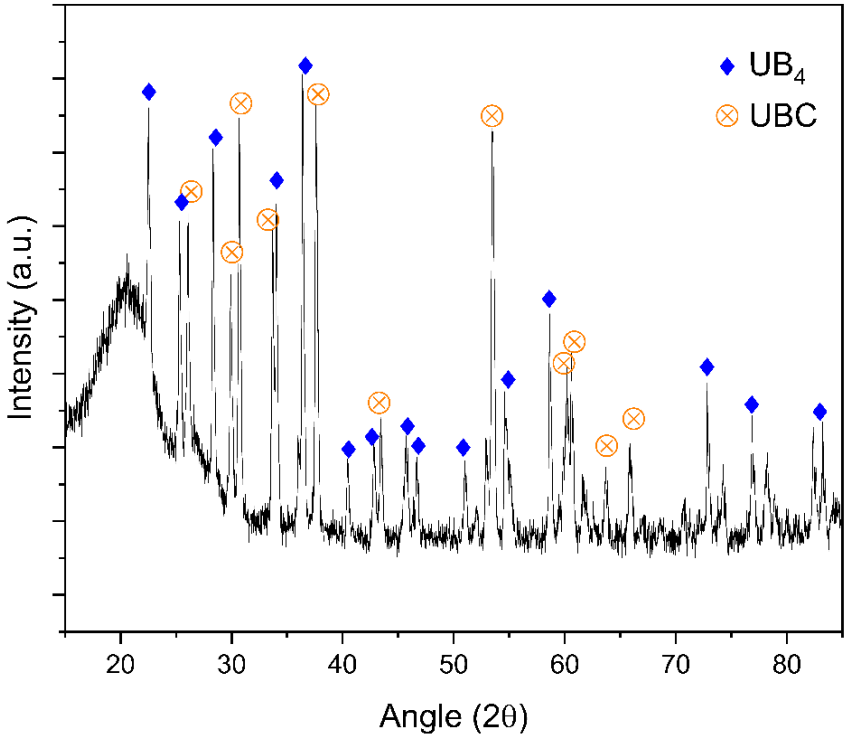

Figure 4.3: XRD pattern of the grey solid recovered from the UB_2 synthesis attempt in the tube furnace

4.3.2. Synthesis of UB_2 at relatively low partial pressures of CO

Over multiple runs, B_4C, C and UO_2. powders were mixed together in the amounts outlined in Table 4.2 and formed into a pellets using the method described in Section 3.4. The pellets were then fired in the chamber furnace under actively pumped vacuum. The temperature and the time at temperature were 1750 °C and 1 hour respectively for experiments A, B, and C, and 1400 °C and 4 hours for experiment D.

The diffraction patterns for synthesis A, B, C, and D are reported in Figure 4.4, Figure 4.5, and Figure 4.6, respectively.

The composition values reported in Table 4.2 are derived from XRD phase analysis, performed as described in Section 3.4.5. Only the abundances of uranium-bearing phases are considered and compared, in order to minimise the errors associated with the comparison of phases with widely varying X-ray extinction coefficients.

The product was a dark grey solid for experiments A-C (Figure 4.8) and a reddish-grey solid for experiment D (Figure 4.9). The dark discoloration at the bottom of the crucible in Figure 4.8 is associated with the original UB_2-Mo interaction product described in Section 3.4.4, which became lighter as the crucible was used in repeated synthesis, as shown in Figure 4.9. It is likely that this is due to diffusion of Mo across the interaction product.

Table 4.2: Composition of the reaction mixture for UB_2 and firing conditions over experiments A, B, C, and D.

ID	UO_2 (eq.)	B_4C (eq.)	C (eq.)	Conditions	Purity	Impurities
A	2.00	1.05	3.00	1750 °C, 1 h	94%	UB_4 (2%), UBC (2%), UC (2%)
B	2.00	1.04	2.85	1750 °C, 1 h	94%	UO_2 (3%), $UMoB_4$ (2%), UB_4 (1%)
C	2.00	1.05	2.85	1750 °C, 1 h	95%	UB_4 (2%), UBC (2%), UO_2 (1%)
D	2.00	1.05	3.00	1400 °C, 4 h	29%	UO_2 (31%), UB_4 (30%), UBC (7%), C*

* Quantification of C content was not deemed reliable due to the difference in X-ray extinction coefficient with the other phases

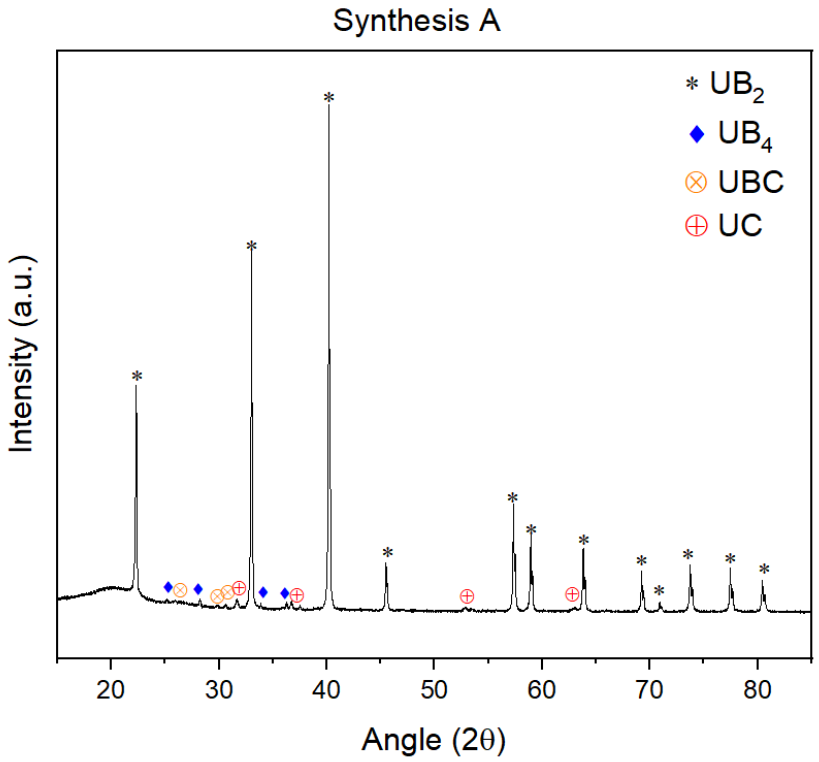

Figure 4.4: XRD pattern of the products of synthesis A.

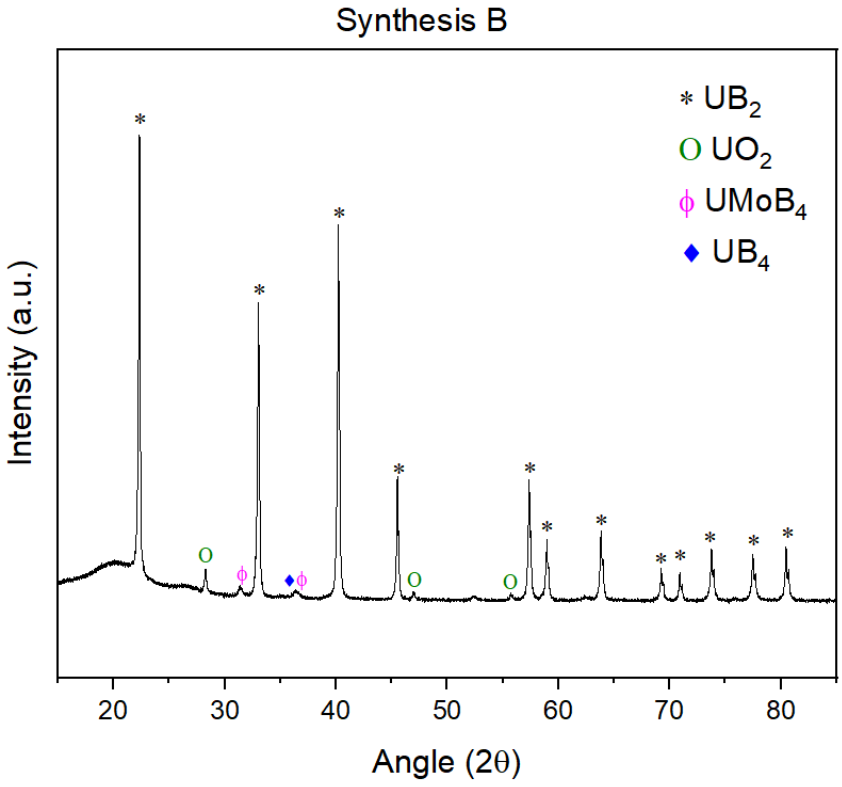

Figure 4.5: XRD pattern of the products of synthesis B.

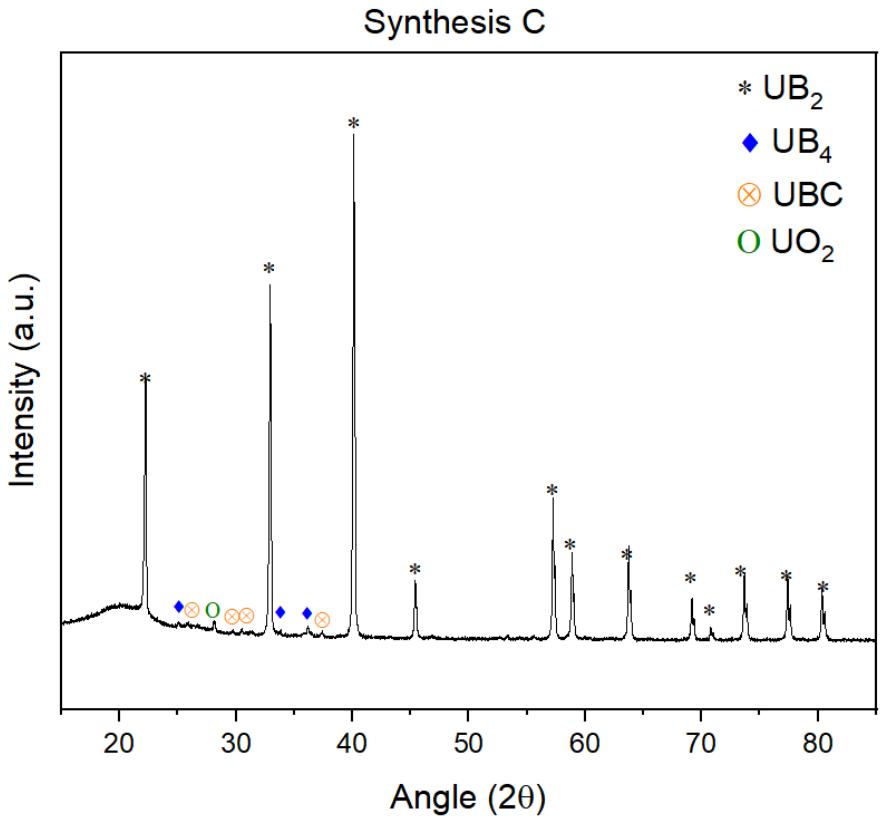

Figure 4.6: XRD pattern of the products of synthesis C

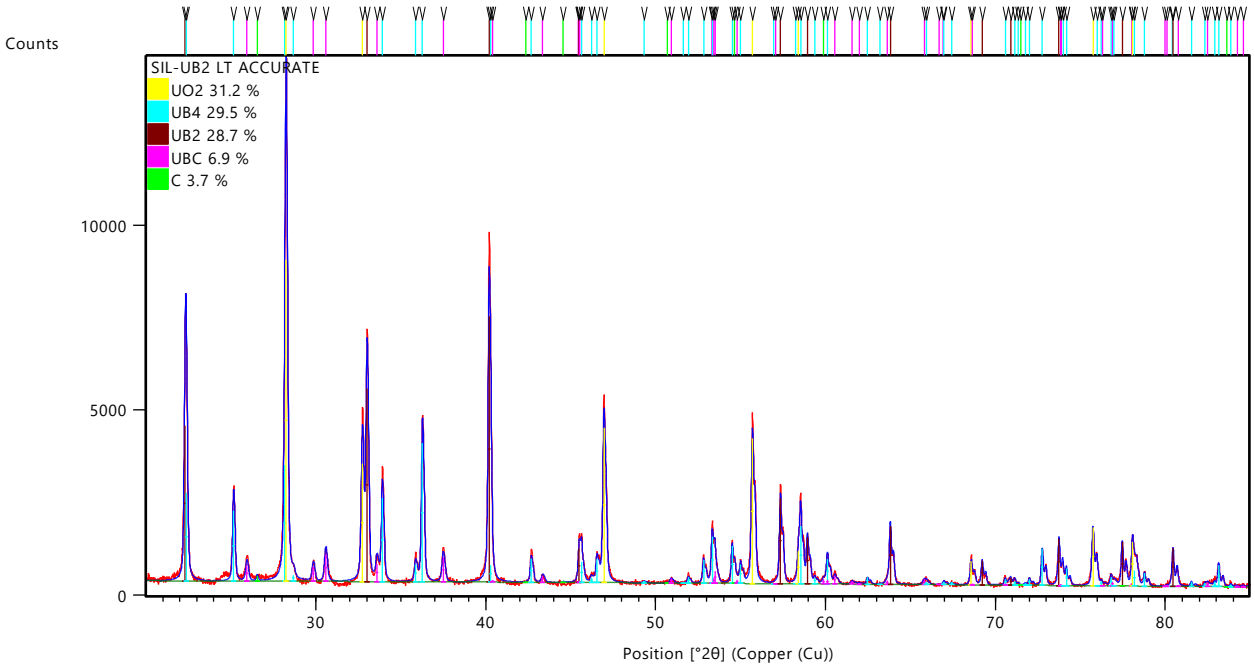

Figure 4.7: XRD pattern of the products of synthesis D

Figure 4.8: Typical sample of UB_2 with high purity.

Figure 4.9: Typical sample of UB_2 with impurities of UO_2.

Taking into account the role of boron carbide as a reductant via reaction 4.4 is crucial in minimising the residual carbon content, as indicated by the UC ($Fm\bar{3}m$, a = 4.9610 Å) and UBC ($Cmcm$, a = 3.5918 Å, b = 11.9959 Å, c = 3.3456 Å) impurities that were detected by XRD the final product. If the C content of the reaction mixture is not reduced accordingly when adding an excess of B_4C, the residual C will be able to displace B from UB_2, forming UB_4, UBC, and UC through reactions 4.19 and 4.20:

$$2\ UB_{2\ (s)} + C_{\ (s)} \rightarrow UB_{4\ (s)} + UC_{\ (s)} \qquad 4.19$$

$$3\ UB_{2\ (s)} + 2\ C_{\ (s)} \rightarrow UB_{4\ (s)} + 2\ UBC_{\ (s)} \qquad 4.20$$

The high purity of 93-95% achieved over multiple runs is an improvement over the first results of Turner *et al.* [127], who reported a purity of 90%, and a testament to the robustness and reproducibility of the method.

While it did not afford a high-purity product, synthesis D demonstrated the feasibility of the low-temperature production of UB_2 and contributed to the validation of the thermodynamic model in a point far closer to the limit of UB_2 formation than that sampled by attempts A through C (see Figure 4.1). However, no further attempts were made due to time constraints.

4.3.3. Synthesis of UB_4 by reaction of UO_2 with B_4C

B_4C and UO_2. powders were mixed together in stoichiometric amounts according to reaction 4.4 and formed into a pellet using the method described in Section 3.4. The pellet was then fired in the tube furnace (1750 °C, 1 hour dwell) under a flow of argon at near-atmospheric pressure.

The product was a steel-grey solid (shown in Figure 4.10). Crystalline UB_4 (98 wt%, $P4/mbm$, a = 7.0577 Å, c = 3.9010 Å) and UO_2 (2 wt%, $Fm\bar{3}m$, a = 5.4702 Å) were identified in the product via XRD (Figure 2a).

The incomplete reaction may be ascribed to the formation of volatile B_2O_2, which may form from reaction 4.21 competing with reaction 4.4 or from the reduction of B_2O_3 by B_4C [152], as described by reaction 4.22:

$$5\ UO_{2\,(s)} + 6\ B_4C_{\,(s)} \rightarrow 5\ UB_{4\,(s)} + B_2O_{2\,(g)} + 6\ CO_{\,(g)} \qquad 4.21$$

$$B_4C_{\,(s)} + 5\ B_2O_{3\,(l)} \rightarrow 7\ B_2O_{2\,(g)} + CO_{\,(g)} \qquad 4.22$$

Both processes result in a decreased effectiveness of B_4C as a reductant. In fact, reaction 4.21 requires 5% more B_4C than reaction 4.4 to completely convert a given amount of UO_2, with the former having a stoichiometric ratio of B_4C to UO_2 of 6:5 and the latter of 8:7.

4.3.4. Synthesis of UB_2 from the comproportionation of UO_2 and UB_4

UB_4 (as prepared in Section 4.3.3), UO_2, and C were mixed together in stoichiometric amounts according to reaction 4.3 and formed into a pellet using the method described in Section 3.4. A picture of the yet-unmixed reactants is shown in Figure 4.10, with UB_4 being the grey solid on the left and UO_2 being the reddish solid on the right.

The residual UO_2 content of the prepared UB_4 was kept into account and considered for the purposes of stoichiometry.

Figure 4.10: UB_4 (left, grey) and UO_2 (right, brick red) in the jar of the ball mill prior to mixing

The pellet was then fired in the chamber furnace (1750 °C, 1 hour dwell) under actively pumped vacuum. The product was a grey solid with a reddish tinge, similar to that shown in Figure 4.9. Crystalline UB_2 (82 wt%, $P6/mmm$, a = 3.1301 Å, c = 3.9869 Å), UO_{2+x} (16 wt%, $Fm\bar{3}m$, a = 5.4698 Å) and $MoUB_4$ (2 wt%, $Pbam$, a = 7.3010 Å, b = 9.4151 Å, c = 3.6487 Å) were identified in the product via phase analysis of the diffraction pattern (Fig 4.11b), the latter being likely formed by reactions with the bottom of the crucible.

The overall boron-to-uranium ratio in the crystalline phases is 1.72:1, or 86% of the initial 2:1 ratio. The more pronounced boron deficiency in the crystalline phases when compared to the UB_4 sample may be due to more intense boron evaporation under vacuum or to interactions with the bottom of the crucible.

The crystalline phases of the UB_2 sample appear to be carbon-deficient as well, as indicated by the excess of UO_2 that was left among the products. Not unlike boron, carbon may be present in undetected amorphous phases or may have been subtracted from the reaction environment by interactions with the bottom of the crucible, potentially limiting the extent of the reaction.

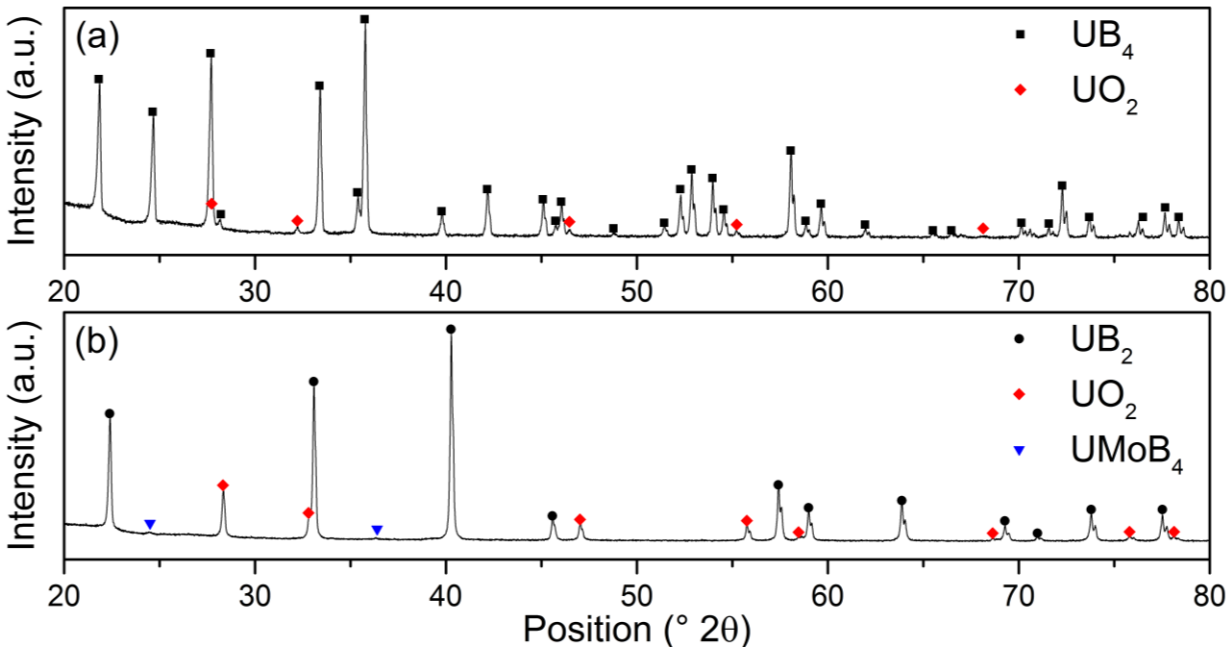

Fig 4.11: XRD patterns of the products of the synthesis of UB_4 from UO_2 and B_4C (a) and of the synthesis of UB_2 from UO_2, B_4C, and C (b).

4.3.5. Synthesis of UB_{12}

Uranium dodecaboride (UB_{12}) was prepared through the borocarbothermic synthesis route, aptly modified with the addition of diboron trioxide (B_2O_3) according to reaction 4.23, as B_4C alone would not be able to deliver boron to UO_2 above a B:U ratio of 8:1 without leaving solid carbon residues (as exemplified by reaction 4.24):

$$7\ UO_{2\,(s)} + 20\ B_4C_{\,(s)} + 2\ B_2O_{3\,(s,l)} \rightarrow 7\ UB_{12\,(s)} + 20\ CO_{\,(g)} \qquad 4.23$$

$$UO_{2\,(s)} + 3\ B_4C_{\,(s)} \rightarrow UB_{12\,(s)} + C_{\,(s)} + 2\ CO_{\,(g)} \qquad 4.24$$

UO_2, B_4C, and B_2O_3 were mixed together in stoichiometric amounts according to reaction 4.23, and formed into a pellet using the method described in Section 3.4.

The pellet was fired at 1750 °C for 1 h under actively pumped vacuum in the chamber furnace in a molybdenum crucible. However, due to time constraints, the crucible was shared with a pellet of a reaction mixture intended for the synthesis of UB_2, with an overall U:B ratio of the contents of the crucible roughly 4.7 times greater than the one intended for UB_{12}.

Despite the pellets being approximately 1 cm apart in the crucible, diffusion of boron must have been fast enough at the reaction temperature for the two pellets to chemically equilibrate almost completely. In fact, according to the thermodynamic model, the comproportionation of UB_2 and UB_{12} into UB_4 through reaction 4.25 is expected to be favourable at all temperatures:

$$4\ UB_{2\,(s)} + UB_{12\,(s)} \rightarrow 5\ UB_{4\,(s)} \qquad 4.25$$

However, despite the UB_2 pellet containing more than enough uranium to fully convert UB_{12}, the reaction did not occur to completion and some UB_{12} was left in the pellet to be detected by XRD, as shown in Figure 4.12.

The composition of the products, as determined by phase analysis, was 8 wt% UB_{12} ($Fm\bar{3}m$, a = 7.4752 Å), 78 wt% UB_4 ($P4/mbm$, a = 7.0577 Å, c = 3.9010 Å), and 14 wt% UB_2 ($P6/mmm$, a = 3.1302 Å, c = 3.9858 Å).

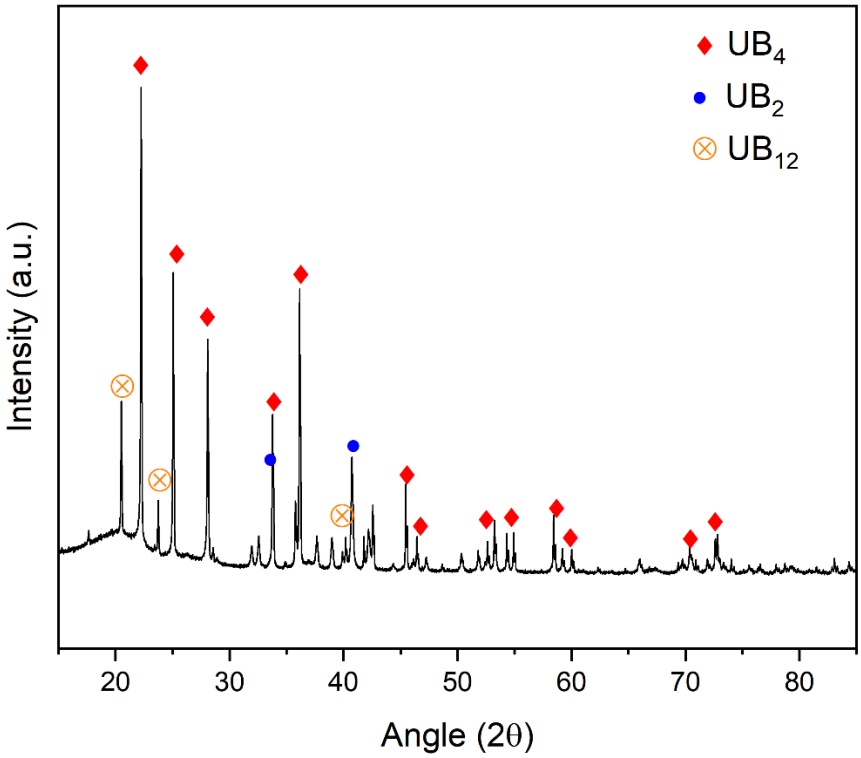

Figure 4.12: XRD pattern of the products of the UB_{12} synthesis attempt

5. Modelling and experiments on the synthesis of tungsten borides

The phase diagram of the W-B system (shown in Figure 5.1, as reported by Duschanek *et al.* [153]) shows three congruently-melting tungsten borides: W_2B, WB, and W_2B_5, the crystallographic properties of which are listed in Table 5.1. However, there are technical limitations in its construction: the weak X-ray scattering of boron compared with tungsten only allows for precise crystallographic determination of the position of W atoms in the crystal lattice via XRD, while its strong neutron absorption limits the effectiveness of neutron diffraction [154], although precise measurements have been performed on WB prepared with ^{11}B [155]. Furthermore, the high temperatures involved add considerable uncertainty due to the potential volatilisation of boron and contamination from crucible materials. The tungsten boride for which non-stoichiometry is reported most often is W_2B_5, in the form of a defective boron sublattice resulting in the W_2B_{5-x} notation [156].

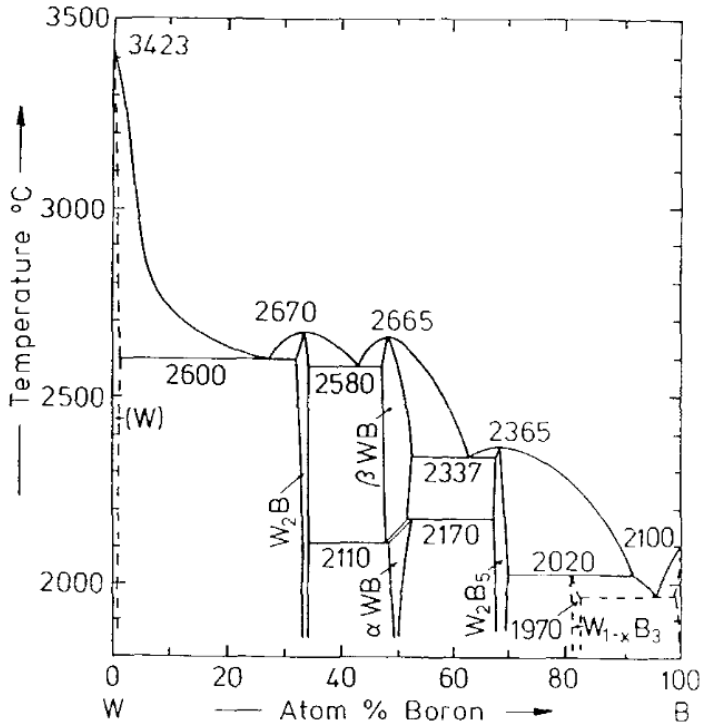

Figure 5.1: Phase diagram of the W-B system

Table 5.1: Crystallographic properties of W_2B, WB, and W_2B_5.

Substance	Space group	*a*	*b*	*c*	α	β	γ	Source
W_2B	$P6/mmm$	5.57 Å	5.57 Å	4.74 Å	90°	90°	90°	[157]
WB	$I4_1/amd$	3.1060 Å	3.1060 Å	16.9513 Å	90°	90°	90°	[155]
W_2B_5	$P6_3/mmc$	2.921 Å	2.921 Å	17.293 Å	90°	90°	120°	[158]

Tungsten borides may find applications as potential shielding materials for compact fusion reactors owing to their combination of neutron-shielding and gamma-ray shielding properties, deriving respectively from their content of boron and tungsten, with W_2B_5 appearing especially promising in terms of effectiveness as a shielding material as predicted by Windsor *et al*. [159].

As for the case of uranium borides, the possibility of being manufactured on a large scale and at relatively low cost is critical for their success. In this chapter, a borocarbothermic synthesis pathway of three tungsten borides is presented, assessed through thermodynamic predictions (formulated with the methods described in Section 3.1), and used successfully to prepare three tungsten borides from tungsten oxides. Of the three borides that were obtained, two were prepared with crystallographic purities greater than 99% and the one with the highest purity, W_2B_5, is the one that is expected to have the most significant applications in shielding for fusion reactors [159].

The synthesis work presented in this chapter makes full use of the experience gained with the preparation of uranium borides and was performed while the chamber furnace was offline for a prolonged maintenance.

5.1. Thermodynamic modelling: synthesis of tungsten borides by the borocarbothermic reduction of tungsten oxides

Three tungsten borides have been prepared by reaction of tungsten nanopowders with boron carbide by Wang *et al.* [160], namely W_2B,, WB and W_2B_5. However, the reported process (which can be described by reaction 5.1, with x = 0.5, 1, and 2.5) leaves a carbon residue in the final product that

must be removed by reaction with molten calcium, as described in reaction 5.2 forming calcium carbide:

$$W_{(s)} + \frac{x}{4} B_4C_{(s)} \rightarrow WB_{x\,(s)} + \frac{x}{4} C_{(s)} \quad 5.1$$

$$2\,C_{(s)} + Ca_{(l)} \rightarrow CaC_{2\,(s)} \quad 5.2$$

Calcium carbide is then separated from the solid tungsten boride by leaching with an aqueous solution of hydrochloric acid, which hydrolyses calcium carbide to soluble calcium chloride ($CaCl_2$) and gaseous acetylene (C_2H_2), as described in reaction 5.3:

$$CaC_{2\,(s)} + 2\,H^+_{(aq)} + 2\,Cl^-_{(aq)} \rightarrow Ca^{2+}_{(aq)} + 2\,Cl^-_{(aq)} + C_2H_{2\,(g)} \quad 5.3$$

However, the boride W_2B_5 was shown to be affected by the decarburisation reaction with Ca, with molten Ca being able to strip boron from W_2B_5 to form CaB_6 and WB [160], as described in reaction 5.4:

$$2\,W_2B_{5\,(s)} + Ca_{(l)} \rightarrow 4\,WB_{(s)} + CaB_{6\,(s)} \quad 5.4$$

The borocarbothermic reduction of tungsten trioxide (WO_3) may afford a synthetic route to the same compounds requiring no subsequent purification, in that all carbon is ideally removed as carbon monoxide:

$$8\,WO_{3\,(s)} + B_4C_{(s)} + 23\,C_{(s)} \rightarrow 4\,W_2B_{(s)} + 24\,CO_{(g)} \quad 5.5$$

$$4\,WO_{3\,(s)} + B_4C_{(s)} + 11\,C_{(s)} \rightarrow 4\,WB_{(s)} + 12\,CO_{(g)} \quad 5.6$$

$$8\,WO_{3\,(s)} + 5\,B_4C_{(s)} + 19\,C_{(s)} \rightarrow 4\,W_2B_{5\,(s)} + 24\,CO_{(g)} \quad 5.7$$

Chemical thermodynamics were used to determine which conditions could be conducive to reactions 5.5, 5.6, and 5.7. Like in the case of the borocarbothermic reduction of UO_2, it is expected that the change in Gibbs free energy associated with the reactions depends on temperature and on

the partial pressure of CO in the overhead space. The process was assumed to entail the carbothermic reduction of WO_2 as a first step. This process was assessed separately in reaction 5.8:

$$WO_{3\,(s)} + C_{\,(s)} \rightarrow WO_{2\,(s)} + CO_{\,(g)} \qquad 5.8$$

With reactions 5.5, 5.6, and 5.7 becoming, respectively reactions 5.9, 5.10, and 5.11:

$$8\ WO_{2\,(s)} + B_4C_{\,(s)} + 15\ C_{\,(s)} \rightarrow 4\ W_2B_{\,(s)} + 16\ CO_{\,(g)} \qquad 5.9$$

$$4\ WO_{2\,(s)} + B_4C_{\,(s)} + 7\ C_{\,(s)} \rightarrow 4\ WB_{\,(s)} + 8\ CO_{\,(g)} \qquad 5.10$$

$$8\ WO_{2\,(s)} + 5\ B_4C_{\,(s)} + 11\ C_{\,(s)} \rightarrow 4\ W_2B_{5\,(s)} + 16\ CO_{\,(g)} \qquad 5.11$$

The equilibrium pressure of CO as a function of temperature was calculated for the reactions above and the results are plotted in Figure 5.2.

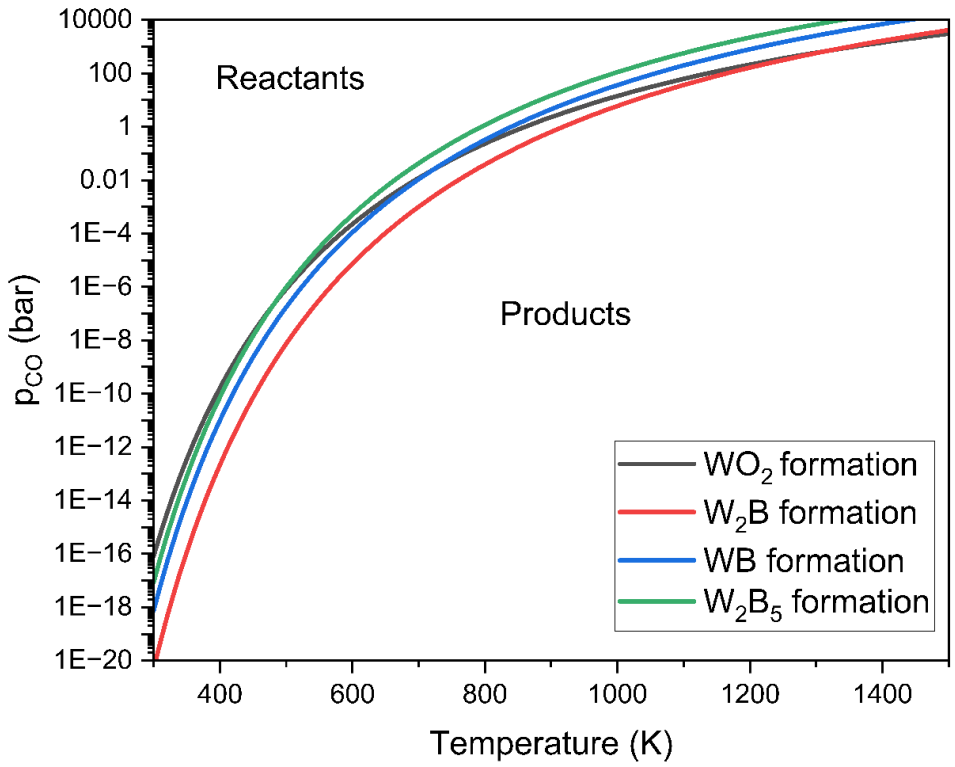

Figure 5.2: Equilibrium pressure of CO as a function of temperature for the carbothermic reduction of WO_3 to WO_2 and for the synthesis of W_2B, WB, and W_2B_5.

The equilibrium partial pressures of CO of reactions 5.8, 5.9, 5.10, and 5.11 are far higher than those involved in the U-B-C-O system (see Figure 4.1); the inert gas flow of the tube furnace was therefore deemed more than sufficient to drive the reaction forwards by removing the CO that is produced.

5.2. Experiments in the borocarbothermic synthesis of WB_x from WO_3

Stoichiometric amounts of WO_3, B_4C, and C, as defined by reactions 5.5, 5.6, and 5.7, were hand-ground together in an agate mortar with an agate pestle and compacted into pellets, as described in Section 3.4. The pellets were then fired at 1400 °C for 4 hours, with a ramp rate of 10 °C/min, under an Ar flow of 20 L/h.

The masses of the pellets were recorded before and after firing, in order to determine the extent of conversion.

5.2.1. Synthesis of W_2B

Phase analysis of the XRD pattern of the products, shown in Figure 5.3, indicates a relative majority of W_2B (61 wt%, $P6/mmm$, a = 5.5706 Å, c = 4.4710 Å) in the crystalline phases, accompanied with WB (24 wt%, $I4_1/amd$, a = 3.1059 Å, c = 16.9560 Å) and WC (15 wt%, $P\bar{6}m2$, a = 2.9020 Å, c = 2.8492 Å). The recovered pellet had a mass which was 70.3% the mass of the original pellet. Complete conversion to W_2B would be associated with a residual mass of 69.3%.

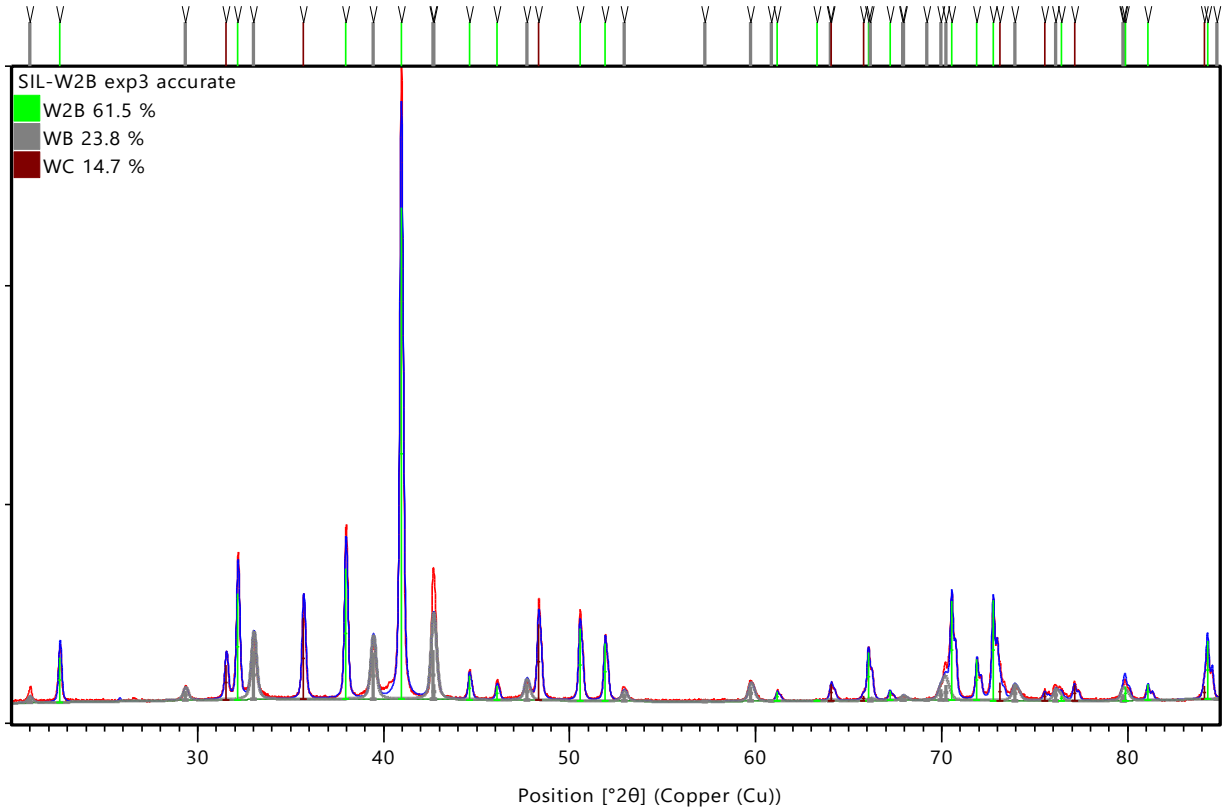

Figure 5.3: XRD pattern of the products of the synthesis of W_2B.

Considering the uncertainty in the XRD phase analysis, the measured ratio of WB to WC (4 : 2.5) would be compatible with the following stepwise behaviour in the production of W_2B, proceeding through reactions 5.12 and 5.13:

$$8\ WO_{3\,(s)} + B_4C_{\,(s)} + 23\ C_{\,(s)} \rightarrow 4\ WB_{\,(s)} + \frac{8}{3} WC_{\,(s)} + \frac{4}{3}\ WO_{2\,(s)} + \frac{64}{3} CO_{\,(g)} \quad 5.12$$

$$4\ WB_{\,(s)} + \frac{8}{3} WC_{\,(s)} + \frac{4}{3}\ WO_{2\,(s)} \rightarrow 4\ W_2B_{\,(s)} + \frac{8}{3} CO_{\,(g)} \quad 5.13$$

With reaction 5.12 affording a WB:WC ratio of 4 : 2.7. The absence of WO_2 among the detected crystalline phases could be due to its volatilisation. It must be noted that the WO_2 has been reported to not volatilise directly, but rather, to disproportionate to tungsten metal and to far more volatile WO_3 through reaction 5.14 [161].

$$3\ WO_{2\,(s)} \rightarrow W_{(s)} + 2\ WO_{3\,(g)} \quad 5.14$$

Furthermore, in the presence of Al_2O_3 (which was chosen as a crucible material) at high temperatures, W can be oxidised by alumina vapours to volatile WO_3, with the formation of gaseous aluminium (II) oxide Al_2O_2 [162].

$$3\ Al_2O_{3\,(g)} + W_{(s)} \rightarrow 3\ Al_2O_{2\,(g)} + WO_{3\,(g)} \quad 5.15$$

The volatilisation of WO_3 could also explain the ratio of WB to WC being lower than what could be expected through reaction 5.12.

5.2.2. Synthesis of WB

Phase analysis of the XRD pattern of the products, shown in Figure 5.4, shows a relative majority of WB (96.5 wt%, $I4_1/amd$, a = 3.1055 Å, c = 16.9555 Å) in the crystalline phases, accompanied with W_2B (2 wt%, $P6/mmm$, a = 5.5701 Å, c = 4.4702 Å), WC (1 wt%, $P\bar{6}m2$, a = 2.9022 Å, c = 2.8496 Å), and WO_2 (0.5 wt%, $P2_1/c$, a = 5.5768 Å, b = 4.8986 Å, c = 5.6645 Å). Due to breaking of the pellet, the mass change data of this experiment were not considered to be reliable.

Carbon, boron carbide, or other boron compounds may be present in undetected amorphous phases. It must be noted that, with B_4C being composed of light elements, its detection and quantification by XRD among substances containing notably heavier tungsten is remarkably difficult. Even if detected, their quantification would not be reliable for the large difference in their X-ray scattering and absorption characteristics when compared to tungsten-bearing phases.

The powders resulting from the synthesis experiment were re-compacted into a pellet and fired again at 1400 °C for two hours. The mass loss was recorded at 1.6%. Phase analysis of the XRD pattern of the re-fired powders, shown in Figure 5.5, indicated a final purity of WB of 99 wt%.

The residual content of W_2B was approximately 1 wt%, suggesting that WO_2, WC, and any undetectable boron-bearing phases reacted again to afford WB.

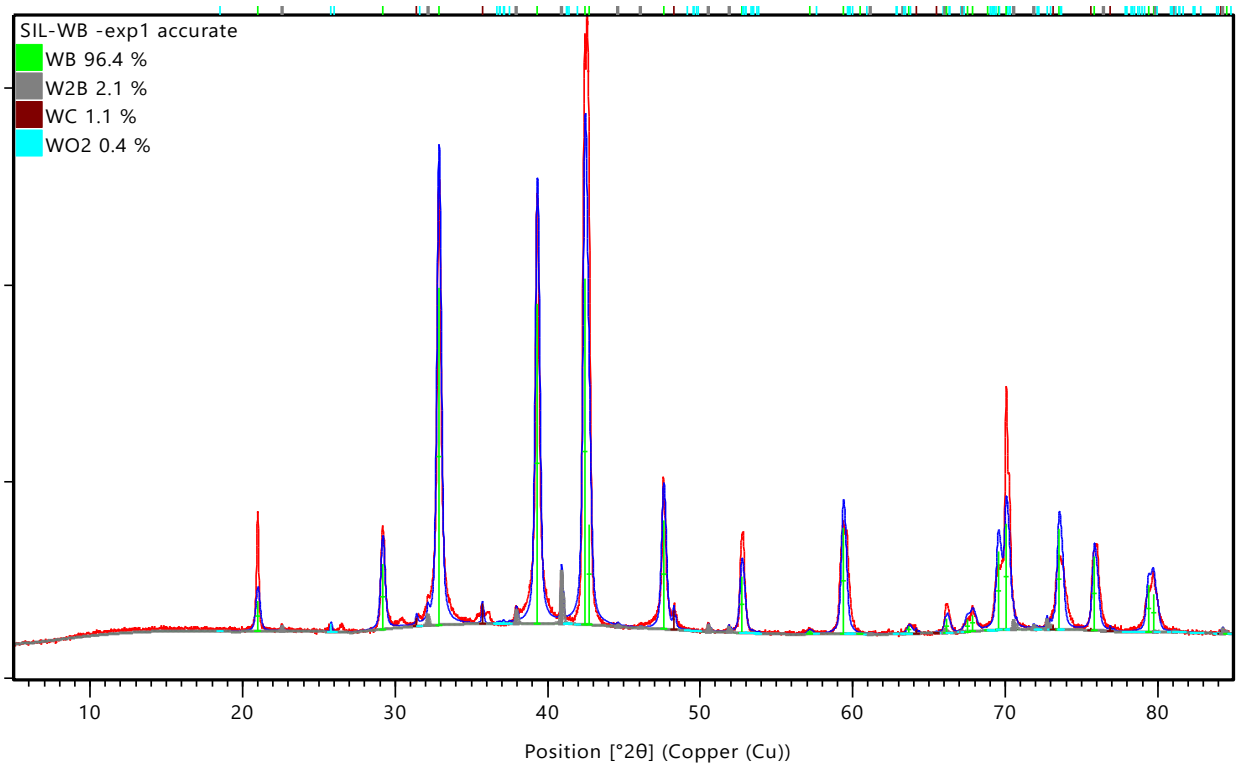

Figure 5.4: XRD pattern of the products of the synthesis of WB after one firing.

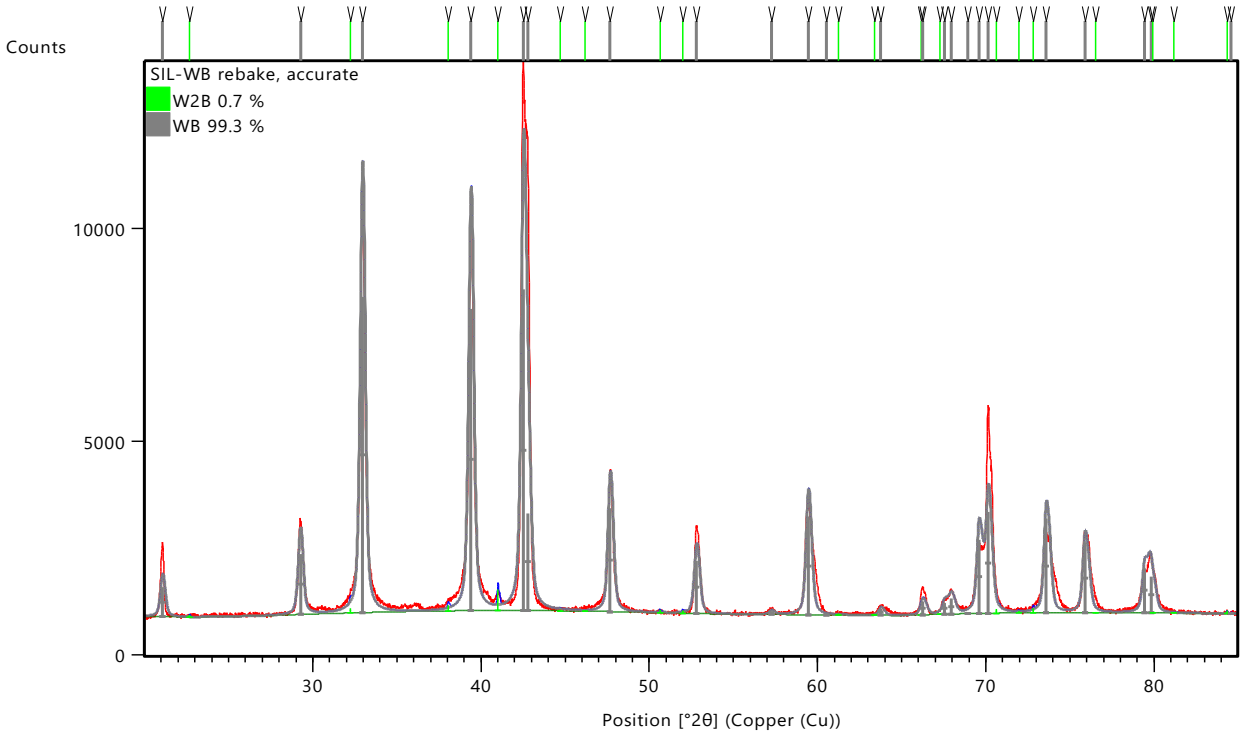

Figure 5.5: XRD pattern of the powders resulting from the second heat treatment of the products of the WB synthesis.

5.2.3. Synthesis of W_2B_5

The recovered pellet has a mass which is 71.4% the mass of the original pellet. Complete conversion to W_2B_5 would be associated with a residual mass of 71.5%. The slightly lower-than-expected mass may be attributed to mass loss during handling of the pellet (e.g., chipping, fretting) or to boron evaporation. All peaks in the XRD pattern, shown in Figure 5.6, can be attributed to W_2B_5 ($P6_3/mmc$, a = 2.9208 Å, c = 17.295 Å). The combination of phase analysis and gravimetric data suggest that W_2B_5 of high purity was obtained.

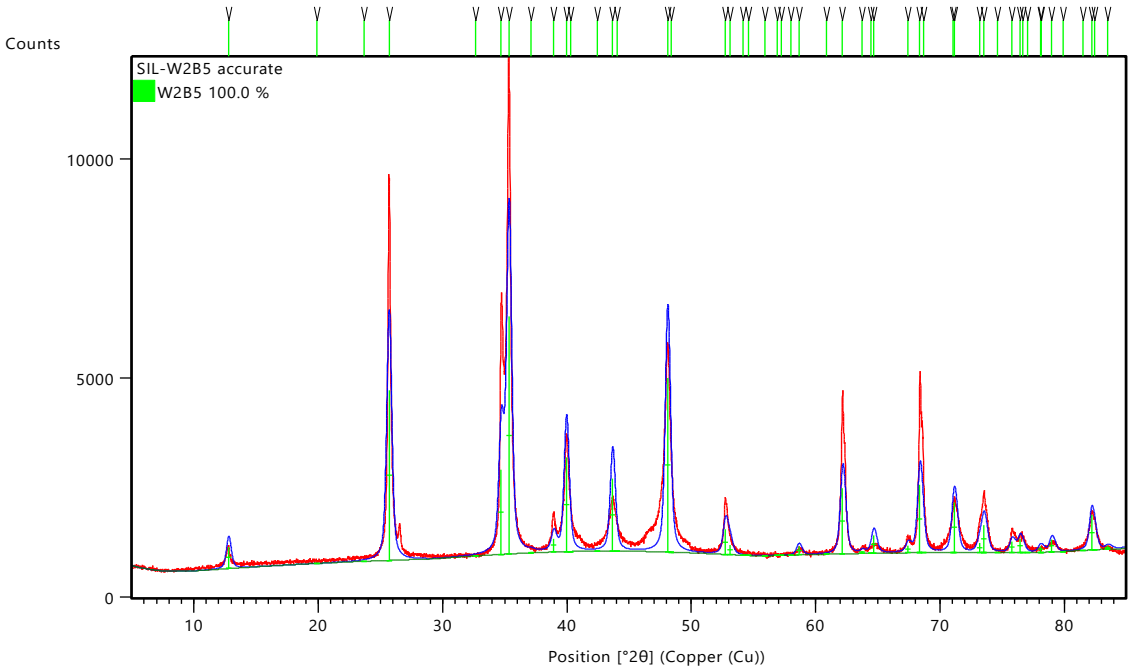

Figure 5.6: XRD pattern of the products of the synthesis of W_2B_5.

Of the three tungsten borides that were prepared, W_2B_5 has the lowest melting point, with the melting points of the borides decreasing with increasing boron content (see Figure 5.1). As a lower melting point is generally associated with a higher diffusivity of the constituent species, and thus faster reaction kinetics, this property may explain the higher conversion achieved for a given reaction time observed in the preparation of WB and W_2B_5 when compared to W_2B.

5.2.4. Considerations on the scale-up of the synthetic routes

The experiments presented in this section highlight a potential synthetic pathway towards tungsten borides, with the one affording W_2B_5 appearing especially promising. The process temperature of 1400 °C employed in the present work does not pose a significant challenge in industrial scale-up when compared to those used in the already established processes for the borocarbothermic production of boride ceramics such as ZrB_2, which is carried out in the 1600-2000 °C range [163], and the concept, method, and handling procedures for the reactants and products share significant similarities. It is also worth noting that the process temperature could be further reduced by exploiting the ample margin of thermodynamic favourability of the reaction (as seen in Figure 5.2),

with the added benefits of reducing boron losses, energy consumption, and unwanted interactions with the crucible material, although likely at the cost of slower kinetics.

6. Chemical interactions and burnup chemistry of UB_2

Understanding the chemical behaviour of a nuclear fuel material is paramount in defining its interactions with the surrounding materials and understanding how its properties may change, both during normal operation and in accident conditions.

UB_2 is generally reported to have a greater affinity for oxygen than UO_2, with its oxidation being highly exothermic. UB_2 is also more reactive towards other substances.

This chapter contains a thermodynamic model for the oxidation of UB_2 that was featured in a publication by Qusai Mistarihi et al. [164], experimental data on the oxidation of UB_2 (collected by Qusai Mistarihi et al. at the University of Manchester and elaborated by the Author), a thermodynamic assessment of the expected chemical behaviour of unirradiated UB_2 upon contact with common materials used in the nuclear industry, a preliminary assessment of the chemical behaviour of irradiation products in UB_2, and the results of DFT simulations of the thermal expansion of UB_2.

6.1. Thermodynamic model for the oxidation of UB_2

A thermodynamic model was developed to calculate the change in enthalpy, entropy, and Gibbs free energy as a function of temperature for various relevant reactions in the U-B-O system, using the thermodynamic data reported in the literature for B_2O_3, O_2, UB_2, UB_4, UB_{12}, UO_2, U_3O_8, and UB_2O_6 [41,124,165–168] and the methodology for thermodynamic calculations reported in Chapter 3. The more negative the variation in Gibbs free energy, the more thermodynamically preferred a given process will be.

The order of preference of the reactions reflects the quasi-equilibrium pathway of the overall process of oxidation of UB_2. The quasi-equilibrium pathway represents the case in which one or more of the reactants are added in infinitesimal increments and the system is allowed to reach chemical and thermal equilibrium after each addition. While notably idealised – no kinetic or diffusion limitations are considered – such a model may still help in predicting which reactions are not spontaneous and which ones may instead be the most likely to occur among the available chemical species.

Figure 6.1a and b show the order of preference of several possible reactions in the U-B-O system. Free energies are calculated at an oxygen partial pressure of 0.215 bar (see Section 6.3) and are referred to the reaction of 1 mol of U (a) and to 1 mol of O_2 (b), representing conditions in which uranium compounds and oxygen are the limiting reactants, respectively. The distinction is achieved by referring the variation in Gibbs free energy associated with each reaction to the amounts of uranium or oxygen involved, respectively, so that the limiting reactant is allocated where it minimises the Gibbs free energy of the products most effectively. It is also worth noting that the order of preference described in Figure 6.1b is independent of the chemical potential of oxygen, since a higher or lower chemical potential of O_2 would uniformly shift all the lines in the plots downwards or upwards, respectively. The order of preference is therefore conserved for any partial pressures of O_2 and for any oxidisers, including water and other oxygen-bearing substances.

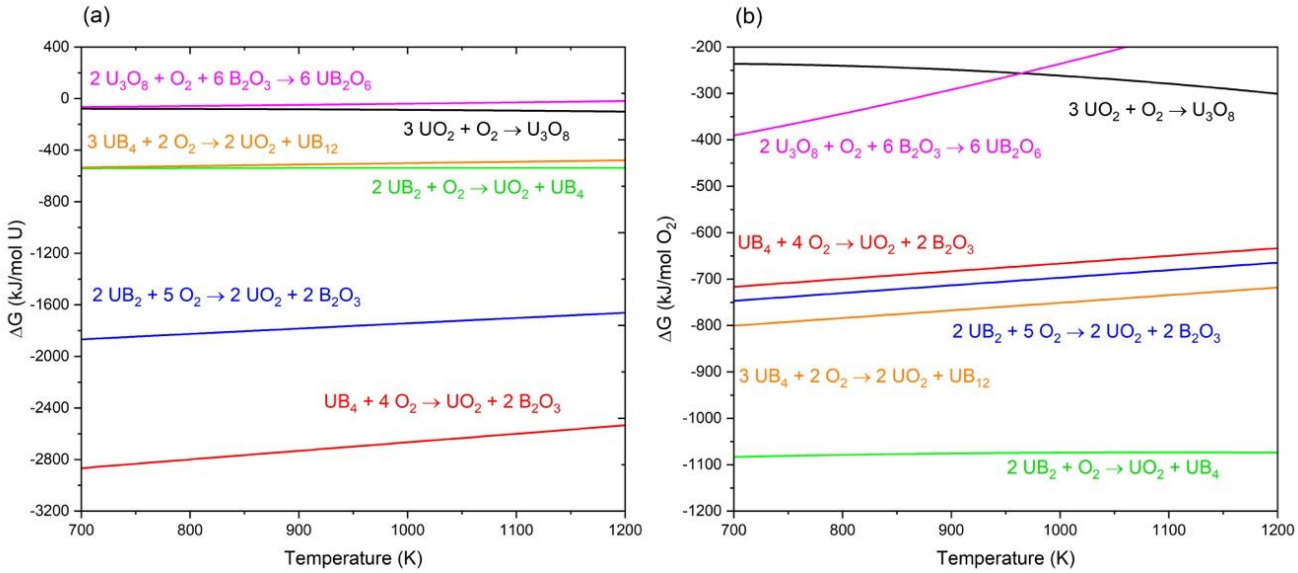

Figure 6.1: Variation in Gibbs free energy for relevant reactions in the oxidation of UB_2.

Figure 6.1a shows that the thermodynamically preferred way to combine UB_2 and O_2 in oxygen-rich conditions is via reaction 6.1 proceeding to completion, followed by the oxidation of the produced UO_2 to U_3O_8 via reaction 6.2. The early stages of the oxidation would necessarily entail the formation of hyperstoichiometric uranium dioxide UO_{2+x}, since UO_2 would be the sole acceptor for oxygen at this point of the pathway [131]. A further oxidation of U_3O_8 and its combination with B_2O_3 result in the formation of UB_2O_6 through reaction 6.3.

$$2\ UB_{2\,(s)} + 5\ O_{2\,(g)} \rightarrow UO_{2\,(s)} + 2\ B_2O_{3\,(l)} \quad 6.1$$

$$3\ UO_{2\,(s)} + O_{2\,(g)} \rightarrow U_3O_{8\,(s)} \quad 6.2$$

$$2\ U_3O_{8\,(s)} + O_{2\,(g)} + 6\ B_2O_{3\,(l)} \rightarrow 6\ UB_2O_{6\,(s)} \quad 6.3$$

It is worth noting that reaction 6.1 is favourable enough to drive reaction 6.2 backwards in both oxygen-rich and oxygen-poor conditions, indicating that UO_{2+x} and U_3O_8 may act as oxidisers when in contact with UB_2. The oxidation would then occur at the interface between the oxide and the boride, ceasing for either thermodynamic or kinetic reasons. In the first case the local chemical potential of oxygen is lowered as the oxidiser is consumed, until it becomes low enough that the reaction stops; in the second case, enough reaction products (B_2O_3 in particular) accumulate and form a barrier layer that separates UB_2 from the oxidiser.

The possibility of uranium oxides acting as oxidisers towards UB_2 may be relevant when they form barriers between UB_2 and a surrounding oxidising environment, since the oxidation of the underlying UB_2 would be thermodynamically favoured and only kinetically limited by the transport of oxygen and boron oxide across the oxide layer. The kinetics of such a process are discussed in greater depth in Section 6.3.

In oxygen-poor conditions (Figure 6.1b), as oxygen is added, the most thermodynamically stable composition is initially obtained by the formal disproportionation of the uranium borides, with U being oxidised to UO_2 and B accumulating into increasingly boron-rich phases such as UB_4 and UB_{12} (Reactions 6.4 and 6.5). As more oxygen is added the higher borides are oxidised to UO_2 and B_2O_3 (Reactions 6.6 and 6.7), which would then react according to reactions 6.2 and 6.3.

$$2\ UB_{2\,(s)} + O_{2\,(g)} \rightarrow UB_{4\,(s)} + UO_{2\,(s)} \quad 6.4$$

$$3\ UB_{4\,(s)} + O_{2\,(g)} \rightarrow UB_{12\,(s)} + UO_{2\,(s)} \quad 6.5$$

$$UB_{4\,(s)} + 4\,O_{2\,(g)} \rightarrow UO_{2\,(s)} + 2\,B_2O_{3\,(l)} \qquad 6.6$$

$$UB_{12\,(s)} + 10\,O_{2\,(g)} \rightarrow UO_{2\,(s)} + 6\,B_2O_{3\,(l)} \qquad 6.7$$

The model can be validated against the available experimental data regarding the U-B-O system. For oxygen-rich conditions, the oxidation of UB_4 in flowing air as described by Guo *et al.* appears to follow the quasi-equilibrium pathway predicted by Figure 6.1, with the process occurring through reactions 6.6, 6.2, and 6.3 [101]. Guo et al. also observed the reversal of reaction 6.3, with the decomposition of UB_2O_6, in air occurring over the temperature range 1273-1473 K (conditions; flowing air, ramp test with a rate of 10 K/min), in agreement with the values reported by Hoekstra *et al*. for static heating (1373 K) [169] and the prediction of the model (1355 K). It must be noted that the evaporation of B_2O_3 will affect the equilibrium of reaction 6.3, so that the observed decomposition temperature will actually depend on the conditions of the experimental setup.

For oxygen-poor conditions, Kardoulaki *et al.* observed the formation of UB_4 and UO_2 in roughly equal amounts at the UB_2-UO_2 interface in solid samples of a UB_2-UO_2 composite heated under an inert atmosphere, with UO_2 acting as an oxidiser. In fact, reaction 6.4 is so thermodynamically favourable that it can strip oxygen from hyperstoichiometric and even hypostoichiometric $UO_{2\pm x}$ at temperatures as low as 700 K, according to the data on the oxygen potential of $UO_{2\pm x}$ reported by Blackburn [170]. While these results provide experimental evidence of reaction 6.4 occurring, no UB_{12} was observed to support the postulated occurrence of reaction 6.5 [84]. However, it must be noted that the sample was not in the quasi-equilibrium conditions that the model assumes. In fact, reaction 6.5 takes over from reaction 6.4 is complete. In the practical case, instead, the majority of the sample was still constituted of UB_2, in the presence of which UB_{12} is unstable owing to reaction 4.25, as demonstrated in Section 4.3.5:

$$UB_{12\,(s)} + 4\,UB_{2\,(s)} \rightarrow 5\,UB_{4\,(s)} \qquad 4.25$$

An analogous UB_4-UO_2 composite was tested by Kardoulaki *et al.* in conditions conducive to reaction 6.5 during the same set of experiments, but no UB_{12} could be identified conclusively at the interface. Nevertheless, an anomaly in the thermal diffusivity suggested the formation of a new phase which could not be detected by XRD, likely because of low crystallinity [84]. The lack of conclusive evidence on the formation of UB_{12} may be due to it forming but having low crystallinity

(and thus not being easily detectable), or to it not forming in appreciable amounts due to a low reaction rate – likely heavily limited by diffusion considering the significant amounts of boron that would require to be relocated to obtain UB_{12} from UB_4.

6.2. Volume change associated with the oxidation of UB_2

As it is oxidised, UB_2 is converted into products with a notably lower density, as indicated by the specific cell volumes in Table 6.1. The oxidation process will therefore entail a significant change in volume, the quantification of which is essential in evaluating the safety performance of UB_2 in nuclear applications.

It is possible to provide an estimate the volume change based on the reported crystalline structures of the compounds involved.

Table 6.1: Specific volume of relevant substances in the U-B-O system in their crystalline form

Substance	Specific cell volume (Å^3/formula)	Reference
$B_2O_{3\ (cr)}$	45.25	[171]
$UB_{2\ (cr)}$	33.84	[42]
$UB_{4\ (cr)}$	48.57	[42]
$UB_{12\ (cr)}$	104.21	[42]
$UO_{2\ (cr)}$	40.87	[172]
$U_4O_{9\ (cr)}$	160.99	[172]
$U_3O_{7\ (cr)}$	121.89	[172]
$U_3O_{8\ (cr)}$	167.28	[172]
$UB_2O_{6\ (cr)}$	115.69	[173]

It must be noted that the estimate likely provides a lower bound to the change in volume, since it assumes ideal crystallinity of the newly produced substances and neglects any effects due to a rapid, exothermic reaction, such as the formation of bubbles and cavities.

Figure 6.2(a) and (b) show the composition change and the volume change that occur as oxygen is added to UB_2 in oxygen-rich and oxygen-poor conditions, respectively.

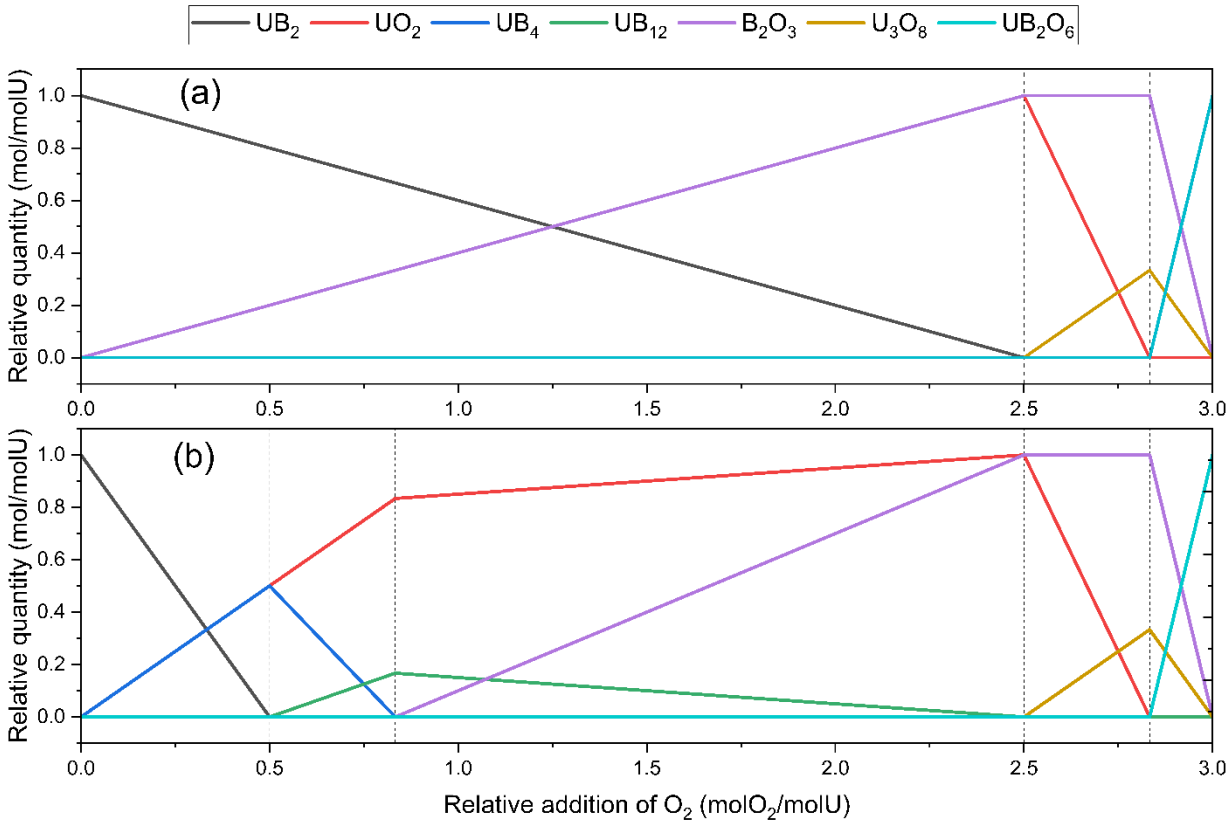

Figure 6.2: Calculated composition change associated with the oxidation of UB_2 during its oxidation in oxygen-rich (a) and oxygen-poor (b) conditions

Figure 6.3 shows the calculated volume change associated with the oxidation of UB_2 in oxygen-rich and oxygen-poor conditions. The oxidation pathway (and thus the volume change) is the same for both cases above 2.5 $molO_2/molU$ (see Figure 6.2). Nevertheless, the volume change between 0 and 2.5 $molO_2/molU$ is strikingly similar as well, despite the two processes occurring on radically different pathways.

Above 2.5 $molO_2/molU$ the oxidation of UO_2 is a highly complex phenomenon, deserving special attention. Upon oxidation the UO_2 lattice (having $Fm\bar{3}m$ symmetry) will initially retain its cubic structure, with the progressive accommodation of negatively charged oxygen ions in interstitial sites and the corresponding increase in the positive formal charge of uranium cations to maintain electrical neutrality leading to increased electrostatic attraction and to a decrease in lattice parameter as the composition shifts to UO_{2+x} [130]. The maximum extent of shrinkage of the cubic structure of UO_{2+x} occurs at x = 0.25, corresponding to U_4O_9, with a cubic structure (having $I\bar{4}3d$

symmetry) and a lattice parameter of 5.44 Å [172] against the original 5.47 Å of UO_2, with a decrease in volume of approximately 1.6% [130].

As U_4O_9 is oxidised to U_3O_7 the cubic symmetry is lost to a tetragonal one (having $P\bar{4}2d$ symmetry) and a slight swelling occurs, but with a total volume that is still lower than the original one of UO_2 by approximately 0.7% [172].

U_3O_7 is then further oxidised to U_3O_8, (with trigonal $P\bar{6}2m$ symmetry), this time with a substantial increase in volume of 36.4% with respect to the original UO_2. However, in real conditions, the actual oxidation process does not follow such a clear, staged path and multiple phases can coexist for kinetic reasons, with the exact reaction path depending on a multitude of factors (to list a few: grain size and porosity of the original material; temperature; partial pressure of oxygen; presence of water vapour; presence of dopants in the original materials) [174]. Seeing how the shrinkage associated with the formation of U_4O_9 and U_3O_7 is overshadowed in magnitude by the overall swelling associated with the formation of U_3O_8 and considering the uncertainty in the composition of the mixture as a function of the extent of oxidation, the volume change associated with the oxidation of UO_2 to U_3O_8 has been linearised for clarity in Figure 6.3, neglecting the intermediate steps.

The complete oxidation of UB_2 to UB_2O_6 results in a final volume that is greater than the original one by approximately a factor of 3.4.

The theoretical mass gain increases linearly with the addition of oxygen and the maximum value (obtained when all UB_2 has been converted to UB_2O_6) is 37%.

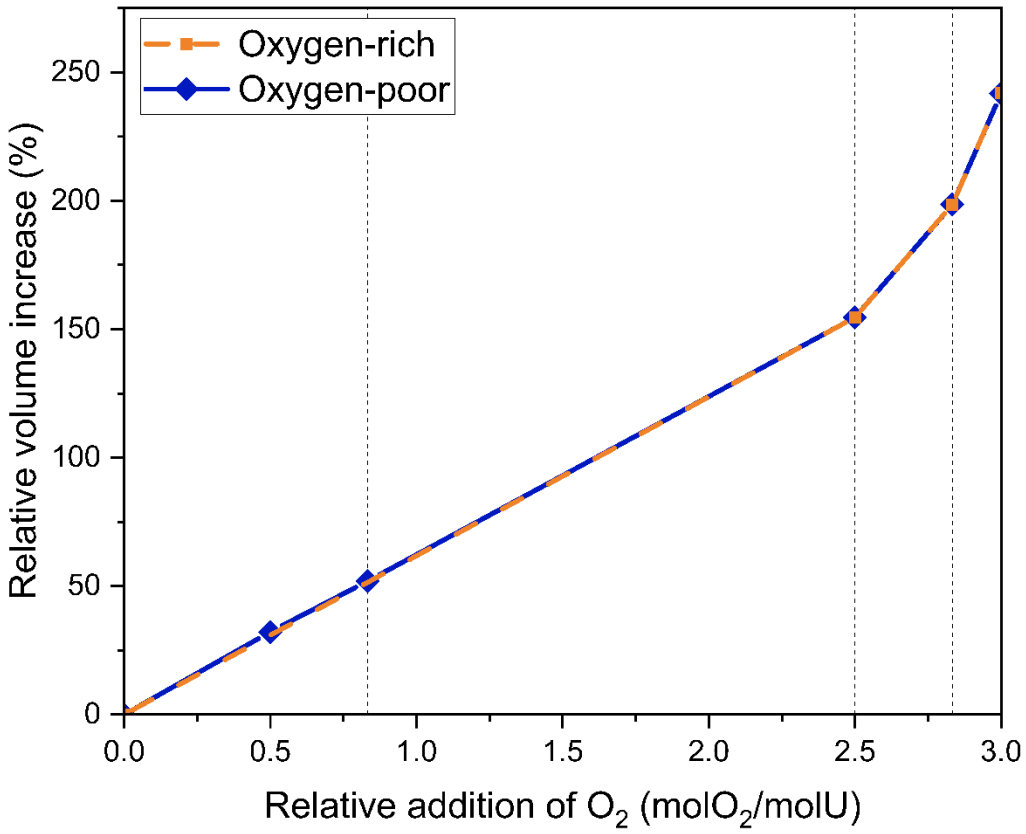

Figure 6.3: Calculated volume change associated with the oxidation of UB_2 in oxygen-rich and oxygen-poor conditions

6.3. Simultaneous Thermal Analysis of the oxidation of UB_2 in flowing synthetic air

UB_2 powder samples were prepared and characterised at the University of Manchester by Dr Qusai Mistarihi, Dr James Buckley, and Dr Joel Turner, as detailed in [164]. XRD analysis and light element analysis revealed a composition of 94% UB_2, 6% UO_2, and less than 0.1% carbon by mass. Oxidation experiments and characterisation of the oxidation products were performed at the University of Manchester. Approximately 20-25 mg of UB_2 material was used in each test, either in powder or fragment form. The fragments had an irregular shape, with an approximate area-equivalent diameter of 0.2-0.7 mm as measured by microscopy, thus making them comparable to the size of 0.5-1.0 mm envisioned for the UB_2 kernels in the UB_2-UO_2 composite fuel concept (see Section 2.4).

TG-DSC was performed using a Netzsch STA449 F1 simultaneous thermal analyser to study the oxidation behaviour of UB_2 during ramp testing. The UB_2 samples were heated in a synthetic air

atmosphere (BOC-certified, 21.49% O_2 in N_2) with a flow rate of 100 mL/min up to 1173 K with a heating rate of 1-10 K/min. The temperature range is representative of the conditions in which air may enter in contact with UB_2 at a manufacturing plant or in a breached reactor pressure vessel following a severe accident.

In the experiments, approximately 1 mmol O_2 per minute was delivered to 0.1 mmol UB_2 over the course of several hours, indicating that the processes may be best interpreted by referring to the oxygen-rich case of Figure 6.1.

Figure 6.4 shows a typical mass change observed during the oxidation of UB_2 powder and fragments with increasing temperature up to 1173 K in flowing synthetic air and with a ramp rate of 3 K/min. The onset of the oxidation reaction (shown in the inset in Figure 4 and defined as the temperature at which 5% of the total observed mass increase was reached) was 807 ± 6 K for samples in fragment form and 799 ± 5 K for samples in fine powder form. The total mass gain on samples shown in Figure 6.4 was 35.2 ± 0.4% and 35.1 ± 0.6% for fragments and fine powder respectively.

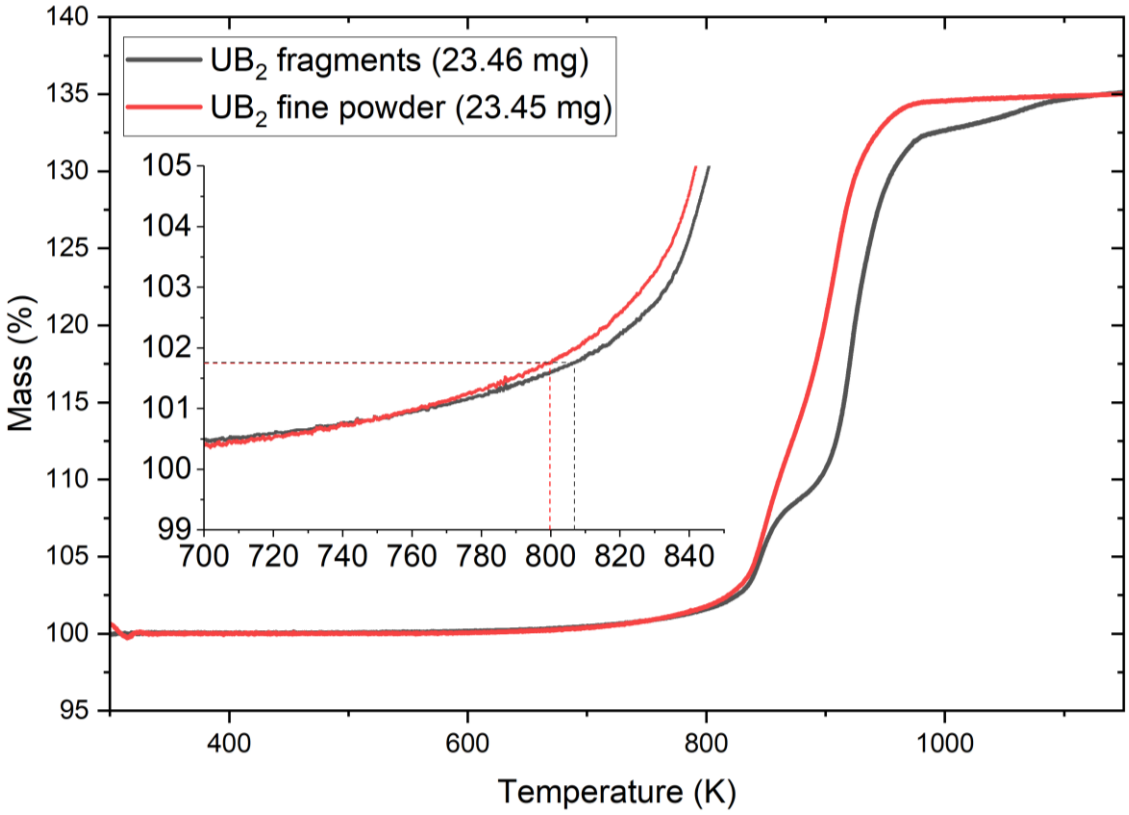

Figure 6.4: Typical mass gain during the air oxidation of UB_2 fine powder and fragments. Inset shows oxidation onset temperatures determined from 5% of the final mass gain.

The XRD pattern of the products of the oxidation testing after the ramp testing up to 900 °C is shown in Figure 6.5, revealing uranium borate (UB_2O_6) as the sole crystalline component, This is in agreement with the thermodynamic model.

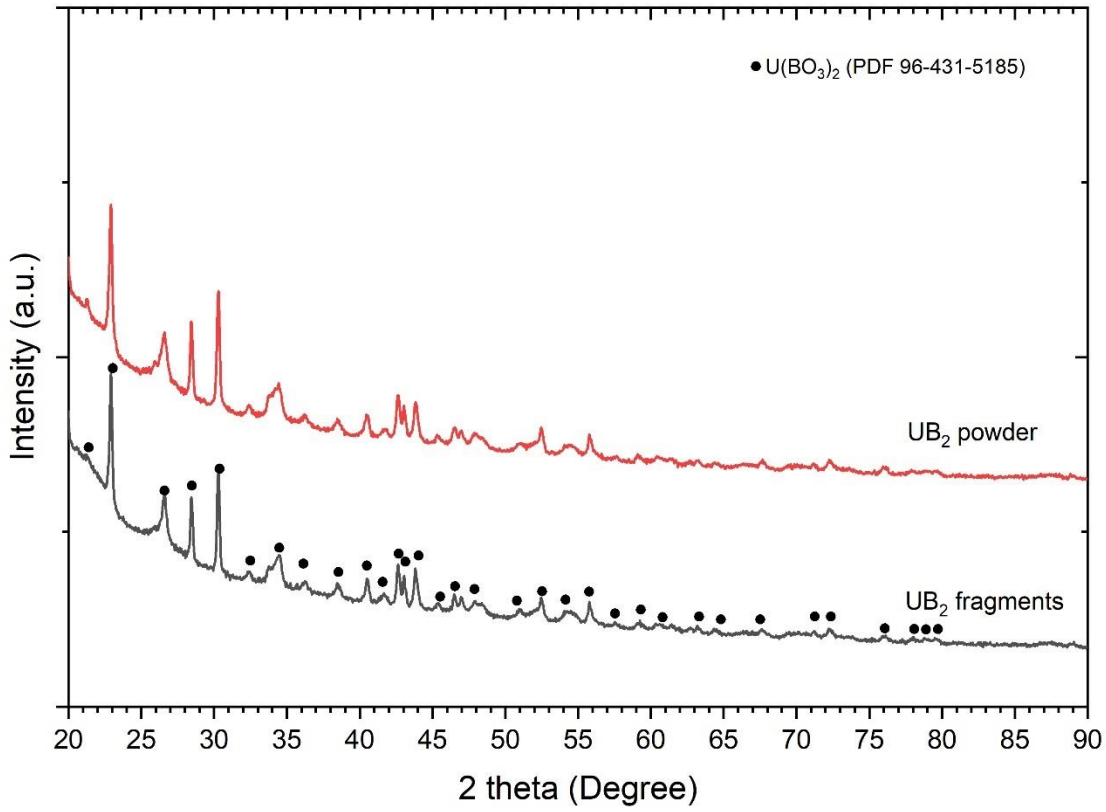

Figure 6.5: XRD pattern of the products of oxidation of UB_2.

The DSC signals measured during the oxidation of UB_2 fragments and powder are shown in Figure 6.6. The oxidation of fragments produced two sharp DSC peaks at approximately 845 K and 921 K, while the oxidation of UB_2 powder appeared to be more uniform, presenting two blunter, overlapping peaks at temperatures of 849 K and 905 K.

The expected value for the total heat produced by the oxidation reaction was calculated by considering the overall process of oxidation of UB_2 to UB_2O_6 through reaction 6.8 as the latter was the sole crystalline material identified among the products.

$$UB_{2\,(s)} + 3\,O_{2\,(g)} \rightarrow UB_2O_{6\,(s)} \qquad 6.8$$

Since the oxidation reaction occurs over a range of temperatures and the enthalpy of reaction depends on temperature, the total heat released by the oxidation process Q_{OX} was calculated through reaction 6.9:

$$Q_{OX} = \int_0^1 \Delta_R H\,(T(X)) \cdot dX \qquad 6.9$$

Where $\Delta_R H(T(X))$ is the enthalpy of reaction as a function of temperature T and X is the extent of reaction as measured by TGA, ranging between 0 (no reaction has occurred) and 1 (reaction complete, i.e. the maximum mass change has been achieved).

Over three replicated runs, fine powders of UB_2 show a mass increase of 34.5 ± 0.6%, while larger fragments show a mass increase of 35.5 ± 0.5%, with the uncertainties being equal to three standard deviations of the set of replicates. The heat released by oxidation was measured by DSC to be 8.2 ± 0.1 J/mg and 8.4 ± 0.1 J/mg, respectively (referred to the initial sample mass).

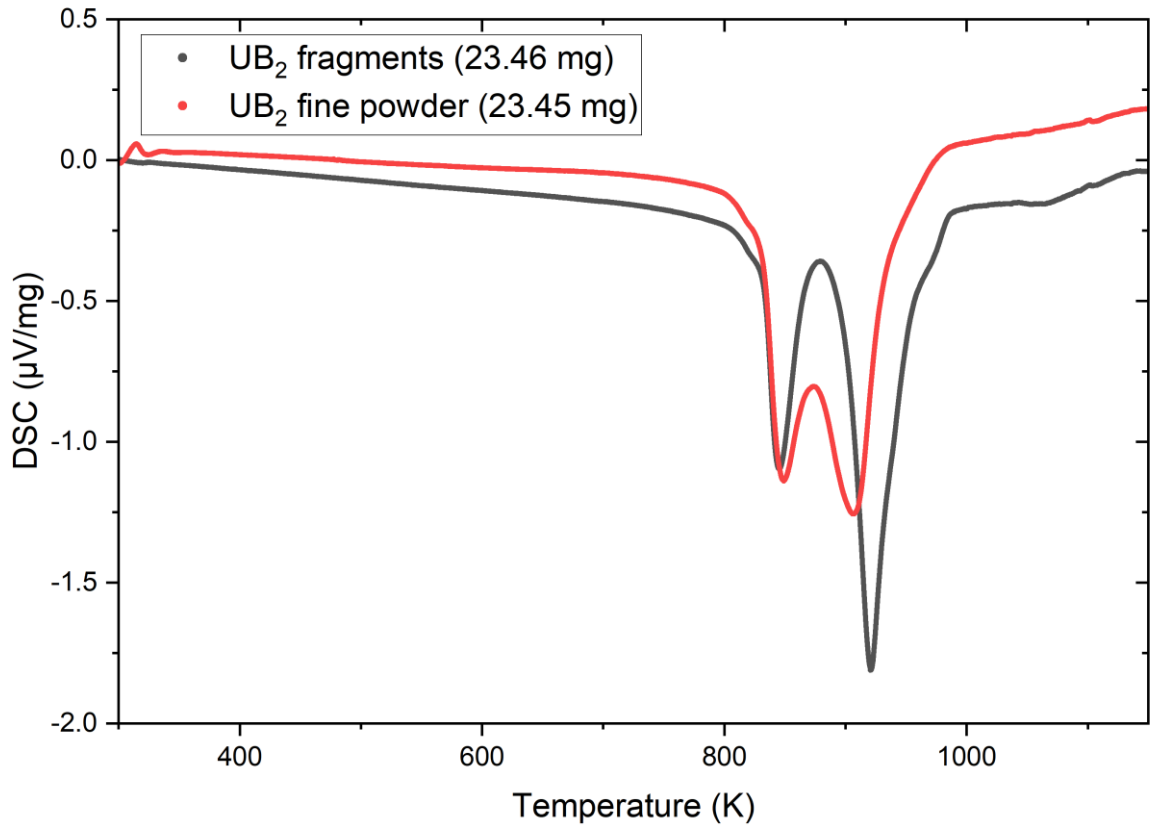

Figure 6.6: DSC profiles during the oxidation of UB_2 fragments and fine powder up to 1173 K

The thermodynamic model predicts that a pure UB_2 sample being completely oxidised to UB_2O_6 would release 9.1 J/mg of heat and would register a 37.0% mass increase. However, considering the initial amount of UO_2 contained as an impurity in the samples (6 ± 1% by mass), which can be assumed to be oxidised to U_3O_8, the predicted values for mass increase and the heat released are reduced to 34.8 ± 0.4% and 8.5 ± 0.1 J/mg.

The values of the mass gain and of the heat released in the oxidation of fine powders and fragments are summarised in Table 6.2, together with the values predicted by the thermodynamic model for the oxidation of pure UB_2 and for a mixture of UB_2 and UO_2 with a composition analogous to the one measured in the samples, showing good agreement between the latter and the experimental data. The uncertainties reported in the table are taken are three standard deviations of the set of three experimental replicates.

Table 6.2: Heat released and mass gain for two theoretical cases and for two sets of experiments in the oxidation of UB_2.

Sample	**Source**	**Heat released**	**Mass gain**
Pure UB_2	Calculation	9.1 J/mg	37.0%
94 wt% UB_2 + 6 wt% UO_2 (± 1%)	Calculation	8.5 ± 0.1 J/mg	34.8 ± 0.4 %
UB_2 powder	Experiment	8.2 ± 0.1 mJ/g	34.5 ± 0.6%
UB_2 fragment	Experiment	8.4 ± 0.1 J/mg	35.5 ± 0.5%

Fine powder samples exhibited systematically lower mass gain and heat released than the fragments tested, although the differences were small and within the bounds of the measurement uncertainty. This phenomenon may be due to a greater extent of pre-oxidation of the samples at room temperature prior to the experiment, resulting from their greater surface area. This interpretation is supported by the fact that the ratio of heat released per relative mass gain is equal within experimental precision across the two sample groups (0.232 ± 0.006 J/(mg·%) and 0.229 ± 0.006 J/(mg·%), respectively), indicating that the mass gain and the heat released are correlated to the amount of unoxidized UB_2 in the samples.

An alternative, but less likely explanation is that, due to the greater surface area of the fine powder samples, loss of volatile B_2O_3 via evaporation may be enhanced during their oxidation, leading to a

smaller net mass gain being observed and to part of the heat produced by the oxidation being used to drive the endothermic evaporation of B_2O_3 [175]. Within work studying the steam reaction with UB_2 a significant mass loss was observed above 1173 K, which was ascribed to this phenomenon; however, no mass loss at high temperature was detected in the present work, suggesting the former description may more readily explain the data [8].

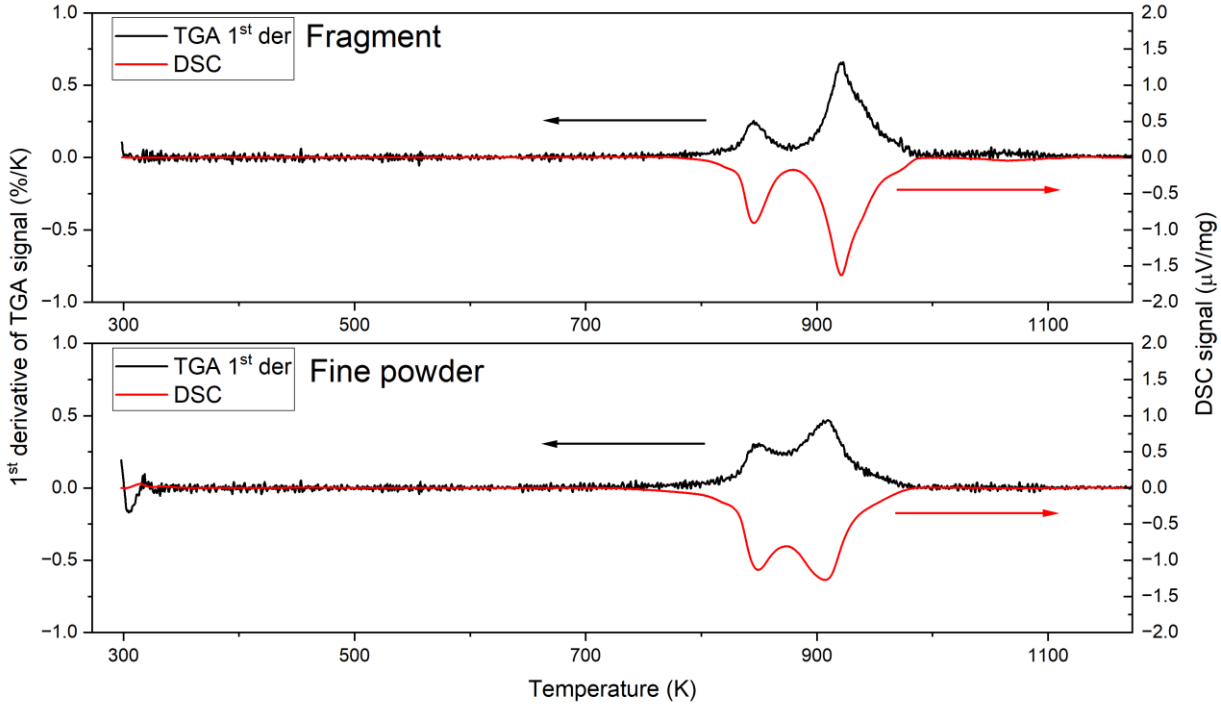

Figure 6.7: 1st derivatives of the mass gain profiles compared with the DSC profiles for the oxidation of UB_2 fragments and fine powder.

For both the fragment and the fine powder samples the two peaks in DSC are matched in position by peaks in the 1st derivative of the mass profile, as seen in Figure 6.7. The ratio between the 1st derivative of the TGA signal and the magnitude of the DSC signal slightly increases with temperature. This is compatible with the trend of decreasing heat released per mass gain across reactions 6.1, 6.2, and 6.3. The peaks are less distinct and occur at lower temperatures in the fine powder samples, suggesting that they may be ascribed to kinetic phenomena.

A possible explanation for the different behaviour of powders and fragments shown in Figure 6.7 would come from a stepwise oxidation behaviour entailing the formation of a barrier layer of oxidation products, which is then disrupted or becomes permeable to oxygen diffusion at higher temperatures. The first peak would correspond to the initial formation of the barrier layer, while the second one to its disruption and to the oxidation of the underlying material. The lower specific surface area of the fragment samples compared to the powder ones would justify the smaller first peak, corresponding to surface oxidation, while the finer and more homogeneous morphology of the powder samples would justify the overlapping shape of the peaks and the overall lower temperature at which they occur.

Figure 6.8 shows the TGA profiles obtained with varying heating rates, demonstrating the effect of the latter on the resolution of the measurements and supporting the thesis of a multi-stage process. At low ramping rates, processes occurring at different times may instead occur at similar temperature values and thus be observed with an insufficient resolution. Up to three stages could be distinctly observed by increasing the ramping rate to 10 K/min, possibly distinguished by the morphology of the barrier layer and by its mechanical resistance and its imperviousness to oxygen.

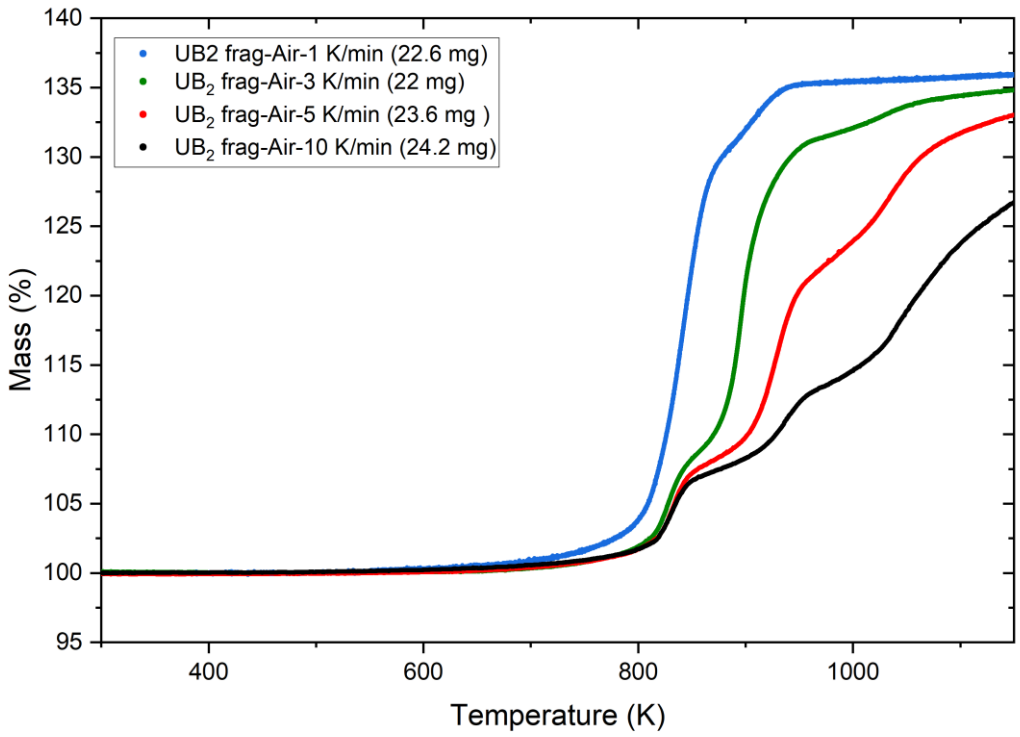

Figure 6.8: Mass gain during the oxidation of UB_2 fragments in air at different heating rates.

6.4. Assessment of the reactions of UB_2 upon contact with metals and ceramics

During its manufacture and its residence in the reactor, UB_2 will be invariably in contact with other solid materials at high temperatures. Ideally, these other materials should not be reactive upon contact with UB_2 or at least not in an exothermic fashion, so as to minimise the chemical energy that is stored in the core. The surroundings of UB_2 inside the reactor will have to be chosen upon careful consideration. The materials included in this analysis should be not only those in the immediate vicinity of UB_2 during normal operation, but also those with which UB_2 may come in contact in the event of an accident – the extreme case being a core meltdown, with full mixing of the contents of the core.

The range of materials that must be assessed must therefore include materials that are currently used for cladding and reactor internals, or that are leading candidates for those applications. A non-comprehensive list of substances (standing in for more complex materials such as alloys) and their possible reactions in presented in Table 6.3.

Table 6.3: Qualitative enthalpy change and spontaneity range of selected reactions of UB_2 with materials relevant to the nuclear industry.

C: barrier layers (element)		
$3\ UB_{2\,(s)} + 2\ C_{(s)} \rightarrow 2\ UBC_{(s)} + UB_{4\,(s)}$	Likely exothermic	All temperatures
Al: claddings and structural materials (element, in alloys), barrier layers (Al_2O_3)		
$UB_{2\,(s)} + Al_{(s,l)} \rightarrow U_{(s,l)} + AlB_{2\,(s)}$	Endothermic	Always unfavourable
$6\ UB_{2\,(s)} + 2\ Al_2O_{3\,(s)} \rightarrow 6\ UO_{2\,(s)} + UB_{4\,(s)} + 4\ Al_{(s,l)}$	Endothermic	Above 1850 K
Si: barrier layers (SiC, SiO_2)		
$3\ UB_{2\,(s)} + 2\ SiC_{(s)} \rightarrow UB_{4\,(s)} + 2\ UBC_{(s)} + 2\ Si_{(l)}$	Likely endothermic	Above 1790 K
$2\ UB_{2\,(s)} + 5\ SiO_{2\,(s)} \rightarrow 2\ UO_{2\,(s)} + 2\ B_2O_{3\,(l)} + 5\ Si_{(l)}$	Endothermic	Above 1710 K
Ti: claddings and structural materials (element, in alloys), barrier layers (TiO_2)		
$UB_{2\,(s)} + Ti_{(s,l)} \rightarrow U_{(s,l)} + TiB_{2\,(s)}$	Exothermic	All temperatures
$UB_{2\,(s)} + TiO_{2\,(s)} \rightarrow UO_{2\,(s)} + TiB_{2\,(s)}$	Exothermic	All temperatures
Cr: claddings and structural materials (element, in alloys), barrier layers (in alloys or Cr_2O_3)		
$(1+x)\ UB_{2\,(s)} + x\ Cr_{(s)} \rightarrow x\ UCrB_{4\,(s)} + UB_{2-2x\,(s)}$	Unknown	Observed at 1973 K
$UB_{2\,(s)} + 4\ Cr_{(s)} \rightarrow U_{(s,l)} + 2\ Cr_2B_{(s)}$	Exothermic	All temperatures

$9\ UB_{2\ (s)} + 10\ Cr_2O_{3\ (s)} \rightarrow 9\ UO_{2\ (s)} + 10\ Cr_2B_{\ (s)} + 4\ B_2O_{3\ (s,l)}$	Exothermic	All temperatures
Fe: claddings and structural materials (element, in alloys)		
$(1+x)\ UB_{2\ (s)} + x\ Fe_{\ (l)} \rightarrow x\ UFeB_{4\ (s)} + UB_{2-2x\ (s)}$	Unknown	Observed at 1973 K
$UB_{2\ (s)} + 4\ Fe_{\ (l)} \rightarrow U_{\ (s,l)} + 2\ Fe_2B_{\ (s)}$	Exothermic below 1400 °C	All temperatures
Zr: claddings, fuels, and structural materials (element, in alloys), barrier layers (ZrO_2)		
$UB_{2\ (s)} + Zr_{\ (s)} \rightarrow U_{\ (s,l)} + ZrB_{2\ (s)}$	Exothermic	All temperatures
$UB_{2\ (s)} + ZrO_{2\ (s)} \rightarrow UO_{2\ (s)} + ZrB_{2\ (s)}$	Exothermic	All temperatures
Nb: claddings, fuels, and structural materials (element, in alloys), barrier layers (Nb_2O_5)		
$UB_{2\ (s)} + Nb_{\ (s)} \rightarrow U_{\ (s,l)} + NbB_{2\ (s)}$	Exothermic	All temperatures
$22\ UB_{2\ (s)} + 10\ Nb_2O_{5\ (s,l)} \rightarrow 22\ UO_{2\ (s)} + 20\ NbB_{2\ (s)} + 2\ B_2O_{3\ (s)}$	Exothermic	All temperatures
Mo: claddings, fuels, and structural materials (element, in alloys)		
$(1+x)\ UB_{2\ (s)} + x\ Mo_{\ (s)} \rightarrow x\ UMoB_{4\ (s)} + UB_{2-2x\ (s)}$	Unknown	Observed at 1973 K
$UB_{2\ (s)} + 4\ Mo_{\ (s)} \rightarrow U_{\ (s,l)} + 2\ Mo_2B_{\ (s)}$	Exothermic	All temperatures
Ta: claddings, fuels, and structural materials (element, in alloys), barrier layers (Ta_2O_5)		
$UB_{2\ (s)} + Ta_{\ (s)} \rightarrow U_{\ (s,l)} + TaB_{2\ (s,l)}$	Exothermic	All temperatures
$22\ UB_{2\ (s)} + 10\ Ta_2O_{5\ (s)} \rightarrow 22\ UO_{2\ (s)} + 20\ TaB_{2\ (s)} + 2\ B_2O_{3\ (s)}$	Exothermic	All temperatures
W: claddings, fuels, and structural materials (element, in alloys)		
$(1+x)\ UB_{2\ (s)} + x\ W_{\ (s)} \rightarrow x\ UWB_{4\ (s)} + UB_{2-2x\ (s)}$	Unknown	Observed at 1973 K
$UB_{2\ (s)} + 4\ W_{\ (s)} \rightarrow U_{\ (s,l)} + 2\ W_2B_{\ (s)}$	Endothermic	Above 660 K

It must be noted that, being based solely on thermodynamics, this assessment cannot take into account kinetic effects such as passivation.

Where possible, only the most thermodynamically favourable reaction for each substance (on the basis of Gibbs free energy change per moles of atoms involved in the reaction) is shown. Where reactions have been reported in the literature, but the thermodynamic data are insufficient in determining which reaction is preferred, the demonstrated reactions with unknown preference are reported as well.

The table also indicates whether the reaction is exothermic or endothermic and the temperature range in which it is thermodynamically favourable.

UB_2 can be reasonably expected to be reactive towards carbon. According to the estimate of the thermodynamic parameters of uranium borocarbide (UBC) reported by Rogl et al. [176], UB_2 will react with carbon to afford UBC and UB_4.

UB_2 is also likely to react with silicon carbide and silicon dioxide, which may be used in claddings for advanced fuels or in barrier layers. However, both reactions are endothermic and expected to be favourable only at temperatures above 1790 K and 1710 K, respectively.

Aluminium metal will not react with UB_2, but its low melting point excludes it from most nuclear applications in its pure form. Nevertheless, the evaluation of the reaction provides some information on the reactivity of the FeCrAl in which it may be employed. Aluminium oxide may react with UB_2, but only at temperatures above 1850 K and in an endothermic fashion.

Compared to other transition metals and their borides, UB_2 tends to have a lower chemical affinity for boron and a greater chemical affinity for oxygen, making it potentially reactive towards many metals that are commonly used in nuclear applications and their oxides.
In fact, many transition metals and their oxides are formally able to strip boron from UB_2 to from their own binary borides, leaving behind metallic uranium or uranium and boron oxide, respectively; this includes Ti, Cr, Fe, Nb, Mo, Ta, and W. The thermodynamically preferred transition metal borides are usually the lower ones, and the reaction is usually exothermic and favourable at all temperatures, with the exception of tungsten, for which the formation of the boride is expected to occur above 660 K and in an endothermic fashion.
Most likely, however, for limited extents of reaction, hypostoichiometric UB_{2-x} [83] will form rather than a mixture of UB_2 and metallic uranium.
However, while the favourability of the formation of the binary borides provides a formal indication that UB_2 is reactive towards a broad class of materials, it is conceivable that ternary borides will be the preferred product instead, especially at high temperatures. Such an occurrence would be in line with the experiments of Rogl *et al*. [177], who equilibrated stoichiometric powder mixtures of the elements at 1700 °C and showed that V, Cr, Mn, Fe, Co, Mo, W, and Re will form mixed borides with the formula UXB_4, where X is one of the aforementioned metals. Nb and Ta did not afford

ternary borides under the same conditions. The occurrence of $UMoB_4$ among the reaction products of the synthesis of UB_2, as seen in Section 4.3, would also support this hypothesis. It is worth noting that the $UMoB_4$ proved remarkably unreactive in subsequent experiments, suggesting that saturating the interface between UB_2 and transition metals with boron may exert a passivating effect.

The formation of ternary U-M-B phases of UB_2 towards Fe, Cr, and Mo would likely translate into strong interactions with FeCrAl alloys, mirroring the formation of ternary U-M-Si phases observed in the interdiffusion zones that form upon contact at high temperature between uranium silicide U_3Si_2 and the metal alloys [178].

6.5. Burnup chemistry of UB_2

As UB_2 is irradiated in a nuclear reactor, both uranium and boron will be transformed by the neutron flux. Uranium will undergo both fission and neutron capture, leading respectively to nuclei of lighter and heavier elements, while boron-10 – composing approximately 20% of naturally occurring boron – will capture neutrons and undergo fragmentation into lithium and helium nuclei.
The properties of UB_2 – and thus its performance as a fuel or as a fuel additive – are expected to be heavily dependent on the chemical state of the fission, transmutation, and fragmentation products.

Neutronic simulations were performed by Mr. Mustafa Bolukbasi at Bangor University using the SERPENT code [179] to predict how the chemical composition of UB_2 is altered by irradiation.
In the simulations, UB_2 was irradiated in a conventional PWR 17x17 fuel assembly, in conditions representative of the operation of a typical GW-scale reactor. The irradiation geometry is shown in Figure 6.9. UB_2 was introduced in 24 modified fuel rods containing pellets with a central, cylindrical UB_2 core (5 mm diameter, in blue in the figure), surrounded by an annular shield of UO_2 (8 mm outer diameter, in yellow). The other 240 fuel rods in the assembly contained only solid UO_2 pellets (8 mm outer diameter, in red). All the uranium in UO_2 and UB_2 had an enrichment of 4.95%.

As burnup progresses, the B/M ratio in the original fuel matrix will decrease, due both to the fragmentation of ^{10}B and to the increase in the number of metal nuclei due to fissions of uranium nuclei. As seen in Section 6.4, it is likely that many fission products will have a greater affinity for

boron than UB_2, thus stripping it of boron to form other compounds and alloys, up to the point at which uranium metal may form. As this is generally seen as an unacceptable safety issue for a ceramic fuel, given the low melting point of uranium metal and its chemical reactivity, it can be expected that there exists a limit of stability for the B/M ratio in the fuel.

Expecting that the fragmentation of boron would have a detrimental effect on the B/M ratio of the fuel and considering that boron of non-natural isotopic composition could be used to improve the performance of UB_2 as a fuel, the simulations were repeated for the irradiation of UB_2 with three different isotopic abundances of neutron-transparent (and therefore more conducive to chemical stability) boron-11: 79.1% (natural abundance), 95%, and 99.5%. The potentially detrimental effect of neutron irradiation on the mechanical stability of boride ceramics was observed experimentally in ZrB_2 and TiB_2, with specimens of natural isotopic composition being far more vulnerable to irradiation [180] than specimens with an isotopic composition of boron tailored toward the ^{11}B isotope [181].

While a good understanding of the compositional evolution of irradiated uranium could be gained from the literature, the neutronic simulations (which aimed at investigating the performance of a UB_2-UO_2 composite as a drop-in replacement for a traditional UO_2 fuel in a conventional PWR) allowed to collect the data with a consistent methodology and in a convenient format as a function of burn-up. Furthermore, no direct irradiation experience exists on UB_2, and no data are available on the fragmentation rate of UB_2 as a function of the isotopic composition of boron.

Based on the results of the simulations – which returned the molar abundances of all elements in the fuel as a function of burnup – and on crystallographic and thermodynamic literature data, a systematic analysis of the possible chemical behaviour of the products of irradiation was performed. In partial analogy with previous studies regarding UO_2 [182,183], five categories (I-V) may be considered for the elements contained in the solid matrix of irradiated UB_2:

- Category I: inert gases
- Category II: volatile elements
- Category III: metallic precipitates
- Category IV: boride precipitates
- Category V: borides that are soluble in UB_2

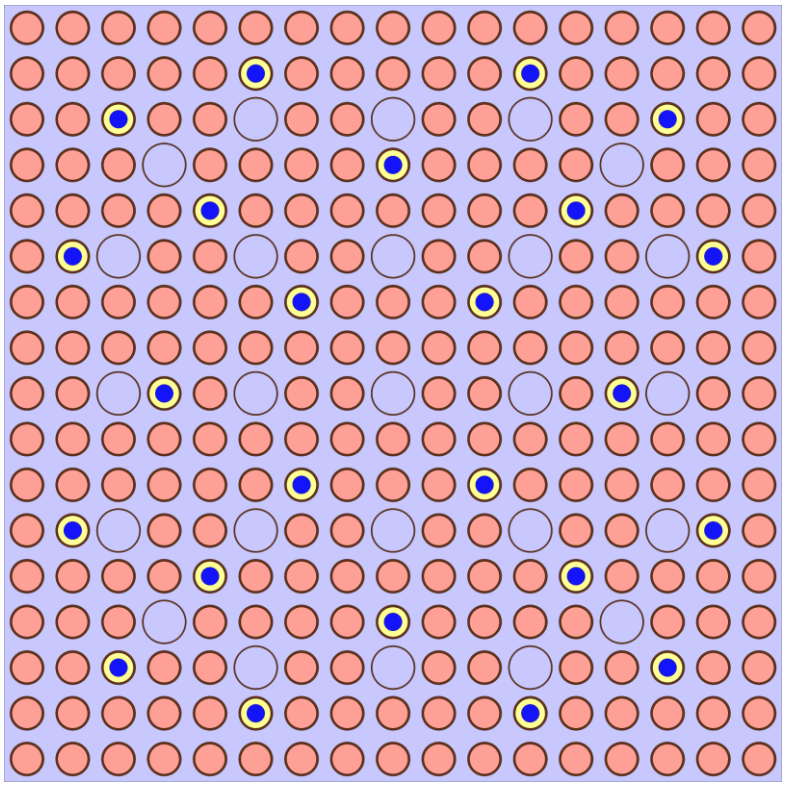

Figure 6.9: Fuel assembly geometry used in the burnup simulations

Not unlike the case of UO_2, some elements may fall in multiple categories depending on the local conditions in the fuel material (e.g., temperature, burnup, presence of other elements and their chemical potential).

Category V is the one for which theoretical predictions may be the most uncertain, given the high complexity of the phenomena that underpin solid solubility in ceramics. Several criteria predicting the mutual solubility of isostructural binary borides are based on their lattice parameters, such as those proposed by Wen et al. for binary diborides [184] and by Gild for high-entropy diborides [185]. The relevant figure of merit is usually related the relative standard deviation of the lattice constants of the constituent diborides in the solid solution.

In this evaluation, the standard deviation itself is used as defined in equation 6.10, but is defined separately for the *a* and *c* directions of the crystal lattice

$$\delta_j = \sqrt{x_H \left(1 - \frac{j_H}{\bar{j}}\right)^2 + (1 - x_H)\left(1 - \frac{j_G}{\bar{j}}\right)^2} \qquad 6.10$$

Where δ_j is the standard deviation on the j lattice parameter, x_H is the molar concentration of the host diboride (in this case UB_2), and j_H, and j_G are the lattice parameters of the host and guest diborides, respectively.

In the present evaluation, only diborides isostructural with UB_2 ($P6/mmm$) were considered to be potentially soluble. Values of 0.3% and 2.5% are taken as thresholds for δ_a and δ_c, respectively, based on the values of a single-phase solid solution of 5% ZrB_2 in UB_2, which was successfully prepared as described in section 6.6.

For a concentration of guest diboride in UB_2 of 2% (with the highest one among the diboride-forming fission products being that of Zr, at 1.6%), such a threshold would allow a maximum difference in lattice parameters between the host UB_2 and the guest diboride of 0.07 Å on the *a* lattice parameter and of 0.70 Å on the *c* lattice parameter. The threshold is roughly inversely proportional to the concentration of solute, with the main limitation to this mathematical description being the large differences in lattice parameters that it allows at very low concentrations of solute.

Table 6.4 shows the main irradiation products of UB_2, their possible chemical forms, and their molar abundance (referred to the total of elements which are not boron or noble gases), in order of increasing atomic number.

Table 6.4: Main fission and transmutation products in UB_2 and their possible chemical forms and abundances.

Element	**Possible chemical forms**	**Abundance (ppm)**
H	H_2, metal hydrides	11
He	Inert	-
Li	LiB_6, LiX (X = halide), Li_B accommodated in V_B sites in UB_2	10334
Br	MBr_x (M = alkali, alkali-earth, transition metals, actinides), BBr_3	92
Kr	Inert	-
Rb	Rb (including in alloys and intermetallics), RbX (X = halide)	1522
Sr	Sr (including in alloys and intermetallics), SrB_6	3723
Y	YB_2, YB_4, YB_6	1948
Zr	ZrB_2	14330

Nb	Nb (including in alloys and intermetallics), Nb_3B_2, NbB, NbB_2	96
Mo	Mo (including in alloys and intermetallics), Mo_2B, MoB, Mo_2B_5, $UMoB_4$	12513
Tc	Tc (including in alloys and intermetallics), TcB, TcB_2	2810
Ru	Ru (including in alloys and intermetallics), Ru_2B_3, RuB_2	8781
Rh	Rh (including in alloys and intermetallics), Rh_7B_3, RhB	1312
Pd	Pd (including in alloys and intermetallics), Pd_4B, Pd_3B, Pd_5B2, Pd_2B	4508
Ag	Ag (including in alloys and intermetallics), AgB_2	242
Cd	Cd (including in alloys and intermetallics)	367
In	In (including in alloys and intermetallics), Ln_3InB (Ln = lanthanides)	6
Sn	Sn (including in alloys and intermetallics), Sn_3Zr_5B, $Sn_5Rh_6B_2$	268
Sb	Sb (including in alloys and intermetallics)	85
Te	Te (including in alloys and intermetallics), BaTe	1458
I	MBr_x (M = alkali, alkali-earth, transition metals, actinides), BBr_3	145
Xe	Inert	-
Cs	Cs (including in alloys and intermetallics), CsX (X = halide)	7706
Ba	Ba (including in alloys and intermetallics), BaB_6	4005
La	La (including in alloys and intermetallics), LaB_4, LaB_6	6
Ce	Ce (including in alloys and intermetallics), LaB_4, CeB_6	6978
Pr	Pr (including in alloys and intermetallics), PrB_6	2883
Nd	Nd (including in alloys and intermetallics), NdB_4, NdB_6	9791
Pm	Pm (including in alloys and intermetallics), PmB_4, PmB_6	352
Sm	Sm (including in alloys and intermetallics), SmB_4, SmB_6	1646
Eu	Eu (including in alloys and intermetallics), EuB_6	362
Gd	Gd (including in alloys and intermetallics), GdB_2, GdB_4, GdB_6	336
Tb	Tb (including in alloys and intermetallics), TbB_2, TbB_4, TbB_6	8
Dy	Dy (including in alloys and intermetallics), DyB_2, DyB_4, DyB_6	7
Ho	Ho (including in alloys and intermetallics), HoB_2, HoB_4, HoB_6	1
U	U (including in alloys and intermetallics), UB_2, $UMoB_4$	889408
Np	Np (including in alloys and intermetallics), NpB_2, NpB_4, NpB_6	895
Pu	Pu (including in alloys and intermetallics), PuB_4, PuB_6	10692
Am	Am (including in alloys and intermetallics), AmB_4, AmB_6	243
Cm	Cm (including in alloys and intermetallics), CmB_6	129

The abundances in Table 6.4 are those obtained from the simulation of the irradiation of UB_2 containing 99.5% ^{11}B irradiated to 60 MWd/kg_{HM}, as they were not notably different from those of the other simulations (with the exception of the concentration of lithium, which depends mostly on the concentration of ^{10}B) and can be considered as representative. The values are rounded to the closest ppm. The abundances of noble gases are not reported, as they are not assumed to form any chemical bonds.

Predictions on the chemical behaviour of the irradiation products are formulated below for each family of elements.

6.5.1. Alkali metals

Lithium is produced mainly from the fragmentation of ^{10}B (although the simulations showed that a very small fraction – approximately 0.002% - of ^{11}B fragmented as well) and its content is therefore highly dependent on the initial ^{10}B content. As suggested by computational studies on ZrB_2, Li atoms are expected to be accommodated in the vacancies left by fragmented B atoms [85]. In any case, a boron vacancy is formed for each event that produces lithium, regardless of the precursor nuclide being ^{10}B or ^{11}B.

No borides of Rb and Cs have been reported [186], and computational studies suggest that such species are unlikely to be stable at pressures below 10 GPa [187]. It is likely that Cs and Rb exist in their metallic state, possibly forming alloys between them.

Based on the observations on UO_2 [182], it is likely that the alkali metals play a crucial role in reducing the chemical potential of free halogens Br and I (which could otherwise exert a corrosive action on UB_2 – see Section 6.5.7) by forming halides of the general formula MX (M = Rb, Cs; X = Br, I).

6.5.2. Alkali-earth metals

The only known crystalline borides of strontium and barium are hexaborides with the formula SrB_6 and BaB_6, respectively [188]. While the literature on the thermodynamic properties of such compounds is sparse, the reported standard enthalpy of formation of SrB_6 of -210.9 kJ/mol [189] suggests that Sr may not be able to strip boron from UB_2 (which has a standard enthalpy of

formation -164.4 kJ/mol [124], while considering that 3 mol of UB_2 must be consumed to produce 1 mol of SrB_6).

Sr and Ba are therefore likely to exist in their metallic state as precipitates in UB_2, potentially forming alloys and intermetallic compounds with other irradiation products such as Te [190], lanthanides, and minor actinides [191], as observed in metallic fuels. It is also worth noting that alkali-earth metals are highly reactive towards oxygen and will likely react with any oxygen impurities present (e.g. from the manufacturing process of UB_2), affording their respective oxides, as observed in metallic fuels [192].

6.5.3. Transition metals

Most of the transition metals among the fission products are able to form alloys with each other, a capability that is fully demonstrated by the formation of metallic nanoparticles in spent UO_2 fuel [193]. In particular, it is possible to distinguish the so-called ε-phase among the metallic nanoparticles, which is composed of an alloy of five transition metals (Mo, Tc, Ru, Rh, Pd) and a *p*-block metal (Te) [194]. It is highly likely that several transition metals will form similar alloys in UB_2, including noble metals Ru, Rh, Pd, and Ag.

The main borides of yttrium are YB_2, [195] YB_4, YB_6, and YB_{12} [196]. YB_2 is isostructural with ZrB_2 ($P6/mmm$) - and hence with UB_2 – with YB_2 being reported to be soluble in ZrB_2, at least up to 2.9 mol% YB_2 [195]. Its lattice parameters are close enough to those of UB_2 (a = 3.102 Å; c = 3.307 Å for YB_2 [197]; a = 3.130 c = 3.988 for UB_2 [42]) and its concentration is low enough for them to form solid solutions under the solid solubility criteria chosen for the evaluation.

Zirconium is likely to form ZrB_2 in solid solution with UB_2, as postulated by DFT simulations [198] and as confirmed by the experiments in Section 6.6.

Niobium can form a range of borides, including Nb_2B_3, NbB, Nb_3B_4, and NbB_2 [199]. As in the case of YB_2, NbB_2 is isostructural with UB_2 and its lattice parameters (a = 3.102 Å; c = 3.307 Å for NbB_2 [197]) would suggest that NbB_2 may form solid solutions with UB_2 under the solid solubility criteria chosen for the evaluation.

Molybdenum can form a range of binary borides (Mo_2B, MoB, Mo_2B_5) [200], although it is likely that a ternary $UMoB_4$ boride may be formed as well in the fuel under irradiation [177].

Technetium borides Tc_3B, Tc_7B_3, and TcB_2 have been prepared and isolated [201]. TcB_2 is not isostructural with UB_2, belonging instead to the $P63/mmc$ space group.

Two borides of ruthenium have been prepared and isolated, with their composition being Ru_2B_3 [202] and RuB_2 [203]. It is worth noting that RuB_2 is not isostructural with UB_2, having instead an orthorhombic lattice $Pmmn$, and is therefore assumed to be insoluble in UB_2.

Several borides of rhodium (Rh_7B_3 and RhB [204]) and palladium (Pd_4B, Pd_3B, Pd_5B2 and Pd_2B [205]) have been described. However, there exists a class of intermetallic compounds between rhodium, palladium, uranium, and plutonium, which are mutually soluble and are described by the general formula $(U_{1-x}Pu_x)(Rh_{1-y}Pd_y)_3$. The melting points of these compounds are notably higher than those of metallic uranium and plutonium, and their chemical stability is considerable [182,206]. It is likely that an analogous intermetallic compound with Ru, prepared in laboratory conditions [206], may form in irradiated fuel, although its presence has only been observed in irradiated substoichiometric UO_{2-x} at high temperatures [182], suggesting that a very low oxygen potential may be required for its formation from UO_2.
Palladium has also been reported to form intermetallic precipitates with lanthanides in irradiated metallic fuel, affording compounds with the general formulas LnPd and Ln_7Pd_3 (where Ln = lanthanides) [207].

The only known boride of silver is AgB_2, isostructural with UB_2 [208], and which may form solid solutions in UB_2 mostly owing to its low concentration, as its lattice parameters (a = 3.000 Å; c = 3.240 Å) are quite different from those of UB_2.

No borides of cadmium are known [209]. It is likely that Cd would be found in metallic form in irradiated UB_2, possibly in alloys or intermetallic phases (likely with Ag, In, Sn, Sb, Te [210]) .

6.5.4. Lanthanides

Hexaborides are the prevalent binary borides of lanthanides, with all of the elements in the family being able to form them [211] and with the hexaborides being often the most stable phase in the Ln-B system (Ln = lanthanide) at room temperature [212]. The hexaborides of the lanthanides, of the alkali-earth metals, and of yttrium are isostructural and exhibit a narrow range of lattice parameters, making them fully miscible with each other [148]. The formation of solid solutions may provide an additional driving force for the formation of metal hexaborides in irradiated UB_2, as the configurational entropy of the mixed phase would provide an additional stabilising term when compared to the isolated hexaborides [213].

Most lanthanides have also been confirmed to form diborides (Gd, Tb, Dy, Ho, Er, Tm, Yb, Lu [214,215]) and tetraborides (all except Pr and Eu [211]).

Furthermore, from observations in irradiated metallic fuel, lanthanides may be found in their native metal state and may form stable intermetallic compounds with Rh, Pd [191], In, Sn, and Sb, the most stable being those with Sb [216]. Lanthanides in their metallic form also appear to have a non-negligible solubility in liquid Cs, which may enhance their mobility in the fuel matrix [216].

6.5.5. Actinides

The diboride, tetraboride, hexaboride, and dodecaboride have been prepared and characterised for Pu [217] and Np [218], while only the tetraboride and the hexaboride were obtained for Am [218]. Furthermore, the diborides of Np and Pu have been reported to be fully miscible over the whole range of compositions [219].

No borides have been reported for Cm, likely owing to experimental difficulties associated with its rarity and radiotoxicity. Nevertheless, in the present analysis it was assumed that it could form CmB_4 and CmB_6, in analogy with Am.

6.5.6. *p*-group metals

No binary borides for In, Sn, Sb, and Te appear to have been reported in the literature. Ternary borides were screened, considering those that contain other elements resulting from irradiation.

La_3InB has been prepared [220] and it is possible that other lanthanides may afford analogous compounds by substituting La in the crystalline structure.

Sn_3Zr_5B [221], $SnRh_3B_{0.81}$, Sn_4Rh_6B, and $Sn_5Rh_6B_2$ [222] have been reported for Sn, while no adequate ternary borides could be found for Sb and Te.

6.5.7. Halogens

Thermodynamic predictions suggest that iodine and bromine resulting from fission may react with UB_2 with a specific corrosion mechanism, indicated in reaction 6.11:

$$UB_{2\,(s)} + 5\ X_{2\,(g)} \rightarrow UX_{4\,(g)} + 2\ BX_{3\,(g)} \qquad 6.11$$

Where X indicates Br or I. Both reactions are favourable, with the calculated equilibrium constants at 1000 K being $3.26 \cdot 10^{31}$ and $9.16 \cdot 10^{7}$ for the reaction with bromine and iodine, respectively.
Since both UI_4 and BI_3 are volatile, the reaction between UB_2 and I_2 could provide a mechanism for the volatilization and enhanced diffusion of boron and uranium inside the fuel rod volume, potentially leading to unwanted chemical interactions or to spatial swings in reactivity as fuel and absorber materials are relocated according to chemical gradients. Furthermore, once mobilised, the volatile species may be deposited again as solids with different mechanisms, such as thermal decomposition into less volatile species upon contact with hot surfaces or condensation upon contact with cold surfaces.

In particular, uranium tetrahalides may decompose into the less volatile trihalides through reaction 6.12, as confirmed experimentally by Bagnall et al. [223]

$$2\ UX_{4\,(s,g)} \rightarrow 2\ UX_{3\,(s,g)} + X_{2\,(g)} \qquad 6.12$$

The transport phenomenon is complex and heavily dependent on the chemical potential of iodine in the fuel environment. However, while a detailed description of the phenomenon is beyond the scope of this preliminary analysis, it is worth noting that the decomposition of fuel-bearing UI_4 in hot spots and the condensation of absorber-bearing BI_3 in cold spots may result in a positive power-temperature feedback that may decrease the temperature homogeneity in the fuel.

From a thermodynamic standpoint, while the corrosion reaction of UB_2 with halogens in itself is favourable, the competing gettering of halogens by alkali metals appears to be extremely effective at limiting the chemical potential of free halogens in the fuel environment (see Figure 6.10), especially considering that the total concentration of alkali metals is almost 40 times greater than that of halogens (see Table 6.4).

Nevertheless, radiolysis of stable alkali metal halides may increase by several orders of magnitude the chemical potential of the free halogen, as observed when irradiating CsI in conditions comparable to those of an active fuel rod inside a nuclear reactor [224,225].

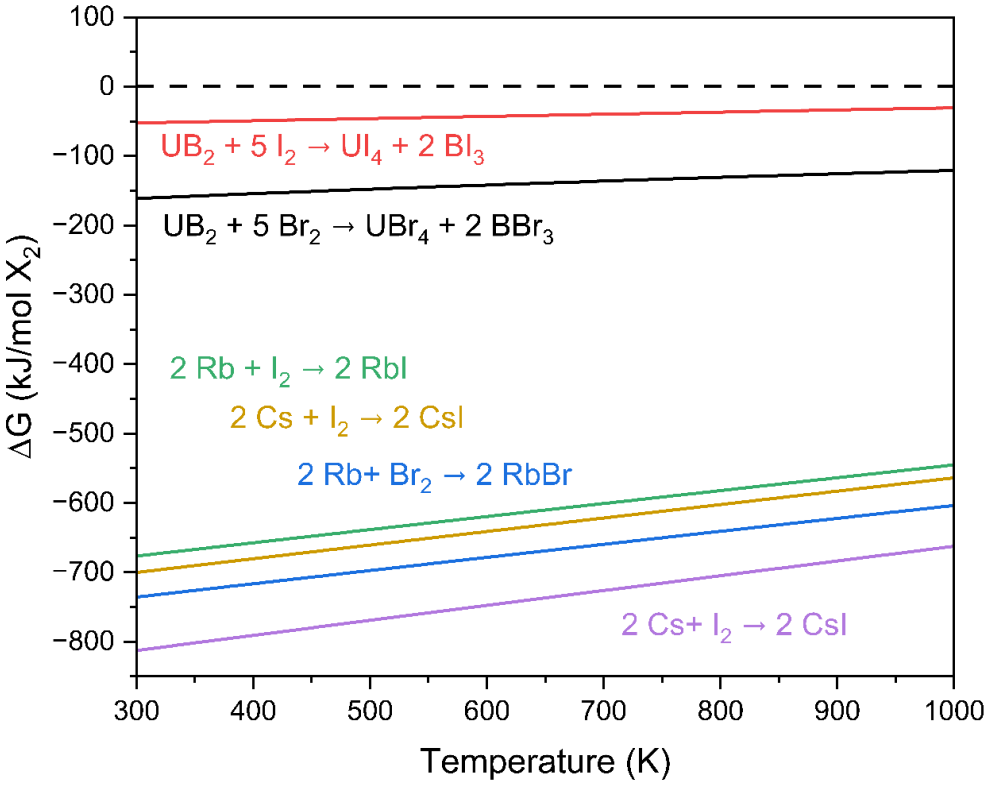

Figure 6.10: Variation in Gibbs free energy for the reactions of UB_2, Cs, and Rb with I_2 and Br_2

6.5.8. Hydrogen and noble gases

Hydrogen (mostly composed of tritium resulting from ternary fission events) is expected to form gaseous H_2 or metal hydrides with metallic fission products or within the cladding [226].
Helium will result from the fragmentation of boron-10 and from ternary fission events. DFT simulations on ZrB_2 predict that its most stable location inn a lattice of that type will be in interstitial positions, from which it can easily diffuse to form bubbles and eventually to the plenum of the fuel element [227].
DFT simulations on the behaviour of Xe in UB_2 suggest that it may be hosted in uranium vacancies in the UB_2 lattice [198]; a similar behaviour can be reasonably expected from Kr.

6.5.9. Systematic classification of irradiation products in UB_2

Table 6.5 presents the results of the previous assessment, providing a tentative placement of the elements into the categories based on available literature data.

Table 6.5: Classes of fission and transmutation products in UB_2

Category	**Elements**
I – inert gases	He, Kr, Xe
II – volatile elements	H, Br, I
III – metallic precipitates	Rb, Sr, Nb, Mo, Tc, Ru, Rh, Pd, Ag, Cd, In, Sn, Sb, Te, Cs, Ba, lanthanides, actinides
IV – boride precipitates	Li, Sr, Nb, Mo, Tc, Ru, Rh, Pd, Ag, In, Sn, Ba, lanthanides, Np, Pu, Am
V – borides that are soluble in UB_2	Zr, Nb, Y, Ag, Gd, Tb, Dy, Ho, Er, Tm, Yb, Lu, Pu, Np

6.5.10. Chemical evolution of UB_2 with burnup

The composition profiles resulting from the simulations (differentiated by the isotopic composition of boron in UB_2: 79.1%, 95.0%, and 99.5% ^{11}B) were used to calculate the amount of boron that

must be available to the fuel matrix for its stability to be guaranteed, i.e. to ensure that no metallic uranium will be formed .

Rather than evaluating the chemical evolution and stability of UB_2 directly and to great detail, considering an extremely complex set of chemical reactions among tens of elements and hundreds of compounds, a preliminary assessment of the phenomenon was carried out by bounding it between a worst and a best case, based on assumptions on the additional demand of boron by the irradiation products and on its decreased availability due to fragmentation.

The UB_2 matrix (including the elements which form soluble diborides) was conservatively assumed to fail if its B/M ratio was reduced below 1.78, corresponding to the lowest stoichiometric ratio found in the literature, reported by Martel et al. [83]. No deviation from the perfect stoichiometry was allowed for the secondary boride phases instead, which were assumed to have complete occupancy of the boron sublattice for a more conservative estimate. In both the best-and worst-case, Li was assumed to be retained in the vacancies left by the fragmentation of boron.

Under the best-case assumptions, all the fission, fragmentation, and transmutation products form their lowest borides or, where possible, remain in metal form, while halogens are perfectly captured by alkali metals.

Under the worst-case assumptions, instead, the highest borides are formed, implying that all of the new elements are able to outcompete UB_2 for boron, while halogens react to completion with UB_2.

Figure 6.11 shows the ranges for the B/M ratio of the main diboride matrix under the best- and worst-case assumptions for the three abundances of ^{11}B that were simulated.

As expected, increasing the fraction of ^{11}B allows to reach higher burnups without compromising the chemical stability of the UB_2 matrix. The behaviour of the best-case scenario curve for the 95.0% and 99.5% ^{11}B cases is interesting in that the B/M ratio of the matrix shows an early decrease followed by an increase, which is even net with respect to initial conditions in the 99.5% ^{11}B case.

The initial decrease in the B/M ratio is likely due to the fragmentation of ^{10}B, 99% of which has been consumed at 42 MWd/kg and 33 MWd/kg for the 95% ^{10}B and the 99.5% ^{10}B case, respectively. The subsequent increase is due instead to a competing effect attributable to the assumptions of the best-case scenario, under which many fission and transmutation products are assumed to be in metallic form or otherwise forming borides with a M:B ratio lower than 2: this leaves the boron atoms that accompanied the fissioned uranium atoms free to remain in the matrix. UB_2 may combine with this free boron to afford UB_4.

Such a behaviour is in part analogous to that of UO_2 undergoing burnup, in which the U/O ratio increases with burnup due to uranium being fissioned into elements forming lower-valent oxides (e.g. Rb(I), Cs(I) Sr(II), Ba(II)), metallic precipitates (e.g. Tc, Mo, Ru, Rh, Pd, Ag), halogens (e.g. Br, I), and noble gases (e.g. Kr, Xe) [228].

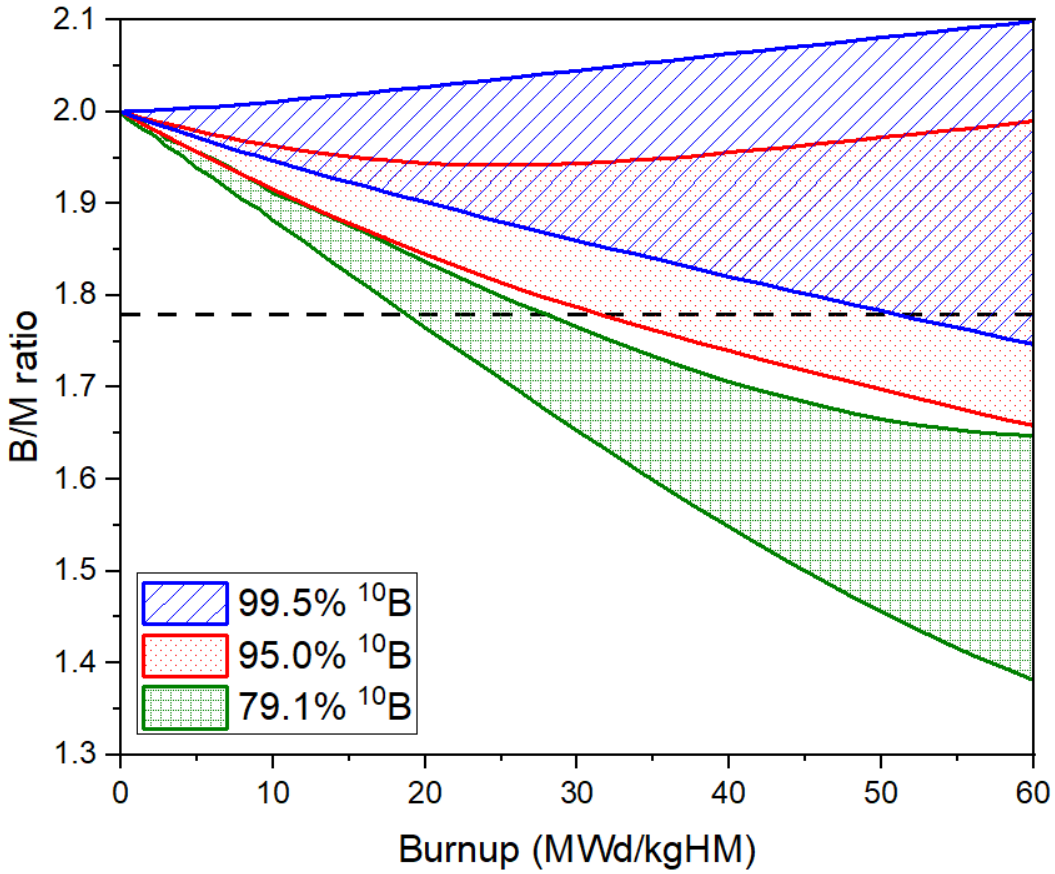

Figure 6.11: Estimated B/M ratio of the UB_2 matrix as a function of burnup for three different isotopic abundances of ^{11}B in UB_2

6.6. Synthesis of (U,Zr)B_2 solid solutions

The synthesis of (U,Zr)B_2 was previously reported by Holleck *et al*. [229] via reactive arc melting of the pure elements. They reported that UB_2 could accommodate up to 10-15% ZrB_2 by moles and that the *a*/*c* ratio decreased with increasing ZrB_2 content, but they did not describe quantitatively the relationship between the ZrB_2 content in (U,Zr)B_2 and the *a* and *c* lattice parameters.
Based on thermodynamic considerations, (U,Zr)B_2 solid solutions were prepared by borocarbothermic synthesis in analogy with reaction 4.1, using UO_2 and ZrO_2 in adequate proportions as starting materials, according to reaction 6.13.

$$2(1\text{-}x)\ UO_{2\ (s)} + 2x\ ZrO_{2\ (s)} + B_4C_{\ (s)} + 3\ C_{\ (s)} \rightarrow 2\ U_{(1-x)}Zr_xB_{2\ (s)} + 4\ CO_{\ (g)} \qquad 6.13$$

The synthesis was performed in the chamber furnace with the procedure outlined in Section 3.4 for x = 0.5%, 1%, 2%, 5%, and 10% in the following conditions: actively pumped vacuum, Mo crucible, dwell time of 12 h at 1900 °C.
The samples were analysed via XRD using a 10% by mass addition of ZrB_2 (ABSCO, UK, 98.5%) as an internal standard to correct for vertical displacement. The composition of the products and the lattice parameters of the (U,Zr)B_2 phase were determined via XRD using the Malvern Panalytical Highscore software. The reference structure used as a starting point for the Rietveld refinement of the ZrB_2 diffraction pattern was the one reported by Baris *et al.* (space group $P6/mmm$, *a* = 3.1703 Å, *c* = 3.5325 Å) [89].
The samples with 0.5 mol%, 1 mol%, 2 mol%, and 5 mol% ZrB_2 all exhibited a single phase of the $P6/mmm$ structural type as the main product, with no peaks attributable to isolated ZrB_2, suggesting that a (U,Zr)B_2 solid solution was indeed formed as the main product. Traces of $UMoB_4$, UB_4, UBC, and UC could be detected as minor impurities (see Table 6.6).

The sample with 10 mol% ZrB_2 showed diffraction peaks attributable to a ZrB_2 crystalline phase in addition to those attributable to (U,Zr)B_2, suggesting that either the solubility limit for ZrB_2 was exceeded or that the dissolution was kinetically limited. Further equilibration of the sample for 12 additional hours at 1900 °C still afforded a material containing unbound ZrB_2, suggesting that the solubility limit of ZrB_2 in UB_2 may be between 5 and 10 mol%.

Table 6.6: Molar fraction of ZrB_2, time at temperature, purity, and other identified crystalline phases for the $(U,Zr)B_2$ samples

ZrB_2 (mol%)	Time at 1900 °C (h)	$(U,Zr)B_2$ purity (wt%)	Other crystalline phases
0.5	12	> 95%	$UMoB_4$, UB_4, UBC
1.0	12	> 95%	$UMoB_4$, UB_4, UBC
2.0	12	> 95%	UB_4
5.0	12	> 95%	$UMoB_4$, UB_4, UBC
10.0	12+12	> 90%	**ZrB_2***, UC

Figure 6.12 shows the shift in the (0 0 2) reflection of $(U,Zr)B_2$ for the 0, 2, and 5% ZrB_2. The shift is in the expected direction, with the *c* lattice parameter decreasing with increasing ZrB_2 content.
The actual concentration of ZrB_2 in the $(U,Zr)B_2$ phase was corrected for the molar amount of uranium which formed other crystalline phases as identified by XRD, while assuming that all of the zirconium was instead involved in the formation of the solid solution. For a 95% pure sample it was therefore assumed that the concentration of ZrB_2 in the solid solution phase was greater by a factor of $(0.95)^{-1}$ than the nominal one.

The relative uncertainty on the concentration of ZrB_2 was estimated to be 5%, which is the quantitative limit of the XRD phase analysis when unsupported by other techniques.
The relative uncertainty (expressed as three standard deviations) in the determination of the lattice parameters of the $(U,Zr)B_2$ phase was estimated as shown in Section 3.4.5 to be 0.03% for the *a* axis and 0.04% for the *c* axis based on the resolution of the goniometer (0.0108 °/step) and on the position of the most intense reflections, with those being the (0 1 0) at approximately 33.0° and the (1 0 0) at approximately 22.3° (the values refer to those for UB_2, as reported by Dancausse [42]). The estimate is in agreement with the typical values reported by Cullity and Stock [128] .

The values of the lattice parameters of the solid solutions, measured by XRD as described in Section 3.4.5, are reported in Table 6.7.

Table 6.7: Measured lattice parameters for the solid solution samples and for pure UB_2 and ZrB_2.

ZrB_2 in UB_2 (mol%)	*a*	*c*
0.00 (pure UB_2)	3.1326 ± 0.0009 Å	3.9857 ± 0.0012 Å
0.53	3.1342 ± 0.0009 Å	3.9841 ± 0.0012 Å
1.05	3.1351 ± 0.0009 Å	3.9798 ± 0.0012 Å
2.11	3.1357 ± 0.0009 Å	3.9769 ± 0.0012 Å
5.26	3.1383 ± 0.0009 Å	3.9687 ± 0.0012 Å
100.00 (pure ZrB_2)	3.1662 ± 0.0009 Å	3.5325 ± 0.0012 Å

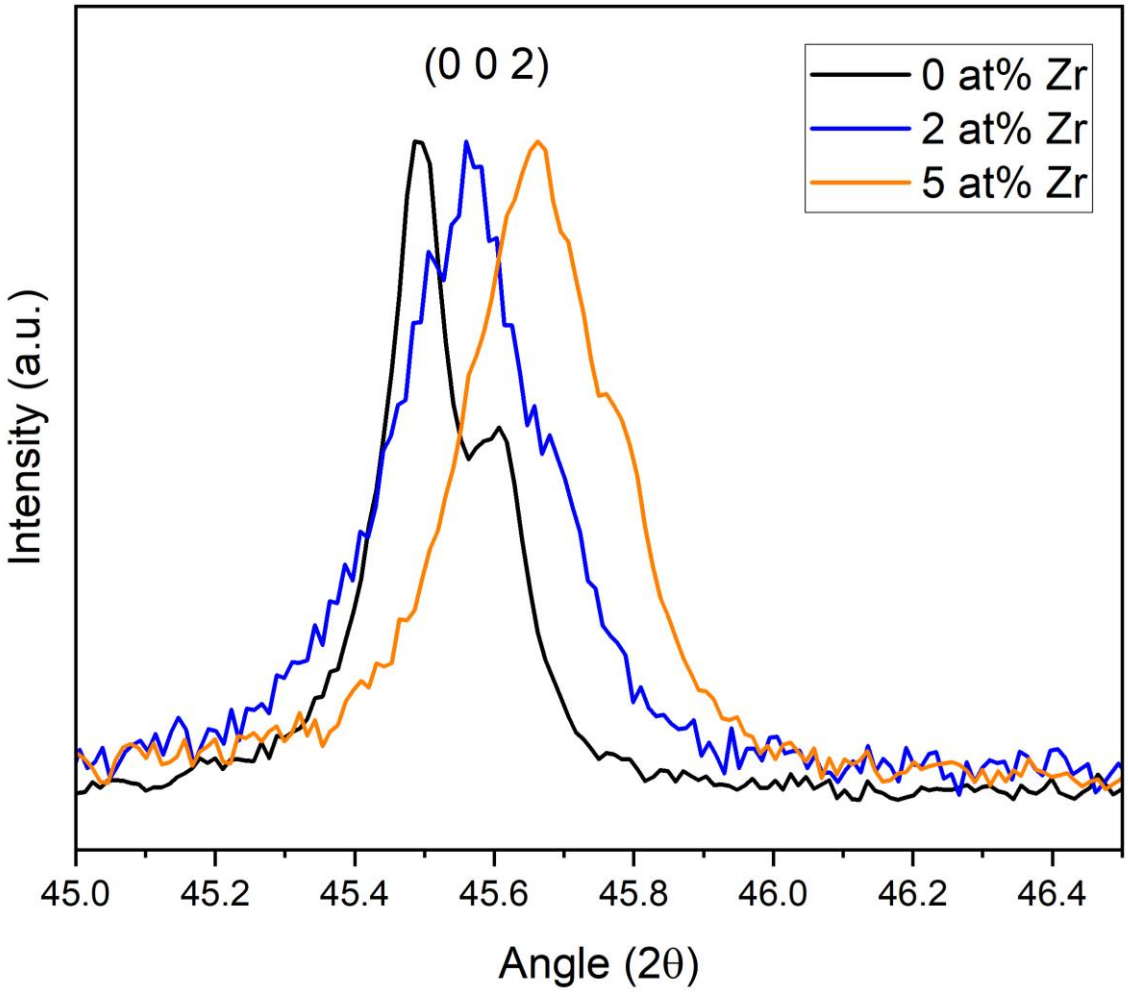

Figure 6.12: Detail of the (0 0 2) reflection in the XRD patterns of three (U,Zr)B_2 samples with varying Zr content.

The change in the *a* and *c* lattice parameters is presented in Figure 6.13, with the dashed line showing the ideal linear variation between UB_2 and ZrB_2. The change in the *a* lattice parameter shows a marked deviation from the ideal behaviour, quickly departing from the dashed line, while the *c* lattice parameter appears to follow it much more closely.

The volume change of UB_2 due to Zr has been predicted by DFT simulations by Jossou et al. [230], who reported a value of -0.11% for 3.7 mol% ZrB_2. Based on the measured lattice parameters, the relative volume change in $(U,Zr)B_2$ for the same concentration of ZrB_2 was estimated by interpolation of the experimental data points (through the dotted lines) as -0.05 ± 0.10%. The relative uncertainty on the calculated volume change is considerable when compared to its actual magnitude, owing to the fact that the effect of the expansion on the *a* direction is largely cancelled by the contraction in the *c* direction. Nevertheless, it is likely that the experimental observations confirm the trend predicted by the simulations.

The calculated reduction in volume is also qualitatively consistent with the fact that the molar volume of ZrB_2 is approximately 9% smaller than that of UB_2, suggesting that the combination of ZrB_2 and UB_2 should afford a solid solution with a molar volume smaller than that of UB_2. From a quantitative standpoint, however, linearising the volume change by applying the ideal mixtures law would return a value of -0.33% at 3.7 mol% ZrB_2, as opposed to approximately -0.10% as measured experimentally and as calculated by DFT, indicating that the behaviour of the U-Zr-B system is notably distant from an ideal one. This could be ascribed to Zr weakening the delocalisation (and thus the strength of the bonds) of the *f* electrons in the uranium planes, as indicated by the more-than-linear swelling in the *a* direction.

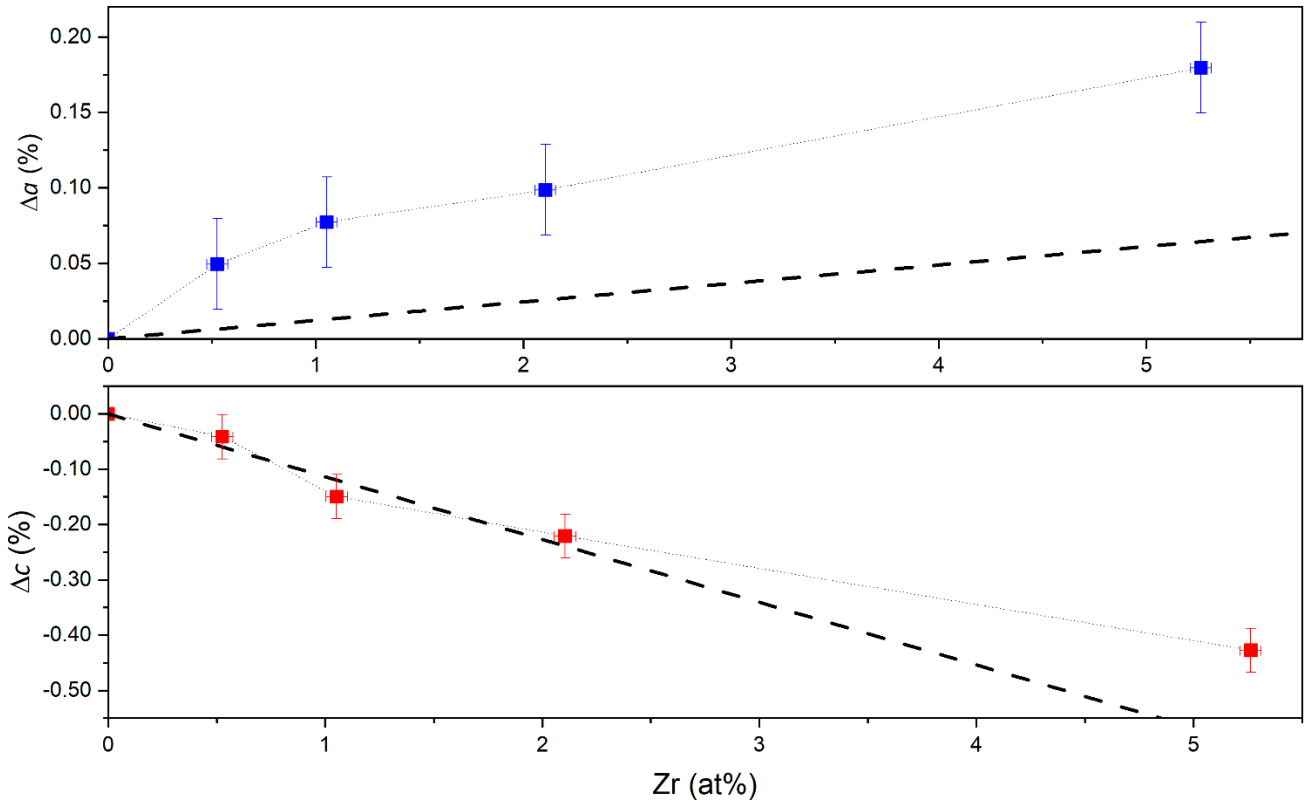

Figure 6.13:Variations in the lattice parameters of the unit cell of (U,Zr)B_2 as a function of Zr content.

6.7. Simulation of the thermal expansion of UB_2

The thermal expansion of a material in a nuclear fuel has profound effects on its nuclear properties and on the mechanical stresses that will be generated if its expansion is constrained by the surrounding materials.

The nuclear properties are affected by the change in the number density of the fissile and absorbing atoms. In fact, the thermal expansion of nuclear fuels and moderators is one of the key phenomena that allow to build and operate fission reactors with negative temperature coefficients of reactivity. Thus, an accurate coupled thermal-neutronic model of UB_2 as a nuclear fuel must include its coefficients of thermal expansion.

The linear coefficient of thermal expansion (CTE) of UB_2 has been measured by Beckman and Kiessling [231] and by Kardoulaki *et al.* [43].
The measurements of Beckman and Kiessling were performed on polycrystalline powder samples by XRD, measuring the lattice parameters as a function of temperature and reporting the linear coefficients of thermal expansion of UB_2 along the *a* and *c* axis. The values are averaged between room temperature and 205 °C and provide the crystallographic linear CTEs.
The measurements of Kardoulaki *et al.* were performed on polycrystalline samples in a dilatometer between room temperature and 1500 °C, providing the technical linear CTE.

It must be noted that the crystallographic CTE and the technical CTE are related but not readily comparable, as they do not arise from the same set of phenomena. In fact, the technical linear CTE results from the combination of the thermal expansion effects due to the idealised crystal lattice (which are the very ones measured by XRD) and of those due to the microstructure and to the non-ideality of the crystals. The crystallographic linear CTEs feature in the technical linear CTEs as their average, weighted with the ordering of each crystallographic axis along the measurement direction; for a truly random ordering of crystallites, the technical CTE should therefore be linearly correlated with the average of the crystallographic CTEs. The other contribution to the increase in dimensions measured by technical dilatometry results from the increase in concentration of crystal defects with temperature, with both vacancies and interstitials being able to cause expansions or contractions of the lattice, and often in an anisotropic fashion [232–234].

Beckman and Kiessling reported averaged values of CTE of 9 ppm/K along the *a*-axis and 8 ppm/K on the *c*-axis in the 20-205 °C range, with a weighted average (2 *a* axes and 1 *c* axis in the crystal lattice) of 8.67 ppm/K, while the technical linear CTE reported by Kardoulaki *et al*. over the same temperature range is approximately 10 ppm/K, showing good agreement between the two measurements when considering the caution with which crystallographic and technical CTEs should be compared.
The technical CTEs reported by Kardoulaki *et al*. [43] are encouraging with respect to the inclusion of UB_2 into UO_2 as a dispersed phase: the values of the two materials are closely matching and the total linear thermal expansion of UB_2 at 1600 K is greater than the one of UO_2 as recommended by Fink [41] by less than 0.1% (referred to the original length), while UO_2 is able to accommodate strains that are up to 3 orders of magnitude greater before fracture at such temperatures owing to increased plasticity [235].

However, both sets of measurements refer to unirradiated UB_2. It can be reasonably expected that the inclusion of soluble fission and fragmentation products in the UB_2 matrix (see Section 6.5) will alter the linear CTEs of UB_2.

Measuring the CTE of suitable surrogate materials or of irradiated samples of UB_2 can provide direct information on the matter but is also experimentally challenging: in the first case the issue lies with the preparation of compositionally and microstructurally representative samples, while in the second case the challenges derive from the intense radioactivity of the samples. At the same time, versatile DFT simulations may be used to predict the thermal expansion of the UB_2 matrix with a variety of doping elements and inform, direct, and focus experimental work.
The first step for such a line of work is the validation of the method and of the parameters that are used to perform the simulations against the available measurements. Once the behaviour of unirradiated UB_2 has been simulated with sufficient accuracy, the simulation method can then be extended to more complex materials based on the same matrix.

Using DFT-QHA calculations as described in Section 3.3, the volumetric CTE of UB_2 was calculated to be 15.0 ppm/K. This would be equivalent to an average linear CTE of 5.0 ppm/K, far lower than those reported in the measurements.

For a more accurate description of the phenomenon, the workflow of DFT-QHA was altered to take into account anisotropy effect. Recalling equation 3.35, it is possible to make explicit the dependency of cell volume on the *a* and *c* lattice parameters, obtaining equation 6.14

$$G(V,T) = E_{lattice}(V) + E_{phonons}(V,T) \quad 3.35$$

$$G(a,c,T) = E_{lattice}(a,c) + E_{phonons}(a,c,T) \quad 6.14$$

The relaxed unit cell of UB_2 obtained by the previous DFT-QHA work was used as a base to generate deformed structures, which were obtained by varying independently the *a* and *c* parameters in the +/- 5% range with respect to the relaxed values, with a step of 1.25%.

The a_i and c_j parameters used in each calculation were defined as

$$a_i = a_r \cdot (0.95 + 0.125 \cdot i) \quad 6.15$$

$$c_j = c_r \cdot (0.95 + 0.125 \cdot j) \quad 6.16$$

Where a_r and c_r are the values of *a* and *c* obtained from the first relaxation of the unit cell and where *i* and *j* vary between 0 and 8.

Thus, a 9x9 array comprising 81 structures with different pairs of (a_i, c_j) values was obtained. The structures in the array were relaxed in VASP allowing movement of the atoms while keeping constant the lattice parameters and the cell shape. The resulting structure output files were used to build the corresponding 4x4x3 supercells, thus obtaining an array of 81 supercells.

The supercells were input in the DFT-QHA workflow described in Section 3.3, calculating the phonon contribution to the free energy of each cell as a function of temperature under the quasi-harmonic approximation, as conceptually expressed by equation 6.14. Calculations were performed for the 0-500 K range, with a step of 10 K. For each temperature. the 9x9 array represents a

sampling matrix for the potential energy surface in the (a,c) space, as shown in Figure 6.14. The sampling points are indicated by the blue dots.

The potential energy surface was numerically reconstructed for each temperature value using a third-order polynomial fit of the $G(a_i, c_j, T)$ values.
For each temperature, the coordinates of the minimum of the energy surface were found numerically form the fitting function and were taken to be the equilibrium values of a and c at said temperature. The resulting (a, T) and (c, T) data points were fitted to obtain $a(T)$ and $c(T)$ functions, respectively.

Using linear interpolation of the functions, the smeared linear CTE in the 20-205 °C range was calculated to be 3.6 ppm/K along the *a* axis and 8.0 ppm/K along the *c* axis.

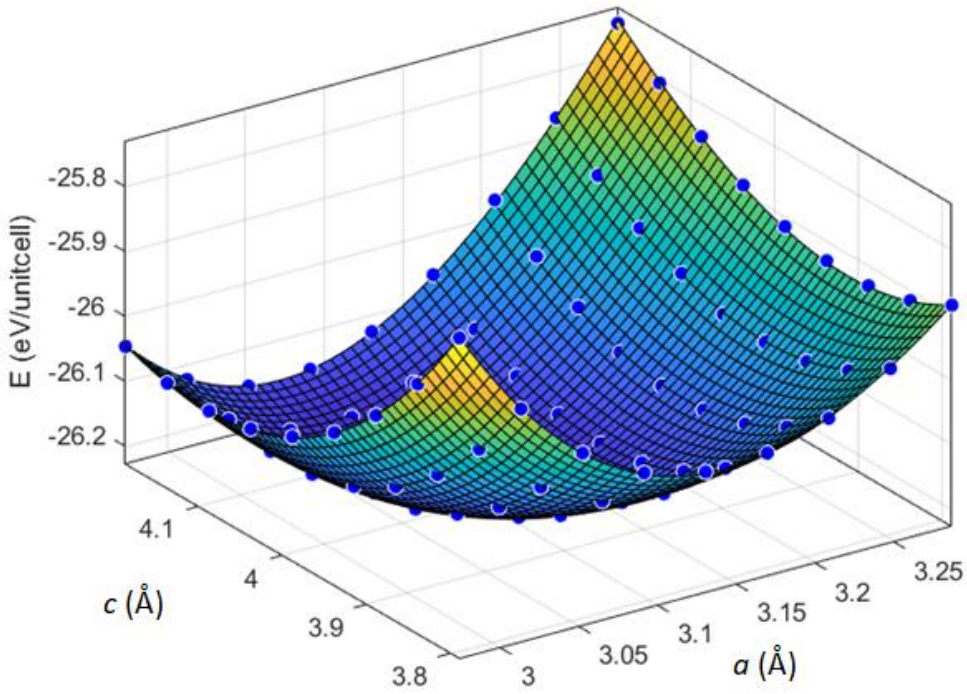

Figure 6.14: Potential energy surface of the UB_2 cell as a function of the lattice parameters at a temperature of 290 K.

Table 6.8 summarises the available literature data discussed at the beginning of this section and the values resulting from this analysis. The volumetric CTEs of Beckman *et al.* and of Kardoulaki *et al.*

are calculated as the sum of the crystallographic linear CTEs in the three directions and as three times the technical linear CTE, respectively.

It appears that the VASP-QHA method is consistent between the isotropic and anisotropic approach, as shown by the closely matching values of the volumetric CTE (15.0 ppm/K and 15.2 ppm/K, respectively). The anisotropic simulations appear to capture well the thermal expansion along the *c* direction, while the main source of discrepancy appears to be the expansion along the *a* axis, possibly due to anharmonic effects that the QHA is unable to reproduce [236].

Table 6.8: Values of the reported and calculated coefficients of thermal expansion of UB_2.

Source	Linear CTE, *a*	Linear CTE, *c*	Volumetric CTE
Beckman *et al.* [231]	9 ppm/K	8 ppm/K	26 ppm/K*
Kardoulaki *et al.* [43]	-	-	30 ppm/K**
Isotropic DFT-QHA	-	-	15.0 ppm/K
Anisotropic DFT-QHA	3.6 ppm/K	8.0 ppm/K	15.2 ppm/K

** calculated from the crystallographic CTEs by summation*

*** calculated from the technical linear CTE by multiplying by 3*

7. Research and development needs

As seen in Section 2.4, the main aims of this thesis revolved around the study of the feasibility of a nuclear fuel based on a UB_2-UO_2 composite pellet, with a focus on the manufacturing of UB_2, on its interaction chemistry with other materials, and on its physical properties. Figure 7.1 shows a proposed pathway for the development effort of such a composite fuel, combining its manufacturing and qualification. The development pathway would be split ideally into three tracks, those being respectively modelling, testing, and manufacturing. Modelling will be initially used to inform the design and direct the manufacturing, while manufacturing will provide materials for analysis, which will in turn provide data to progressively refine the model [237].

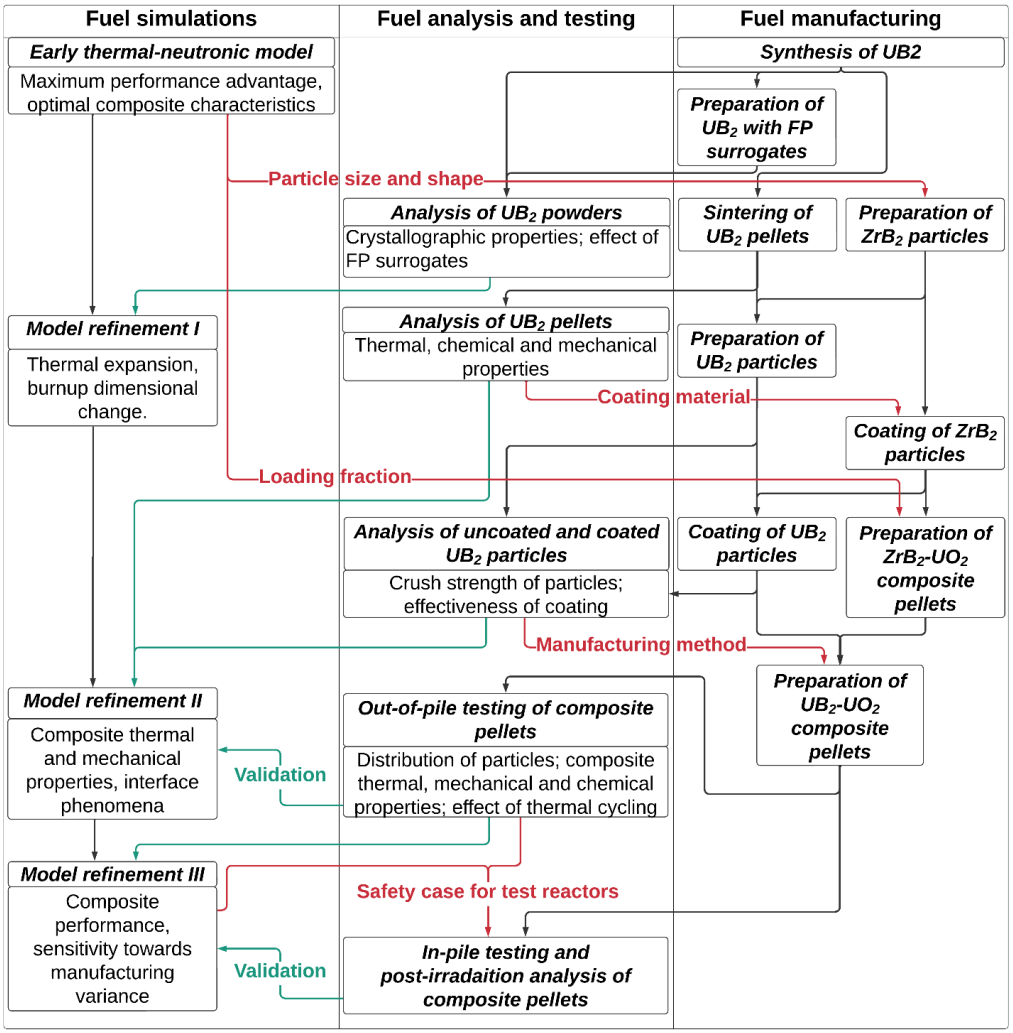

Figure 7.1: Flowchart of the proposed pathway towards the evaluation and testing of a UO_2-UB_2 composite fuel.

The work presented so far advanced chiefly the manufacturing and analysis tracks, developing an economical, scalable and consistent method to prepare UB_2 and applying it to the preparation of UB_2 doped with Zr to understand the effect of the inclusion of the latter as a fission product on the crystal lattice, as well as modelling the chemical reactivity of UB_2 and validating it against experimental data in the case of the reaction with air. The synthesis routes presented in this work can also be regarded as contributing to making uranium and tungsten borides widely available for testing by other research groups through relatively simple and inexpensive methods, further supporting the research efforts in the field.

This thesis contributed to the simulation track as well, with the results of the assessment of the chemical behaviour of UB_2 and of its chemical stability against burnup allowing to screen promising materials and coolants for fuel and reactor concepts and to investigate acceptable $^{11}B/^{10}B$ ratios in neutronic simulations. Finally, the DFT-QHA simulations showcased the shortcomings of QHA in describing the thermal expansion of UB_2 and suggested pursuing an anharmonic treatment of the lattice vibrations.

This work has advanced the state of knowledge on the manufacturing of uranium and tungsten borides and on the chemical behaviour of UB_2.

7.1. Simulations and modelling

Modelling is crucial in the first step in the evaluation of any ATF candidate. Before resources are committed to the development of the concept, it is paramount to estimate the maximum gain in performance that the concept may offer while satisfying certain constraints. In the present case, it is expected that such constraints may be the maximum volume fraction of the dispersed phase, the isotopic composition of uranium and boron, or the compatibility with a certain reactor design.

7.1.1. Preliminary feasibility studies

The preliminary modelling should be carried out with multi-scale and multi-physics simulations aimed at understanding the neutronic and thermal advantage offered by the composite owing to the burnable absorber effect of UB_2, to its greater uranium density, and to its greater thermal conductivity.

An approximate core-scale simulation would be used to determine the optimal isotopic composition of the fuel to reach a given goal in terms of extension in the refuelling interval: uranium enrichment of the matrix, uranium enrichment of the particles and boron isotopic composition in the particles. The microstructure of the composite would not be considered in such a simulation, which – given the scale of the core relative to the particles – would instead rely on a smeared composition of the composite pellet. The core-scale simulations would then return the optimal loading fraction and isotope composition for the UB_2 particles.

The data would then be used to inform a simplified pellet-scale, coupled thermal-neutronic model, requiring knowledge of the neutronic properties of UB_2 and of some of its physical properties – namely, its heat capacity, its thermal conductivity and its coefficient of thermal expansion. The pellet-scale simulations would return the optimal size and shape of the particles for a given loading fraction. Multimodal size distributions should be considered as well.

The currently known properties of UB_2 are its thermodynamic functions and heat capacity [124], its thermal conductivity and its technical coefficient of thermal expansion [43], alongside with some of its mechanical properties (bulk, shear and Young's moduli [43]). The available data would allow to simulate the neutronic performance of the composite concept in BOL conditions, as has been done for UN-UO_2 composites [32]. While no data are available regarding the variation in the physical properties of UB_2 as a function of burnup, a sensitivity analysis could be carried out with respect to the unknown parameters – most crucially, the mechanical resistance of the interface layers, the dimensional change in UB upon irradiation, the alteration of its thermal conductivity, and the quality of the thermal contact between the guest particles and the host matrix. Such an analysis would allow to identify any critical flaws in the concept and would return indicative goals for the composite's characteristics in order to direct the manufacturing work, with the most desirable outputs being the optimal size, shape, and volume fraction of the particles.

It is possible that particle geometries with a high aspect ratio (e.g. rods, whiskers, platelets) may perform better than spheroids in such simulations, especially in terms of improving the thermal conductivity [238]. Nevertheless, spheroids possess a number of other advantages: significant experience in the preparation and handling of spheroidal fuel kernels (e.g. for TRISO fuel [239]); excellent flowability, facilitating handling [240]; low surface-to-volume ratio, leading to reduced chemical reactivity.

7.1.2. Advanced modelling and integration of data from experiments and atomic-scale simulations

It must be noted that comprehensive models are extremely complex and computationally demanding and simulating *ab initio* a wide range of conditions may be far from optimal and introduce significant uncertainty in the results. Furthermore, owing to the greater geometrical complexity of the composite, even more computationally expensive 3-dimensional methods may be required to describe its behaviour more accurately.

The simulation of phenomena such as fuel failure, fuel fragmentation, and fission gas release in particular is as critical to fuel performance as is difficult to simulate accurately and requires experimental data for accurate benchmarking [241], stressing the need for the manufacturing and analysis tracks to inform the simulations.

Data on the still largely undocumented and not easily measured effects of burnup on the properties of UB_2 (e.g. volume change, thermal properties, retention of fission products) may also be supplemented by atomic-scale simulations and by correlation with the behaviour of known fuels.

7.1.3. Modelling the front- and back-end of the fuel cycle

As more experimental data are added, simulations should be aimed towards understanding the sensitivity of the performance of the composite pellets towards variance in the manufacturing process. Deviations in the size and shape of the particles, in their loading fraction, and in the homogeneity with which the particles are dispersed, should be taken into account to assess which fluctuations from the ideal parameters may be tolerated. The information would set targets for the quality assurance and quality control procedures which should be used in the manufacture of the fuel.

Finally, the simulations should address the post-irradiation performance of the spent fuel as well. The higher burn-up and the higher thermal conductivity are expected to alter its thermal and radiological profile, likely leading to different optimal handling procedures and disposal strategies when compared to the current fuels. In fact, while the radiogenic heat per unit of mass of irradiated

fuel (and therefore the difficulties in handling and storing the fuel) increases with burn-up, the increased burnup may lead to a smaller overall cost of the final disposal per unit of electricity generated if an adequate cooling time in monitored conditions is allowed prior to their transfer in a geological repository [7].

7.2. Fuel analysis and testing

The fuel analysis and testing track is instrumental in informing the fuel performance simulations described in Section 7.1.

7.2.1. Experiments on powders and sintered shapes of UB_2

Produced UB_2 powders may be analysed directly or sintered into specimens of the desired shape and bulk density in order to collect data on their thermal, mechanical, and chemical behaviour.

The chemical compatibility between UB_2 and other materials should be evaluated to select the best materials to be used as coatings for the UB_2 particles and in the industrial handling and processing of UB_2, especially at high temperatures. The properties of any diffusion interlayer forming at the interface between UB_2 and candidate coating materials should be studied extensively to determine their effect on the fuel performance.

Knowledge of the compatibility of UB_2 with fluids is necessary not only to properly evaluate its in-reactor safety performance, but also to illustrate which methods may be suitable for its handling and processing (e.g. wet granulation processes for the production of kernels, which may use water or may require less corrosive liquids), for the recycling of fuel which did not meet factory specifications and possibly for spent fuel reprocessing.
While the compatibility of UB_2 with dry steam [242] and with air (Section 6.3) has been investigated, no studies exist on its compatibility with liquid water, especially in the conditions that may be found in a LWR. With B_2O_3 being a key component in the passivating layer that UB_2 forms and at the same time being soluble in water, it may be conjectured that any protective effect that it may exert on the underlying material would be greatly reduced during corrosion by liquid water, especially if compounded by erosion in flowing conditions. The reactor coolant conditions may be simulated in an autoclave, with analogous experiments having been performed on UN-UO_2 composites [243].

The aqueous oxidation tests should also explore the effect of oxygen dissolved in water (also relevant to see which oxygen concentrations may be tolerated by UB_2 slurries during industrial handling), as well as the effect of oxidizers deriving from the radiolysis of water [244].

While some predictions have been formulated in Chapter 6, the chemical compatibility of UB_2 with fission products and the effects of irradiation must be assessed directly as part of the fuel licensing process.

Examination of UB_2 after the irradiation in a research reactor would naturally be the most direct answer to the research needs; however, the preliminary analysis of UB_2 samples doped with irradiation products surrogates (in abundances defined by the neutronic simulations) would be a necessary step in defining the safety case for the very in-pile testing of UB_2. Furthermore, the results of such a set of experiments may provide useful reference materials for the validation of atomic-scale simulations on the effects of burnup.

The samples containing boride-forming irradiation products may be prepared by modifying the borocarbothermic synthesis of UB_2, as illustrated in the case of ZrB_2 in Section 6.6, while ion implantation may be an especially valuable technique to study the combined effect of radiation damage and of the inclusion of gaseous irradiation products such as He and Xe [245] in the microstructure of UB_2 on its properties. Furthermore, the effect of microstructural features (in particular ones representative of the high-burnup structure observed in UO_2 [246]) may be reproduced by advanced sintering and manufacturing techniques, such as Spark Plasma Sintering [247].

7.2.2. Analysis of the UB_2 particles

The analysis track should also extensively characterise the UB_2 particles, as their mechanical and chemical behaviour may be substantially different from that of bulk samples of UB_2 owing to a combination of microstructure and impurities specific to their production process,

The crush strength of the sintered ceramic kernels should be evaluated to establish handling procedures and to determine the maximum pressure to which they may be safely subjected during

the manufacture of the fuel pellet which is expected to contain them, thus informing the fuel manufacturing track. Electron microscopy and X-ray tomography are expected to provide extremely relevant data in the investigation [248].

At this stage, the effectiveness of the coating should be evaluated as well, determining the minimum thickness with which it provides sufficient chemical protection and the optimal process for its application.

7.2.3. Analysis and testing of the composite fuel pellet and of its manufacturing process

Once composite fuel pellets have been prepared, their properties may be tested out-of-pile to validate and inform the thermo-mechanical simulations. The effect of thermal cycling at rates analogous to those experienced in reactor conditions is of particular interest, as it may lead to the formation of cracks, which would be detrimental to the quality of the thermal contact at the composite interface.

The bulk thermal conductivity of the composite pellets may be measured via Laser Flash Analysis (LFA), while X-ray tomography may be used to determine the homogeneity in the dispersion of spheres and the formation of cracks [249].

Finally, in-pile testing and post-irradiation examination (PIE) are expected to be the final steps for the validation of the fuel performance codes, with PIE allowing to determine the spatial distribution of irradiation products, the ratio of fission gas release, and the morphology and microstructure of the fuel [250].

Quality assurance and quality control procedures are also tested and validated, potentially providing input towards slight redesigns of the fuel concept to improve their effectiveness.

7.3. Fuel manufacturing

The first step in the manufacturing work – which will supply materials for analysis and testing throughout the development process – is the investigation and optimisation of industrially scalable

pathways for the preparation of UB_2. Key requirements for the synthesis procedure are safety, scalability, minimal loss of reactants (especially if valuable isotopically separated boron is used), minimal generation of waste, robustness, and product purity and homogeneity.

The subsequent laboratory-scale manufacturing of the composite fuel requires the study, the optimization and possibly the integration of several processes – namely the preparation of UB_2, its shaping and sintering into particles, the coating of the particles and their inclusion in a UO_2 matrix. Scrap recycling procedures should be established as well.

Owing to their similar properties (such as their chemical reactivity and thermal conductivity), ZrB_2 may be employed as a non-radioactive surrogate of UB_2 to screen and test manufacturing techniques before radioactive materials are used, facilitating the early research work by reducing radiological burdens, cost of materials and waste disposal, and regulatory oversight. Furthermore, UO_2-ZrB_2 composites may be ATF candidates in their own right, owing to the burnable absorber capabilities and to the high thermal conductivity of ZrB_2. [18].

7.3.1. Optimisation of the preparation of UB_2 and evaluation of its industrial scale-up

The development of industrially viable routes for UB_2 is crucial to its success as a fuel material. Key requirements for the synthesis procedure: safety, scalability, minimal loss of valuable reactants (with special attention to valuable and volatile isotopically separated boron), minimal generation of waste, robustness and product homogeneity.

If isotopically separated boron is to be used, integration of the synthesis process with the isotope separation process must also be considered. Isotopically separated boron may be obtained from ion exchange chromatography of borate anions (preferably coming from boric acid) [81] or via processes based on the distillation or the membrane diffusion of boron trifluoride or of its adducts with organic ethers [251]. The most readily available forms of isotopically separated boron are boron trifluoride (BF_3) and boric acid (H_3BO_3), both of which may be readily converted into boric anhydride (B_2O_3). Boron carbide (B_4C) may be prepared by the high-temperature reaction between B_2O_3 and carbon [134].

It is also worth noting that boron isotope separation may occur spontaneously in nature, with processes akin to its chromatographic separation. Depending on the pathway that led to the formation of natural boron deposits, they may present deviations from the isotopic mean in favour of either ^{10}B or ^{11}B [78]. This should be considered when sourcing the boron raw material, depending on the intended application.

The handling properties of the UB_2 powders (in particular their flowability and their propensity to caking) depend on their morphology and thus from the manufacturing process. The handling properties of the final product should be considered when optimizing the manufacturing process. Furthermore, the possibility of integrating the synthesis of UB_2 with the subsequent steps of the preparation of the composite should be explored as well.

The current method for the borocarbothermic synthesis of UB_2 may be optimized by Simultaneous Thermal Analysis (STA) of the reaction system coupled to mass spectrometry (MS). Comprising Thermo-Gravimetric Analysis (TGA) and Differential Scanning Calorimetry (DSC), the STA would allow to determine the mass and energy balance of the reaction system as a function of time and temperature, while mass spectrometry (MS) would allow to discern which chemical species are being released (e.g., CO, B_2O_3, B_2O_2).

The data provided by STA-MS would allow to identify the onset and the end point of the reaction and to determine the conditions in which the atom economy of boron is optimal. The data would also allow to correlate pre-processing of the reactants (e.g., mixing, pelletising, pre-shaping in particles) to the reaction kinetics, for optimal process integration.

Data on the kinetics of the reaction are especially useful to maintain the reaction time and temperature to a minimum in batch processing. A low synthesis temperature would be highly desirable in an industrial setting, given its manifold effect on process costs: lower temperature requirements result in decreased energy consumption, lower equipment wear and complexity, and in a reduced rate of volatilization of valuable boron from the reaction system.

7.3.2. Manufacture of UB_2 and ZrB_2 kernels

Kernels of ceramic materials can be obtained from liquid suspensions or solutions of the ceramics themselves or of their chemical precursors, with the concept being to lock the shape of the carrier liquid into loaded gel beads or aggregated particles which can be then converted into ceramic kernels. Several possible methods are discussed below.

7.3.2.1. Droplet gelation

In a droplet gelation process, the spherical shape of a droplet falling into a gelation bath is retained by cross-linking of chemical species contained in the droplet as they react with substances contained in the gelation bath.

Oxide ceramics in aqueous suspensions may be obtained by the formation of gelatinous metal oxide networks upon changes in pH. Such a process has been used to prepare UO_2 kernels from the gelation of acidic droplets of uranyl nitrate into a basic gelation bath containing ammonia [252].
Non-oxide ceramics such as ZrB_2 and UB_2 cannot exploit a similar chemistry and must therefore rely on other gelation agents such as polymers. Several polyanionic polymers (e.g., poly-(acrylic acid) and alginic acid) can be crosslinked by divalent cations. A good example of this technique is the crosslinking aqueous droplets containing sodium alginate in a bath of aqueous calcium chloride [253].

Falling droplets may be deformed by impact with the gelation bath. To contrast this phenomenon, they may be pre-emptively hardened by letting them fall in an atmosphere containing vapours of a suitable crosslinker (as in the case of ammonia vapours for the uranyl gelation route [252]) or a mist of the cross-linking solution. The gel beads containing the ceramic can then be dried and sintered to obtain fuel kernels.

The chemistry of the crosslinking system must be carefully evaluated, since any polymers and crosslinkers that are retained in the final shape will be present during the sintering phase. Organic polymers can be treated as sources of carbon for the purposes of sintering, with most of them undergoing full pyrolysis into volatile organic molecules and a solid carbonaceous residue in the temperature range 400-600 °C [254].

The crosslinking cations and their counterions may also play a part in sintering. Halides may react with the underlying material to form volatile species, which may in turn lead to coarsening of the material as opposed to sintering. Furthermore, if chloride salts are used as crosslinkers, the residual chlorine may act as a parasitic neutron absorber with difficult to predict concentrations.

Reducing the number of elements in the sintering system is an effective way to reduce the complexity of its chemistry. If organic anionic polymers are used, salts of uranium or zirconium cations with volatile or organic anions may be used to good effect. Examples include zirconium acetate $Zr(CH_3COO)_4$, zirconyl nitrate $ZrO(NO_3)_2$, uranyl acetate $UO_2(CH_3COO)_2$ and uranyl nitrate $UO_2(NO_3)_2$.

Uranyl cations UO_2^{2+} have been demonstrated to cross-link poly-(acrylic acid) [255] while Zr^{4+} [256] and ZrO^{2+} [257] cations have been used to cross-link alginate. The poly-(vinyl alcohol)/boric acid system may also represent a promising solution [258]., also contributing to introduce a slight boron excess that may compensate the losses during sintering.

The droplet gelation process may also be used to obtain beads from a slurry containing all the reactants for the borocarbothermic synthesis of UB_2, which may then be heated to the appropriate temperature in a combined synthesis and sintering process to obtain directly UB_2 kernels. In this case, the gelation effect of uranium oxide networks may be exploited as well. This process has been applied to the preparation of ZrB_2 with good effect [259].

7.3.2.2. Freeze granulation

In freeze granulation, droplets of an aqueous ceramic suspension are sprayed into liquid nitrogen under stirring and are quickly frozen (with the process requiring a few milliseconds). The resulting frozen granules are recovered and subsequently freeze-dried under vacuum to sublimate ice and yield a dry granulated powder with spherical granules [260].

The technique could be used to produce sintered UB_2 kernels both from UB_2 powders and from suitable reactants in a combined synthesis-sintering procedure.

7.3.2.3. Spray drying

In spray drying, a suspension containing the desired ceramic material and a binder is sprayed through a nozzle in a drying environment, forming droplets. As the droplets fall, the fluid evaporates and leaves behind agglomerates of ceramic held together by the binder. The particles are then collected at the bottom of the drier [261].

An upward flow of gas may be used to promote drying and at the same to slow the descent of the particles, in order to prevent any deformation upon impact with the bottom of the container. A suitable liquid may be also used to provide a soft landing for the agglomerates.

As in the case of droplet gelation and freeze granulation, the technique could be used to produce sintered UB_2 kernels both from UB_2 powders and from suitable reactants in a combined synthesis-sintering procedure.

7.3.3. Coating of kernels

The coating method for spheres should aim to apply a homogeneous layer of minimally reactive material with the lowest thickness that guarantees safe performance. Coating methods should also be evaluated according to their compatibility with the underlying material.

Coatings would be more conveniently applied to already sintered kernels, since they would not add complexity to the kernel's sintering chemistry and there would not be size mismatch and potentially coating delamination arising from the densification of the underlying material.

Tungsten and its alloys with molybdenum are especially promising coating materials, owing to their high thermal and mechanical stability and to the possibility of forming stable boride interlayers with the underlying UB_2. Two concepts for the coating of UB_2 particles are discussed below.

7.3.3.1. Chemical vapour deposition in fluidized bed reactor

Chemical Vapour Deposition (CVD) has the advantage of equipment simplicity over Physical Vapour Deposition (PVD), while the usage of a fluidized bed reactor (FBR) has the advantage of affording a coating with high homogeneity.

CVD-FBR has been used successfully to coat TRISO kernels with silicon carbide [262] and UO_2 particles with tungsten [38]. In the latter case, tungsten hexachloride (WCl_6) was used at temperatures between 400 °C and 550 °C in a stream of hydrogen and argon[263]. It must be noted that the reaction produces hydrogen chloride, therefore requiring careful evaluation of the corrosion resistance of the equipment to be used. In fact, iron impurities of 2000 ppm were reported due to corrosion of the stainless-steel vessel used by Oxley *et al*. [27]. Furthermore, UB_2 may be less resistant than UO_2 to chlorine and hydrogen chloride due to the stability and volatility of boron and uranium halides (see Paragraph 6.5.7), making the use of WCl_6 potentially challenging. Tungsten hexafluoride WF_6 should be avoided for the same reasons.

CVD with tungsten hexacarbonyl $W(CO)_6$ in the presence of hydrogen may be considered for the coating of UB_2 owing to its lower decomposition temperature and to the absence of halogens that may react with UB_2 or with the equipment. However, obtaining homogeneous films of tungsten from $W(CO)_6$ at low temperatures proved challenging, with the coatings containing impurities of tungsten oxides and tungsten carbide [264]. Nevertheless, it is possible to reduce any residual tungsten oxide to tungsten metal using hydrogen at temperatures ranging between 500 and 900 °C [265], while the formation of tungsten carbide may be inhibited by tuning the process conditions.

It is also worth noting that molybdenum hexacarbonyl, having similar properties to tungsten hexacarbonyl, may be used alone or in conjunction with the latter to obtain respectively coatings composed of molybdenum or of molybdenum-tungsten alloys. In fact, the thermal decomposition of metal carbonyls (including molybdenum, nickel and chromium) on uranium metal surfaces [266] and on ceramic oxides [267] has been described. Organometallic compounds with more sophisticated ligands may be used as well for a finer control of the process [268].

Owing to the electrical conductivity of UB_2, it would be possible to combine CVD-FBR with the inductive heating of the sole UB_2 suspended particles, thereby enhancing the selectivity of the process and minimizing the amount of coating metal that is lost on the reactor's walls. Furthermore, depending on the excitation frequency, the alternating currents induced in the particles would be mostly confined to their surface by the skin effect of conductors, thereby localizing the heating closer to where it would be required for the CVD process [269]. The concept of inductively heated, conductive particles in a FBR has already been explored by heating beds of materials such as iron hollow balls [270] or particles of graphite agglomerated with paraffin wax [271].

7.3.3.2. Dip coating in solutions of refractory metal precursors

Metal-coated UB_2 particles may be obtained by dipping bare particles into a solution or a dispersion containing a precursor of the desired metal, letting it dry and converting the precursor left on the particle to its metal form. The thickness of the resulting metal layer depends on the amount of metallic precursor on the particle's surface, which in turn depends on its concentration and on the amount of solution that is retained on the surface, which in turn depends on the surface tension of the solution and on the shape and surface features of the underlying particle [272].

It is worth noting that the solution may not necessarily be an aqueous one, potentially allowing the use of organometallic precursors. Nevertheless, the usage of aqueous solutions may benefit the simplicity and therefore scalability and the economics of the process.

Ammonium paratungstate $(NH_4)_{10}(H_2W_{12}O_{42})$ is a water-soluble precursor of tungsten [273] which may be used in the coating manufacture. The ammonium tungstate film deposited on the dried particles would be converted into mixed tungsten oxides WO_x by thermal decomposition [274] and reduced to tungsten metal under a flow of hydrogen [265]. Ammonium salts of tungstic acids are chosen because tungsten oxide is left as the sole solid product of the decomposition, with ammonium cations being converted into volatile ammonia and nitrogen oxides (depending on the oxygen potential in the gas space).

Water-soluble molybdenum precursors such as ammonium heptamolybdate $(NH_4)_6(Mo_7O_{24})$ may be used to the same effect to introduce molybdenum in the coating.

7.3.4. Fabrication of composite pellets

The fabrication of the composite pellet involves the dispersion of the coated UB_2 particles inside the UO_2 matrix and the pressing and sintering of a pellet.

The homogeneity of sphere distribution inside the pellet may significantly affect its thermal and neutronic properties. Should an extremely regular distribution of UB_2 kernels be required, it may conceptually be achieved with the following method: UB_2 kernels may be pre-coated with UO_2 and suitable binders to obtain spheres of a desired size (which would depend on the goal loading

fraction of UB_2). During preparation of the green pellet such “masterbatch” spheres would approximately follow a close packed arrangement and the interstices between spheres may be filled with UO_2 powder, affording a regular distribution of UB_2 kernels in a UO_2 matrix.

7.3.5. Quality control and scrap recycling

Quality control of the UB_2 kernels and of the composite pellets may be carried out via X-ray tomography and by neutron activation.

Uncoated UB_2 kernels that do not meet the required specifications may be crushed, reshaped and re-sintered. Finished pellets that do not meet the required specifications may be recycled in their components by exploiting the different resistance to attack by nitric acid HNO_3 of the UO_2 matrix and of the coated kernels.

In fact, UO_2 is readily soluble in nitric acid, whereas tungsten requires hydrogen peroxide [275], a combination of HNO_3 and HF [276] or electrochemically assisted dissolution in alkaline solutions [277] to be dissolved. It would therefore be possible to recover the tungsten-coated kernels from the UO_2 matrix via attack with nitric acid and filtration. The coated kernels could then be reused or further processed (e.g., via removal of the coating and dissolution of UB_2).

8. Conclusions

The development and qualification of new materials for the nuclear industry is an effort broad and deep in terms of the disciplines involved, mirroring the complex and challenging environment which the materials themselves will have to face and the consistency and reliability with which they have to operate. The intricate interplay of nuclear, physical, and chemical phenomena generates an extremely stringent set of requirements in terms of materials properties, the fulfilment of which must be meticulously verified before any new technology can be implemented on a large scale.

Collaboration among specialists and among research institutions becomes then of paramount importance, allowing to share knowledge and equipment to address the research, development, and qualification questions in the most thorough and effective manner.

Admittedly, with finite resources and such a daunting path ahead towards implementation, many ideas and concepts end up never leaving the drawing boards, adding to the vast number of paper fuels and paper reactors. However, that mountain of paper is essential in inspiring nuclear scientists and engineers, fostering debate and fuelling their passion. Thus, while it is uncertain whether a UB_2-UO_2 composite fuel pellet or a W_2B_5 neutron shield will ever be made, it is possible that this thesis will live on in other ideas, or that it will provide for a useful review of data – or perhaps for an amusing read.

Appendix A: tables of thermodynamic coefficients

Table A.1 reports the coefficients A-L used to calculate the thermodynamic properties of substances, using equations 3.12 and 3.13, as described in Section 3.1. Where necessary, the values of the coefficients were converted to be numerically compatible with equations 3.12 and 3.13, e.g. by converting units of kcal/mol into kJ/mol.

Most substances only required coefficients A through J for an accurate description of their thermodynamic properties. However, the literature data reported for C [280] and for UO_2 [41] used different sets of coefficients to be input in equations 3.12 and 3.13, which are reported in Table A.2 and Table A.3, respectively.

Table A.1: thermodynamic coefficients used in the assessments, along with their literature sources.

Substance	A	B	C	D	E	F	J	Ref.
Al	31.750	0.000	0.000	0.000	0.000	-0.946	73.399	[278]
Al_2O_3	102.429	38.750	-15.911	2.628	-3.008	-1717.930	146.997	[278]
AlB_2	48.461	53.073	-27.482	11.852	-1.379	-44.208	79.138	[279]
B	10.186	29.244	-18.021	4.212	-0.551	-6.036	7.089	[278]
B_2H_6	-12.422	267.611	-152.261	33.159	0.300	35.099	146.512	[278]
B_2O_3	111.569	23.174	-10.322	1.533	3.540	-1290.900	188.018	[278]
B_4C	95.999	23.165	-0.410	0.081	-4.395	-107.200	111.333	[278]
BBr_3	128.030	0.000	0.000	0.000	0.000	-276.660	383.802	[278]
BF_3	21.286	130.301	-109.992	34.288	-0.073	-1147.102	245.438	[278]
BI_3	80.757	2.015	-0.543	0.046	-0.968	43.722	440.349	[278]
Br_2	38.527	-1.977	1.526	-0.198	-0.186	-12.034	291.486	[278]
C	27.067	0.458	0.000	0.000	-2.182	-17.316	18.719	[280]
CO	35.151	1.300	-0.206	0.014	-3.283	-127.838	231.712	[278]
Cr	18.465	5.478	7.904	-1.148	1.266	-2.677	48.093	[278]
Cr_2B	47.116	40.200	-2.213	1.917	1.981	-103.934	98.836	[281]
Cs	30.046	0.506	0.348	-0.099	0.197	-6.234	129.377	[278]
CsBr	52.930	0.000	0.000	0.000	0.000	-421.583	177.150	[282]
CsI	52.800	0.000	0.000	0.000	0.000	-362.334	186.950	[282]
Fe	23.974	8.368	0.000	0.000	0.000	0.268	62.063	[278]
Fe_2B	-1543.292	1868.045	-785.458	118.375	483.723	1302.271	-1112.116	[281]
H_2	33.066	-11.363	11.433	-2.773	-0.159	-9.981	172.708	[278]

H_2O	30.092	6.833	6.793	-2.534	0.082	-250.881	223.397	[278]
HF	30.117	-3.247	2.868	0.458	-0.025	-281.491	210.923	[278]
I_2	37.798	0.225	-0.913	1.035	-0.084	50.869	305.920	[278]
Mo	24.727	3.960	-1.271	1.153	-0.170	-8.111	56.434	[278]
Mo_2B	63.380	15.330	0.000	0.000	-0.075	-112.820	138.300	[200,283]
MoB	41.771	11.080	0.000	0.000	-0.542	-118.658	78.200	[200,284]
N_2	19.506	19.887	-8.599	1.370	0.528	-4.935	212.390	[278]
Nb	22.014	9.888	-5.649	1.760	0.022	-6.881	60.524	[278]
Nb_2O5	116.057	117.181	-71.763	15.308	-1.161	-1942.640	239.334	[278]
NbB_2	74.236	3.992	0.000	0.000	-2.458	-282.096	140.900	[200,285]
O_2	30.032	8.773	-3.988	0.788	-0.742	-11.325	236.166	[278]
RbBr	52.840	0.000	0.000	0.000	0.000	-410.336	173.960	[282]
RbI	53.180	0.000	0.000	0.000	0.000	-349.546	182.410	[282]
Si	27.196	0.000	0.000	0.000	0.000	40.362	77.372	[278]
SiC	46.902	5.846	-1.085	0.093	-3.449	-95.467	56.975	[278]
SiO_2	58.753	10.279	-0.131	0.025	0.026	-929.329	105.809	[278]
Ta	-43.871	73.021	-27.408	4.005	26.304	60.175	25.710	[278]
Ta_2O_5	131.976	80.027	-33.897	5.280	-1.626	-2094.125	271.026	[278]
TaB_2	65.582	12.410	0.000	0.000	1.792	-228.559	94.079	[200]
Ti	44.372	-44.092	31.706	0.052	0.036	-12.720	93.088	[278]
TiB_2	52.333	33.695	-7.909	0.804	-1.541	-301.684	73.493	[278]
TiO_2	67.298	18.709	-11.579	2.450	-1.485	-964.514	117.863	[278]
UB_2	66.860	30.946	-7.095	0.000	-1.861	-191.909	116.025	[124]
UB_4	101.068	55.782	10.682	0.000	-3.719	-279.353	152.910	[124]
UB_{12}	236.470	125.556	20.703	0.000	0.827	-460.238	350.348	[124]
UB_2O_6	29.266	506.320	-229.759	0.000	0.000	-2571.676	69.041	[168]
UBr_4	110.817	3.137	-0.302	0.000	-0.431	-640.206	582.900	[286]
UC	59.521	-0.229	3.891	0.000	-0.871	-117.753	126.799	[124]
UF_6	135.687	33.204	0.000	0.000	-1.342	-2195.011	523.300	[286,287]
UI_4	110.978	2.957	-0.255	0.000	-0.271	-339.109	631.100	[286]
UN	55.531	0.152	4.661	0.000	0.768	-308.375	133.719	[288]
U_3O_8	264.240	463.860	0.000	0.000	0.000	-3674.140	464.600	[166,167]
UO_3	86.170	24.984	0.000	0.000	1.092	-1243.679	199.300	[286]
U_3Si_2	140.500	25.820	0.000	0.000	0.000	-208.510	380.000	[48,289]
W_2B	68.054	9.640	0.000	0.000	-0.185	-86.628	170.700	[153,290]
W_2B_5	152.392	23.980	0.000	0.000	-4.366	-253.628	299.200	[153,290]

WB	48.334	4.892	0.000	0.000	-0.818	-81.066	107.100	[153,290]
WO_2	53.409	53.532	-39.012	11.120	-0.931	-610.805	95.573	[278]
WO_3	23.959	2.640	1.258	-0.255	-0.048	-7.433	60.543	[278]
Zr	29.017	-12.556	20.750	-5.914	-0.157	-8.792	75.973	[278]
ZrB_2	66.962	5.665	1.434	-0.152	-1.836	-349.003	104.801	[278]
ZrO_2	74.475	0.000	0.000	0.000	0.000	-1115.333	138.043	[278]

Table A.2: thermodynamic coefficients for carbon (C) used in the assessments.

Substance	A	B	E	F	G	M	N	P
C	27.067	0.458	-2.182	-17.13516	18.87199	-4.532	0.800	-0.073

Table A.3: thermodynamic coefficients for uranium dioxide (UO_2) used in the assessments.

Substance	A	B	C	D	E	F	J	L
UO_2	52.174	87.951	-84.211	31.542	-0.714	-1106.167	117.420	-2.633

References

1. OECD-NEA. State-of-the-Art Report on Light Water Reactor Accident-Tolerant Fuels. No.7317 (2018).
2. Kurata, M. Research and Development Methodology for Practical Use of Accident Tolerant Fuel in Light Water Reactors. *Nucl. Eng. Technol.* **48**, 26–32 (2016). DOI:10.1016/j.net.2015.12.004.
3. Lang, P. M. Improving the productivity of LWRs. *Nucl. Eng. Int.* **23**, 13–14 (1978).
4. Whitlock, J. J. & Lee, A. G. CANDU ® : Setting the Standard for Proliferation Resistance of Generation III and III+ Reactors. International conference on opportunities and challenges for water cooled reactors in the 21st century, IAEA-CN--164-5P07 1–8 (2009).
5. Burkett, J. S. Refuelling the AGR. *Nucl. Power* **6**, (1961).
6. Krayushkin, A. V. Xenon transients, initiated by on-power reactor refuelling in the RBMK reactor. *At. Ehnergiya* **98**, 412–414 (2005).
7. Xu, Z. Design strategies for optimizing high burnup fuel in pressurized water reactors. (Massachusets Institute of Technology, 2003).
8. Lovering, J. R., Yip, A. & Nordhaus, T. Historical construction costs of global nuclear power reactors. *Energy Policy* **91**, 371–382 (2016). DOI:10.1016/j.enpol.2016.01.011.
9. Rothwell, G. S. Economics of Nuclear Energy. in *Encyclopedia of Nuclear Energy* 304–316 (Elsevier, 2021). doi:10.1016/B978-0-12-819725-7.00039-8. DOI:10.1016/B978-0-12-819725-7.00039-8.
10. Szulecki, K. & Overland, I. Russian nuclear energy diplomacy and its implications for energy security in the context of the war in Ukraine. *Nat. Energy* **8**, 413–421 (2023). DOI:10.1038/s41560-023-01228-5.
11. Harding, P. Uranium enrichment. in *Uranium for Nuclear Power* 321–351 (Elsevier, 2016). doi:10.1016/B978-0-08-100307-7.00012-0. DOI:10.1016/B978-0-08-100307-7.00012-0.
12. Omland, E. & Andersen, H. T. Y. Price responses to demand shocks in the commodity market for Uranium. (Stavanger University, 2023).
13. Lovecký, M., Závorka, J., Jiřičková, J. & Škoda, R. Increasing efficiency of nuclear fuel using burnable absorbers. *Prog. Nucl. Energy* **118**, (2020). DOI:10.1016/j.pnucene.2019.103077.
14. Fadaei, A. H. Investigation of burnable poisons effects in reactor core design. *Ann. Nucl. Energy* **38**, 2238–2246 (2011). DOI:10.1016/j.anucene.2011.06.005.
15. Uchida, S., Asakura, Y. & Suzuki, H. Deposition of boron on fuel rod surface under sub-

cooled boiling conditions - An approach toward understanding AOA occurrence. *Nucl. Eng. Des.* **241**, 2398–2410 (2011). DOI:10.1016/j.nucengdes.2011.04.009.

16. Fiorini, G. L., Gautier, G. M. & Bergamaschi, Y. Feasibility Studies of a Soluble Boron-Free 900-MW(electric) PWR, Safety Systems: Consequences of the Partial or Total Elimination of Soluble Boron on Plant Safety and Plant Systems Architecture. *Nucl. Technol.* **127**, 239–258 (1999). DOI:10.13182/NT99-A2999.
17. Wagner, J. C. & Sanders, C. E. Investigation of the Effect of Fixed Absorbers on the Reactivity of PWR Spent Nuclear Fuel for Burnup Credit. *Nucl. Technol.* **139**, 91–126 (2002). DOI:10.13182/NT02-A3307.
18. Middleburgh, S., Hallstadius, L. & Puide, M. A sintered nuclear fuel pellet, a fuel rod, a fuel assembly, and a method of manufacturing a sintered nuclear fuel pellet. U.S. Patent Application No. 16/486,330. Assignee: Westinghouse Electric Sweden AB (2020).
19. Enica, A., Vrtiska, S. J. & Middleburgh, S. C. Annular nuclear fuel pellets with discrete burnable absorber pins. U.S. Patent Application No. 15/590,234. Assignee: Westinghouse Electric Co LLC (2018).
20. Talamo, A. Effects of the burnable poison heterogeneity on the long term control of excess of reactivity. *Ann. Nucl. Energy* **33**, 794–803 (2006). DOI:https://doi.org/10.1016/j.anucene.2006.04.009.
21. Burr, P. A., Kardoulaki, E., Holmes, R. & Middleburgh, S. C. Defect evolution in burnable absorber candidate material: Uranium diboride, UB_2. *J. Nucl. Mater.* **513**, 45–55 (2019). DOI:10.1016/J.JNUCMAT.2018.10.039.
22. Bolukbasi, M. J., Middleburgh, S. C., Dahlfors, M. & Lee, W. E. Performance and economic assessment of enriched gadolinia burnable absorbers. *Prog. Nucl. Energy* **137**, 103752 (2021). DOI:10.1016/J.PNUCENE.2021.103752.
23. Hirai, M. & Ishimoto, S. Thermal Diffusivities and Thermal Conductivities of UO_2-Gd_2O_3. *J. Nucl. Sci. Technol.* **28**, 995–1000 (1991). DOI:10.1080/18811248.1991.9731462.
24. Popov, S. G., Lysenko, V. A. & Proselkov, V. N. Thermodynamic simulation of phase equilibria in the UO_2-Gd_2O_3 system at high temperatures. *High Temp.* **50**, 221–224 (2012). DOI:10.1134/S0018151X12020137.
25. Qin, M. J. *et al.* Thermal conductivity variation in uranium dioxide with gadolinia additions. *J. Nucl. Mater.* **540**, 152258 (2020). DOI:10.1016/j.jnucmat.2020.152258.
26. Secker, J. R. & Erwin, R. D. ZrB_2: The optimum integral fuel burnable absorber for PWRs. *Trans. Am. Nucl. Soc.* 555–556 (1990).

27. Medvedev, P. Effect of diamond additive on the fission gas release in UO_2 fuel irradiated to 7.2 GWd/tHM. *Ann. Nucl. Energy* **139**, 107282 (2020). DOI:10.1016/j.anucene.2019.107282.

28. Chen, S. & Yuan, C. Neutronic study of UO_2-BeO fuel with various claddings. *Nucl. Mater. Energy* **22**, 100728 (2020). DOI:10.1016/j.nme.2020.100728.

29. Gauld, I. C. & Ryman, J. C. *Nuclide Importance to Criticality Safety, Decay Heating, and Source Terms Related to Transport and Interim Storage of High-Burnup LWR Fuel*. http://www.osti.gov/servlets/purl/799527/ (2000) doi:10.2172/799527. DOI:10.2172/799527.

30. Ferreira, R. A. N. & Lopes, J. A. M. Implementation of a fuel pellets density and open porosity measurement system by the xylol penetration-immersion method at CDTN. in *2007 International Nuclear Atlantic Conference-INAC 2007* (2007).

31. Porter, D. L., Chichester, H. J. M., Medvedev, P. G., Hayes, S. L. & Teague, M. C. Performance of low smeared density sodium-cooled fast reactor metal fuel. *J. Nucl. Mater.* **465**, 464–470 (2015). DOI:https://doi.org/10.1016/j.jnucmat.2015.06.014.

32. Brown, N. R., Aronson, A., Todosow, M., Brito, R. & McClellan, K. J. Neutronic performance of uranium nitride composite fuels in a PWR. *Nucl. Eng. Des.* **275**, 393–407 (2014). DOI:10.1016/j.nucengdes.2014.04.040.

33. Feng, B., Shwageraus, E., Forget, B. & Kazimi, M. S. Light Water Breeding with Nitride Fuel. *Prog. Nucl. Energy* **53**, 862–866 (2011). DOI:https://doi.org/10.1016/j.pnucene.2011.06.001.

34. Turner, J. *et al.* Synthesis of candidate advanced technology fuel: Uranium diboride (UB_2) via carbo/borothermic reduction of UO_2. *J. Nucl. Mater.* **540**, 152388 (2020). DOI:10.1016/J.JNUCMAT.2020.152388.

35. Bratton, R. N., Jessee, M. A., Wieselquist, W. A. & Ivanov, K. N. Rod Internal Pressure Distribution and Uncertainty Analysis Using FRAPCON. *Nucl. Technol.* **197**, 47–63 (2017). DOI:10.13182/NT16-75.

36. Jacques, P., Lefebvre, F. & Lemaignan, C. Deformation-corrosion interactions for Zr alloys during I-SCC crack initiation part I: Chemical contributions. *J. Nucl. Mater.* **264**, 239–248 (1999). DOI:10.1016/S0022-3115(98)00501-7.

37. Petrochenko, V., Toshinsky, G. & Komlev, O. Safety of Future NPPs Must Not Be in Conflict with Economics. *World J. Nucl. Sci. Technol.* **06**, 284–300 (2016). DOI:10.4236/wjnst.2016.64026.

38. Lim, J., Kim, H. & Park, Y. Review of the regulatory periodic inspection system from the

viewpoint of defense-in-depth in nuclear safety. *Nucl. Eng. Technol.* **50**, 997–1005 (2018). DOI:10.1016/j.net.2018.07.008.

39. Sato, I., Lemoine, F. & Struwe, D. Transient Fuel Behavior and Failure Condition in the CABRI-2 Experiments. *Nucl. Technol.* **145**, 115–137 (2004). DOI:10.13182/NT04-A3464.
40. Chakraborty, S. *et al.* Micro-structural study and Rietveld analysis of fast reactor fuels: U–Mo fuels. *J. Nucl. Mater.* **467**, 618–627 (2015). DOI:https://doi.org/10.1016/j.jnucmat.2015.09.055.
41. Fink, J. K. Thermophysical properties of uranium dioxide. *J. Nucl. Mater.* **279**, 1–18 (2000). DOI:10.1016/S0022-3115(99)00273-1.
42. Dancausse, J.-P. *et al.* Compression study of uranium borides UB_2, UB_4 and UB_{12} by synchrotron X-ray diffraction. *J. Alloys Compd.* **189**, 205–208 (1992). DOI:https://doi.org/10.1016/0925-8388(92)90708-H.
43. Kardoulaki, E. *et al.* Thermophysical and mechanical property assessment of UB_2 and UB_4 sintered via spark plasma sintering. *J. Alloys Compd.* **818**, 153216 (2020). DOI:https://doi.org/10.1016/j.jallcom.2019.153216.
44. Vigier, N. *et al.* New Data on the Structure of Uranium Monocarbide. *Chem. Mater.* **20**, 3199–3204 (2008). DOI:10.1021/cm8001783.
45. Szpunar, B. & Szpunar, J. A. Thermal Conductivity of Uranium Nitride and Carbide. *Int. J. Nucl. Energy* **2014**, 1–7 (2014). DOI:10.1155/2014/178360.
46. Léger, J. M. Chalcogenides and pnictides of cerium and uranium under high pressure. *Phys. B Condens. Matter* **190**, 84–91 (1993). DOI:https://doi.org/10.1016/0921-4526(93)90447-E.
47. Remschnig, K., Le Bihan, T., Noël, H. & Rogl, P. Structural chemistry and magnetic behavior of binary uranium silicides. *J. Solid State Chem.* **97**, 391–399 (1992). DOI:https://doi.org/10.1016/0022-4596(92)90048-Z.
48. White, J. T. *et al.* Thermophysical properties of U_3Si_2 to 1773K. *J. Nucl. Mater.* **464**, 275–280 (2015). DOI:https://doi.org/10.1016/j.jnucmat.2015.04.031.
49. Jain, D., Nuwad, J., Sudarsan, V. & Tyagi, A. K. Effect of structural phase transitions on high temperature thermal conductivity of nuclear-grade uranium. *J. Alloys Compd.* **831**, 154706 (2020). DOI:https://doi.org/10.1016/j.jallcom.2020.154706.
50. Martin, D. G. A re-appraisal of the thermal conductivity of UO_2 and mixed (U,Pu) oxide fuels. *J. Nucl. Mater.* **110**, 73–94 (1982). DOI:10.1016/0022-3115(82)90410-X.
51. Harding, J. H. & Martin, D. G. A recommendation for the thermal conductivity of UO_2. *J. Nucl. Mater.* **166**, 223–226 (1989). DOI:10.1016/0022-3115(89)90218-3.

52. Lucuta, P. G., Matzke, H. & Hastings, I. J. A pragmatic approach to modelling thermal conductivity of irradiated UO_2 fuel: Review and recommendations. *J. Nucl. Mater.* **232**, 166–180 (1996). DOI:10.1016/S0022-3115(96)00404-7.

53. Williams, W. S. High-Temperature Thermal Conductivity of Transition Metal Carbides and Nitrides. *J. Am. Ceram. Soc.* **49**, 156–159 (1966). DOI:10.1111/j.1151-2916.1966.tb15395.x.

54. Williams, W. S. The thermal conductivity of metallic ceramics. *JOM* **50**, 62–66 (1998). DOI:10.1007/s11837-998-0131-y.

55. Lee, C. B., Kim, D. H. & Jung, Y. H. Fission gas release and swelling model of metallic fast reactor fuel. *J. Nucl. Mater.* **288**, 29–42 (2001). DOI:10.1016/S0022-3115(00)00718-2.

56. Middleburgh, S. C., Bolukbasi, M. & Goddard, D. Enhancing economics with ATF. *Nuclear Engineering International* https://www.neimagazine.com/features/featureenhancing-economics-with-atf-8159379/ (2020).

57. Bragg-Sitton, S. M. *et al.* Metrics for the Technical Performance Evaluation of Light Water Reactor Accident-Tolerant Fuel. *Nucl. Technol.* **195**, 111–123 (2016). DOI:10.13182/NT15-149.

58. Shennan, J. V, Sterry, F. & DeNordwall, H. J. *The Irradiation Behaviour of Uranium Carbide/silicon Carbide Dispersed Fuels*. (1966).

59. Ebert, E. L. *et al.* Reprocessability of molybdenum and magnesia based inert matrix fuels. *Nukleonika* **60**, 871–878 (2015). DOI:10.1515/nuka-2015-0124.

60. Webb, J. A. & Charit, I. Analytical determination of thermal conductivity of W–UO_2 and W–UN CERMET nuclear fuels. *J. Nucl. Mater.* **427**, 87–94 (2012). DOI:10.1016/j.jnucmat.2012.04.020.

61. Raftery, A. M. *et al.* Fabrication of UN-Mo CERMET Nuclear Fuel Using Advanced Manufacturing Techniques. *Nucl. Technol.* **207**, 815–824 (2021). DOI:10.1080/00295450.2020.1823187.

62. Slifka, A. J., Filla, B. J. & Phelps, J. M. Thermal conductivity of magnesium oxide from absolute, steady-state measurements. *J. Res. Natl. Inst. Stand. Technol.* **103**, 357 (1998). DOI:10.6028/jres.103.021.

63. Joshi, R. P., Neudeck, P. G. & Fazi, C. Analysis of the temperature dependent thermal conductivity of silicon carbide for high temperature applications. *J. Appl. Phys.* **88**, 265–269 (2000). DOI:10.1063/1.373651.

64. Hust, J. G. & Giarratano, P. J. *Thermal Conductivity and Electrical Resistivity Standard Reference Materials: Tungsten SRM's 730 and 799, from 4 to 3000 K*.

https://www.nist.gov/system/files/documents/srm/SP260-52.PDF (1975).

65. Lindemann, A. & Blumm, J. *Measurement of the thermophysical properties of pure molybdenum*. (Netzsch, 2009).

66. Lee, Y.-W., Joung, C. Y., Kim, S. H. & Lee, S.-C. Inert matrix fuel — A new challenge for material technology in the nuclear fuel cycle. *Met. Mater. Int.* **7**, 159–164 (2001). DOI:10.1007/BF03026954.

67. Porta, J. & Puill, A. U-Free Pu Fuels for LWRs–The CEA/DRN Strategy. *Adv. React.* 169 (1998).

68. Chabert, C., Coulon-Picard, E. & Pelletier, M. Neutronics performances study of silicon carbide as an inert matrix to achieve very high burn-up for light water reactor fuels. ICAPP 2007 - International congress on advances in nuclear power plants. The nuclear renaissance at work, Nice Acropolis (France). INIS-FR-08-0656 (2007).

69. Costa, D. R. *et al.* UN microspheres embedded in UO_2 matrix: An innovative accident tolerant fuel. *J. Nucl. Mater.* **540**, 152355 (2020). DOI:10.1016/j.jnucmat.2020.152355.

70. Gong, B. *et al.* U_3Si_2 and UO_2 composites densified by spark plasma sintering for accident-tolerant fuels. *J. Nucl. Mater.* **534**, 152147 (2020). DOI:10.1016/j.jnucmat.2020.152147.

71. Costa, D. R. *et al.* Oxidation of UN/U_2N_3-UO_2 composites: an evaluation of UO_2 as an oxidation barrier for the nitride phases. *J. Nucl. Mater.* **544**, 152700 (2021). DOI:10.1016/J.JNUCMAT.2020.152700.

72. Pietrak, K. & Wiśniewski, T. S. A review of models for effective thermal conductivity of composite materials. *J. Power Technol.* **95**, (2015).

73. Veyret, D., Cioulachtjian, S., Tadrist, L. & Pantaloni, J. Effective thermal conductivity of a composite material: A numerical approach. *J. Heat Transfer* **115**, 866–871 (1993). DOI:10.1115/1.2911381.

74. Eucken, A. Allgemeine Gesetzmäßigkeiten für das Wärmeleitvermögen verschiedener Stoffarten und Aggregatzustände. *Forsch. auf dem Gebiete des Ingenieurwesens* **11**, 6–20 (1940). DOI:10.1007/BF02584103.

75. Baron, D. D. & Hallstadius, L. Fuel Performance of Light Water Reactors (Uranium Oxide and MOX). in *Comprehensive Nuclear Materials* 481–514 (Elsevier, 2012). doi:10.1016/B978-0-08-056033-5.00040-9. DOI:10.1016/B978-0-08-056033-5.00040-9.

76. Miller, J. V. *Estimating thermal conductivity of cermet fuel materials for nuclear reactor application - NASA-TN-D-3898*. (1967).

77. Medvedev, P. G. & Mariani, R. D. Conductive inserts to reduce nuclear fuel temperature. *J.*

Nucl. Mater. **531**, 151966 (2020). DOI:10.1016/j.jnucmat.2019.151966.

78. Barth, S. Boron isotope variations in nature: a synthesis. *Geol. Rundschau* **82**, 640–651 (1993). DOI:10.1007/BF00191491.
79. OECD-NEA. JEFF 3.2 library. https://www.oecd-nea.org/dbdata/jeff/ (2014).
80. Korea Atomic Research Institute. Nuclear Data Center At KAERI. https://atom.kaeri.re.kr/nuchart/.
81. Oi, T., Shimazaki, H., Ishii, R. & Hosoe, M. Boron Isotope Fractionation in Liquid Chromatography with Boron-Specific Resins as Column Packing Material. *Sep. Sci. Technol.* **32**, 1821–1834 (1997). DOI:10.1080/01496399708000739.
82. Okamoto, H. B−U (Boron-Uranium). *J. Phase Equilibria Diffus.* **27**, 304–304 (2006). DOI:10.1361/154770306X109962.
83. Martel, L. *et al.* Insight into the crystal structures and physical properties of the uranium borides $UB_{1.78\pm0.02}$, $UB_{3.61\pm0.041}$ and $UB_{11.19\pm0.13}$. *Minerals* **12**, 29 (2022). DOI:10.3390/MIN12010029/S1.
84. Kardoulaki, E. *et al.* Fabrication and thermophysical properties of UO_2-UB_2 and UO_2-UB_4 composites sintered via spark plasma sintering. *J. Nucl. Mater.* **544**, 152690 (2021). DOI:10.1016/j.jnucmat.2020.152690.
85. Middleburgh, S. C., Parfitt, D. C., Blair, P. R. & Grimes, R. W. Atomic Scale Modeling of Point Defects in Zirconium Diboride. *J. Am. Ceram. Soc.* **94**, 2225–2229 (2011). DOI:https://doi.org/10.1111/j.1551-2916.2010.04360.x.
86. Gosset, D., Kryger, B., Bonal, J. P., Verdeau, C. & Froment, K. Evolution of thermo-physical properties and annealing of fast neutron irradiated boron carbide. *J. Nucl. Mater.* **500**, 166–175 (2018). DOI:10.1016/j.jnucmat.2017.11.027.
87. Howlett, B. W. A note on the uranium-boron alloy system. *J. Inst. Met.* **88**, (1959).
88. Troć, R., Wawryk, R., Pikul, A. & Shitsevalova, N. Physical properties of cage-like compound UB_{12}. *Philos. Mag.* **95**, 2343–2363 (2015). DOI:10.1080/14786435.2015.1054916.
89. Baris, M., Simsek, T., Simsek, T., Ozcan, S. & Kalkan, B. High purity synthesis of ZrB_2 by a combined ball milling and carbothermal method: Structural and magnetic properties. *Adv. Powder Technol.* **29**, 2440–2446 (2018). DOI:10.1016/j.apt.2018.06.024.
90. Fahrenholtz, W. G., Hilmas, G. E., Talmy, I. G. & Zaykoski, J. A. Refractory Diborides of Zirconium and Hafnium. *J. Am. Ceram. Soc.* **90**, 1347–1364 (2007). DOI:10.1111/j.1551-2916.2007.01583.x.

91. Lonergan, J. M., Fahrenholtz, W. G. & Hilmas, G. E. Zirconium Diboride with High Thermal Conductivity. *J. Am. Ceram. Soc.* **97**, 1689–1691 (2014). DOI:10.1111/jace.12950.
92. Domaszek, G. R., Parish, T. A. & Schlapper, G. A. Potential Applications of Boron-11 in Fusion Reactors. *Fusion Technol.* **15**, 465–468 (1989). DOI:10.13182/FST89-A39743.
93. Le Guyadec, F. *et al.* Pyrophoric behaviour of uranium hydride and uranium powders. *Journal of Nuclear Materials* vol. 396 294–302 (2010). DOI:10.1016/j.jnucmat.2009.11.007.
94. Lupinetti, A. J., Fife, J. L., Garcia, E., Dorhout, P. K. & Abney, K. D. Low-Temperature Synthesis of Uranium Tetraboride by Solid-State Metathesis Reactions. *Inorg. Chem.* **41**, 2316–2318 (2002). DOI:10.1021/ic015607a.
95. Schlesinger, H. I. & Brown, H. C. Uranium (IV) Borohydride. *J. Am. Chem. Soc.* **75**, 219–221 (1953). DOI:10.1021/ja01097a058.
96. Erickson, K. A., Scott, B. L. & Kiplinger, J. L. Ca(BH4)2 as a simple tool for the preparation of thorium and uranium metallocene borohydride complexes: First synthesis and crystal structure of $(C_5Me_5)_2Th(\eta^3\text{-}H_3BH)_2$. *Inorg. Chem. Commun.* **77**, 44–46 (2017). DOI:10.1016/j.inoche.2017.01.019.
97. Peshev, P., Bliznakov, G. & Leyarovska, L. On the preparation of some chromium, molybdenum and tungsten borides. *J. Less Common Met.* **13**, 241–247 (1967). DOI:10.1016/0022-5088(67)90188-9.
98. Cordova, S. & Shafirovich, E. Toward a better conversion in magnesiothermic SHS of zirconium diboride. *J. Mater. Sci.* **53**, 13600–13616 (2018). DOI:10.1007/s10853-018-2460-8.
99. Baroch, C. T. & Evans, T. E. Production of Zirconium Diboride from Zirconia and Boron Carbide. *JOM* **7**, 908–911 (1955). DOI:10.1007/BF03377586.
100. Odintsov, V. V. & Paderno, Y. B. Physical properties of uranium dodecaboride. *Sov. At. Energy* **30**, 561–562 (1971). DOI:10.1007/BF01408771.
101. Guo, H. *et al.* Boro/carbothermal reduction synthesis of uranium tetraboride and its oxidation behavior in dry air. *J. Am. Ceram. Soc.* **102**, 1049–1056 (2019). DOI:10.1111/jace.15987.
102. Mondal, S. & Banthia, A. K. Low-temperature synthetic route for boron carbide. *J. Eur. Ceram. Soc.* **25**, 287–291 (2005). DOI:https://doi.org/10.1016/j.jeurceramsoc.2004.08.011.
103. Atkins, P. & de Paula, J. *Atkins' physical chemistry*. (Oxford university press, 2014).
104. Shomate, C. H. A method for evaluating and correlating thermodynamic da ta. *J. Phys. Chem.* **58**, 368–372 (1954).
105. Harvey, A. H. Accuracy of Approximations to the Poynting Correction for Ice and Liquid

Water. *J. Res. Natl. Inst. Stand. Technol.* **122**, 41 (2017). DOI:10.6028/jres.122.041.

106. Kresse, G. & Furthmüller, J. Efficiency of ab-initio total energy calculations for metals and semiconductors using a plane-wave basis set. *Comput. Mater. Sci.* **6**, 15–50 (1996). DOI:10.1016/0927-0256(96)00008-0.
107. Kresse, G. & Joubert, D. From ultrasoft pseudopotentials to the projector augmented-wave method. *Phys. Rev. B* **59**, 1758–1775 (1999). DOI:10.1103/PhysRevB.59.1758.
108. Togo, A. & Tanaka, I. First principles phonon calculations in materials science. *Scr. Mater.* **108**, 1–5 (2015). DOI:10.1016/J.SCRIPTAMAT.2015.07.021.
109. Blöchl, P. E. Projector augmented-wave method. *Phys. Rev. B* **50**, 17953–17979 (1994). DOI:10.1103/PhysRevB.50.17953.
110. Perdew, J. P., Burke, K. & Ernzerhof, M. Generalized Gradient Approximation Made Simple. *Phys. Rev. Lett.* **77**, 3865–3868 (1996). DOI:10.1103/PhysRevLett.77.3865.
111. Kratzer, P. & Neugebauer, J. The Basics of Electronic Structure Theory for Periodic Systems. *Front. Chem.* **7**, (2019). DOI:10.3389/fchem.2019.00106.
112. Jorgensen, J. J. & Hart, G. L. W. Effectiveness of smearing and tetrahedron methods: best practices in DFT codes. *Model. Simul. Mater. Sci. Eng.* **29**, 065014 (2021). DOI:10.1088/1361-651X/ac13ca.
113. Lawson, A. C., Olsen, C. E., Richardson Jnr, J. W., Mueller, M. H. & Lander, G. H. Structure of β-uranium. *Acta Crystallogr. Sect. B* **44**, 89–96 (1988).
114. Parakhonskiy, G., Dubrovinskaia, N., Bykova, E., Wirth, R. & Dubrovinsky, L. High pressure synthesis and investigation of single crystals of metastable boron phases. *High Press. Res.* **33**, 673–683 (2013). DOI:10.1080/08957959.2013.806500.
115. Ohkochi, T. *et al.* Observation of 5f electrons in the itinerant limit: Three-dimensional electronic structure of UB_2. *Phys. Rev. B* **78**, 165110 (2008). DOI:10.1103/PhysRevB.78.165110.
116. Lohr, L. L. Relativistically parameterized extended Hückel calculations. 13. Energy bands for uranium compounds UB_2, UB_4, UC, UBC, and UPt_3. *Int. J. Quantum Chem.* **40**, 121–130 (1991). DOI:10.1002/qua.560400815.
117. Buschow, K. H. J. Magnetic Properties of Borides. in *Boron and Refractory Borides* 494–515 (Springer Berlin Heidelberg, 1977). doi:10.1007/978-3-642-66620-9_26. DOI:10.1007/978-3-642-66620-9_26.
118. Yamamoto, E. *et al.* De Haas-van Alphen Effect and Energy Band Structure in UB_2. *J. Phys. Soc. Japan* **67**, 3171–3175 (1998). DOI:10.1143/JPSJ.67.3171.

119. Evitts, L. J. *et al.* Influence of boron isotope ratio on the thermal conductivity of uranium diboride (UB_2) and zirconium diboride (ZrB_2). *J. Nucl. Mater.* **528**, 151892 (2020). DOI:10.1016/j.jnucmat.2019.151892.

120. Kirchner-Hall, N. E., Zhao, W., Xiong, Y., Timrov, I. & Dabo, I. Extensive Benchmarking of DFT+U Calculations for Predicting Band Gaps. *Appl. Sci.* **11**, 2395 (2021). DOI:10.3390/app11052395.

121. Misra, P. *Physics of condensed matter*. (Academic Press, 2011).

122. Wei, B., Sun, Q., Li, C. & Hong, J. Phonon anharmonicity: a pertinent review of recent progress and perspective. *Sci. China Physics, Mech. Astron.* **64**, 117001 (2021). DOI:10.1007/s11433-021-1748-7.

123. Okhotnikov, K., Charpentier, T. & Cadars, S. Supercell program: a combinatorial structure-generation approach for the local-level modeling of atomic substitutions and partial occupancies in crystals. *J. Cheminform.* **8**, 17 (2016). DOI:10.1186/s13321-016-0129-3.

124. Chevalier, P. Y. & Fischer, E. Thermodynamic modelling of the C-U and B-U binary systems. *J. Nucl. Mater.* **288**, 100–129 (2001). DOI:10.1016/S0022-3115(00)00713-3.

125. Davis, M. E. & Davis, R. J. T. A.-T. T.-. Fundamentals of chemical reaction engineering. (2003) doi:LK - https://worldcat.org/title/880604539. DOI:LK - https://worldcat.org/title/880604539.

126. Cox, A. N. *Allen's astrophysical quantities*. (Springer, 2015).

127. Turner, J. *et al.* Synthesis of candidate advanced technology fuel: Uranium diboride (UB_2) via carbo/borothermic reduction of UO_2. *J. Nucl. Mater.* **540**, 152388 (2020). DOI:10.1016/j.jnucmat.2020.152388.

128. Cullity, B. D. & Stock, S. R. Elements of X-ray Diffraction, Third Edition. (2001).

129. Meyer, V. R. Measurement uncertainty. *J. Chromatogr. A* **1158**, 15–24 (2007). DOI:10.1016/j.chroma.2007.02.082.

130. Elorrieta, J. M., Bonales, L. J., Rodríguez-Villagra, N., Baonza, V. G. & Cobos, J. A detailed Raman and X-ray study of UO2+x oxides and related structure transitions. *Phys. Chem. Chem. Phys.* **18**, 28209–28216 (2016). DOI:10.1039/c6cp03800j.

131. Rousseau, G. *et al.* A detailed study of UO_2 to U_3O_8 oxidation phases and the associated rate-limiting steps. *J. Nucl. Mater.* **355**, 10–20 (2006). DOI:10.1016/J.JNUCMAT.2006.03.015.

132. Qiu, H. Y., Guo, W. M., Zou, J. & Zhang, G. J. ZrB_2 powders prepared by boro/carbothermal reduction of ZrO_2: The effects of carbon source and reaction atmosphere. *Powder Technol.* (2012) doi:10.1016/j.powtec.2011.11.002. DOI:10.1016/j.powtec.2011.11.002.

133. Larroque, J., Chipaux, R. & Beauvy, M. Synthese de composes d'actinides binaires et ternaires de grande purete a partir de leurs oxydes. *J. Less Common Met.* **121**, 487–496 (1986). DOI:10.1016/0022-5088(86)90567-9.

134. Jung, C. H., Lee, M. J. & Kim, C. J. Preparation of carbon-free B_4C powder from B_2O_3 oxide by carbothermal reduction process. *Mater. Lett.* **58**, 609–614 (2004). DOI:10.1016/S0167-577X(03)00579-2.

135. Aleksandrov, B. P., Gordon, E. B., Ivanov, A. V, Kotov, A. A. & Smirnov, V. E. Reduction of uranium hexafluoride to tetrafluoride by using the hydrogen atoms. *J. Phys. Conf. Ser.* **751**, 012012 (2016). DOI:10.1088/1742-6596/751/1/012012.

136. Hiroshi, T. & Akio, U. Process for conversion of UF_6 to UO_2. U.S. Patent Application No.4788048A (1988).

137. Solozhenko, V. L. & Kurakevych, O. O. Equilibrium p-T Phase Diagram of Boron: Experimental Study and Thermodynamic Analysis. *Sci. Rep.* **3**, 2351 (2013). DOI:10.1038/srep02351.

138. Mewes, J.-M. & Smits, O. R. Accurate elemental boiling points from first principles. *Phys. Chem. Chem. Phys.* **22**, 24041–24050 (2020). DOI:10.1039/D0CP02884C.

139. NIOSH Pocket Guide to Chemical Hazards - Boron Oxide. https://www.cdc.gov/niosh/npg/npgd0060.html (2019).

140. Xi, P. *et al.* Internal Explosion Performance of RDX@Nano-B Composite Explosives. *Nanomaterials* **13**, 412 (2023). DOI:10.3390/nano13030412.

141. NIOSH Pocket Guide to Chemical Hazards - Boron trifluoride. https://www.cdc.gov/niosh/npg/npgd0062.html (2019).

142. NIOSH Pocket Guide to Chemical Hazards - Diborane. https://www.cdc.gov/niosh/npg/npgd0183.html (2019).

143. U.S. Enrichment Corp. *Uranium hexafluoride: A manual of good handling practices. Revision 7*. http://www.osti.gov/servlets/purl/205924-LzIkaU/webviewable/ (1995) doi:10.2172/205924. DOI:10.2172/205924.

144. NIOSH Pocket Guide to Chemical Hazards - Uranium (soluble compounds, as U). https://www.cdc.gov/niosh/idlh/uranium.html.

145. Jang, H. *et al.* Synthetic diversity in the preparation of metallic uranium. *R. Soc. Open Sci.* **9**, (2022). DOI:10.1098/rsos.211870.

146. Nicol, W., Hernier, M., Hildebrant, D. & Glasser, D. The attainable region and process synthesis: reaction systems with external cooling and heating. *Chem. Eng. Sci.* **56**, 173–191

(2001). DOI:10.1016/S0009-2509(00)00196-2.

147. Gang, L., Chunmiao, Y., Peihong, Z. & Baozhi, C. Experiment-based fire and explosion risk analysis for powdered magnesium production methods. *J. Loss Prev. Process Ind.* **21**, 461–465 (2008). DOI:10.1016/j.jlp.2008.03.003.
148. Cahill, J. T. & Graeve, O. A. Hexaborides: a review of structure, synthesis and processing. *J. Mater. Res. Technol.* **8**, 6321–6335 (2019). DOI:10.1016/j.jmrt.2019.09.041.
149. Zhou, J. & Bai, P. A review on the methods of preparation of elemental boron. *Asia-Pacific J. Chem. Eng.* **10**, 325–338 (2015). DOI:10.1002/apj.1892.
150. Constantine, M. T., Weber, J. Q. & Youel, K. J. *Diborane Handbook.* https://ntrs.nasa.gov/api/citations/19700078681/downloads/19700078681.pdf (1971).
151. Morel, B. *et al.* Surface reactivity of uranium hexafluoride (UF_6). *Comptes Rendus Chim.* **21**, 782–790 (2018). DOI:10.1016/j.crci.2018.05.006.
152. Jacobson, N. S. & Myers, D. L. High-temperature vaporization of $B_2O_{3\ (l)}$ under reducing conditions. *J. Phys. Chem. B* **115**, 13253–13260 (2011). DOI:10.1021/jp206480d.
153. Duschanek, H. & Rogl, P. Critical assessment and thermodynamic calculation of the binary system boron-tungsten (B-W). *J. Phase Equilibria* **16**, 150–161 (1995). DOI:10.1007/BF02664852.
154. Zhao, C. *et al.* Unexpected stable phases of tungsten borides. *Phys. Chem. Chem. Phys.* **20**, 24665–24670 (2018). DOI:10.1039/C8CP04222E.
155. Kayhan, M. *et al.* Neutron diffraction and observation of superconductivity for tungsten borides, WB and W_2B_4. *Solid State Sci.* **14**, 1656–1659 (2012). DOI:10.1016/j.solidstatesciences.2012.05.036.
156. Setayandeh, S. S. *et al.* A DFT study to determine the structure and composition of ε-W_2B_{5-x}. *J. Alloys Compd.* **911**, 164962 (2022). DOI:10.1016/j.jallcom.2022.164962.
157. Hu, X. B., Zhu, Y. L., Sheng, N. C. & Ma, X. L. The Wyckoff positional order and polyhedral intergrowth in the M_3B_2- and M_5B_3-type boride precipitated in the Ni-based superalloys. *Sci. Rep.* **4**, 7367 (2014). DOI:10.1038/srep07367.
158. Pak, A. Y. *et al.* Efficient Synthesis of WB_{5-x} –WB_2 Powders with Selectivity for WB_{5-x} Content. *Inorg. Chem.* **61**, 6773–6784 (2022). DOI:10.1021/acs.inorgchem.1c03880.
159. Windsor, C. G. *et al.* Tungsten boride shields in a spherical tokamak fusion power plant. *Nucl. Fusion* **61**, 086018 (2021). DOI:10.1088/1741-4326/ac09ce.
160. Wang, Y., Li, Z.-B., Wang, K.-F. & Zhang, G.-H. Preparation of Monophasic Tungsten boride powder from Tungsten and boron carbide. *Ceram. Int.* **47**, 9543–9550 (2021).

DOI:10.1016/j.ceramint.2020.12.088.

161. Wriedt, H. A. The O-W (oxygen-tungsten) system. *Bull. Alloy Phase Diagrams* **10**, 368–384 (1989). DOI:10.1007/BF02877593.

162. Kostomarov, D. V., Bagdasarov, K. S., Kobzareva, S. A. & Antonov, E. V. Chemical transformations in the W-Al_2O_3 system under pressure P = 1 bar near the melting point of aluminum oxide. *Crystallogr. Reports* **55**, 153–157 (2010). DOI:10.1134/S1063774510010232.

163. Sonber, J. K. & Suri, A. K. Synthesis and consolidation of zirconium diboride: review. *Adv. Appl. Ceram.* **110**, 321–334 (2011). DOI:10.1179/1743676111Y.0000000008.

164. Mistarihi, Q. *et al.* The oxidation of uranium diboride in flowing air atmospheres. *J. Nucl. Mater.* **580**, 154417 (2023). DOI:10.1016/J.JNUCMAT.2023.154417.

165. Chase, M. W., Davies, C. A., Downey, J. R., Frurip, D. J. & McDonald, R. A. JANAF thermochemical tables. vol. 4 (1998).

166. Navrotsky, A., Shvareva, T., Guo, X. & Burns, P. C. Uranium - Thermodynamics of Uranium Minerals and Related Materials. in *Uranium - Cradle to Grave* (2013).

167. Hideaki, I., Hisashi, S. & Keiji, N. Lambda-type heat capacity anomalies in U_3O_8. *J. Nucl. Mater.* **64**, 66–70 (1977). DOI:10.1016/0022-3115(77)90009-5.

168. Chernorukov, N. G., Smirnova, N. N., Knyazev, A. V., Marochkina, M. N. & Ershova, A. V. The thermodynamic properties of uranyl metaborate. *Russ. J. Phys. Chem.* **80**, 1915–1919 (2006). DOI:10.1134/S0036024406120089.

169. Hoekstra, H. R. Uranyl Metaborate and Sodium Uranyl Borate. 320–330 (1967) doi:10.1021/ba-1967-0071.ch023. DOI:10.1021/ba-1967-0071.ch023.

170. Blackburn, P. E. Oxygen pressures over fast breeder reactor fuel (I) A model for $UO_{2\pm x}$. *J. Nucl. Mater.* **46**, 244–252 (1973). DOI:10.1016/0022-3115(73)90038-X.

171. Burianek, M. *et al.* High-pressure synthesis, long-term stability of single crystals of diboron trioxide, B_2O_3, and an empirical electronic polarizability of $^{[3]}B^{3+}$. *Phys. Chem. Miner.* **43**, 527–534 (2016). DOI:10.1007/S00269-016-0813-X/METRICS.

172. Desgranges, L., Baldinozzi, G., Rousseau, G., Nièpce, J. C. & Calvarin, G. Neutron diffraction study of the in situ oxidation of UO_2. *Inorg. Chem.* **48**, 7585–7592 (2009). DOI:10.1021/ic9000889.

173. Gasperin, M. Structure du borate d`uranium UB_2O_6. *Acta Crystallogr. Sect. C Cryst. Struct. Commun.* **43**, 2031–2033 (1987). DOI:10.1107/S0108270187089121.

174. McEachern, R. J. & Taylor, P. A review of the oxidation of uranium dioxide at temperatures

below 400 °C. *J. Nucl. Mater.* **254**, 87–121 (1998). DOI:10.1016/S0022-3115(97)00343-7.

175. Hildenbrand, D. L., Hall, W. F. & Potter, N. D. Thermodynamics of Vaporization of Lithium Oxide, Boric Oxide, and Lithium Metaborate. *J. Chem. Phys.* **39**, 296 (1963). DOI:10.1063/1.1734245.
176. Rogl, P., Bauer, J. & Debuigne, J. The ternary system uranium-boron-carbon. *J. Nucl. Mater.* **165**, 74–82 (1989). DOI:10.1016/0022-3115(89)90504-7.
177. Rogl, P. & Nowotny, H. Uran-haltige Komplexboride. *Monatshefte für Chemie* **106**, 381–387 (1975). DOI:10.1007/BF01150518.
178. Adorno, D. L. *et al. Compatibility Of U_3Si_2 Fuel With Zr, FeCrAl and SiC/SiC Based Cladding*. http://www.osti.gov/servlets/purl/1529825/ (2018) doi:10.2172/1529825. DOI:10.2172/1529825.
179. Leppänen, J., Pusa, M., Viitanen, T., Valtavirta, V. & Kaltiaisenaho, T. The Serpent Monte Carlo code: Status, development and applications in 2013. *Ann. Nucl. Energy* **82**, 142–150 (2015). DOI:10.1016/j.anucene.2014.08.024.
180. Grinik, E. U., Ogorodnikov, V. V. & Krainy, A. G. Fracturing of borides under neutron irradiation. *J. Nucl. Mater.* **233**–**237**, 1349–1354 (1996). DOI:10.1016/S0022-3115(96)00293-0.
181. Koyanagi, T. *et al.* Response of isotopically tailored titanium diboride to neutron irradiation. *J. Am. Ceram. Soc.* **102**, 85–89 (2019). DOI:10.1111/jace.16036.
182. Kleykamp, H. The chemical state of the fission products in oxide fuels. *J. Nucl. Mater.* **131**, 221–246 (1985). DOI:10.1016/0022-3115(85)90460-X.
183. Grimes, R. W. & Catlow, C. R. A. The stability of fission products in uranium dioxide. *Philos. Trans. R. Soc. London. Ser. A Phys. Eng. Sci.* **335**, 609–634 (1991). DOI:10.1098/rsta.1991.0062.
184. Wen, T. *et al.* Formation criterion for binary metal diboride solid solutions established through combinatorial methods. *J. Am. Ceram. Soc.* **103**, 3338–3348 (2020). DOI:10.1111/jace.16983.
185. Gild, J. *et al.* High-Entropy Metal Diborides: A New Class of High-Entropy Materials and a New Type of Ultrahigh Temperature Ceramics. *Sci. Rep.* **6**, 37946 (2016). DOI:10.1038/srep37946.
186. Albert, B. The Structure Chemistry of Boron-Rich Solids of the Alkali Metals. doi:10.1002/1099-0682(200008)2000:8. DOI:10.1002/1099-0682(200008)2000:8.
187. Kolmogorov, A. N. & Curtarolo, S. Theoretical study of metal borides stability. *Phys. Rev. B*

- *Condens. Matter Mater. Phys.* **74**, 224507 (2006). DOI:10.1103/PHYSREVB.74.224507/FIGURES/15/MEDIUM.

188. Chen, C.-H., Aizawa, T., Iyi, N., Sato, A. & Otani, S. Structural refinement and thermal expansion of hexaborides. *J. Alloys Compd.* **366**, L6–L8 (2004). DOI:10.1016/S0925-8388(03)00735-7.
189. Samsonov, G. V, Serebryakova, T. I. & Bolgar, A. S. Preparation and physico-chemical properties of strontium hexaboride. *Zhur. Neorg. Khim* **Vol: 6**, (1961).
190. Salvato, D. *et al.* Transmission electron microscopy study of a high burnup U-10Zr metallic fuel. *J. Nucl. Mater.* **570**, 153963 (2022). DOI:10.1016/j.jnucmat.2022.153963.
191. Wright, K. E., Harp, J. M. & Capriotti, L. Electron probe microanalysis of irradiated FUTURIX-FTA U-Pu-Zr alloy with added minor actinides. *J. Nucl. Mater.* **526**, (2019). DOI:10.1016/J.JNUCMAT.2019.151745.
192. Brunett, A. J., Bucknor, M. & Grabaskas, D. Toward a Mechanistic Source Term in Advanced Reactors: Characterization of Radionuclide Transport and Retention in a Sodium Cooled Fast Reactor. International Congress on Advances in Nuclear Power Plants (ICAPP '16), San Francisco (USA) (2016).
193. Kleykamp, H., Paschoal, J. O., Pejsa, R. & Thümmler, F. Composition and structure of fission product precipitates in irradiated oxide fuels: Correlation with phase studies in the Mo-Ru-Rh-Pd and BaO-UO_2-ZrO_2-MoO_2 Systems. *J. Nucl. Mater.* **130**, 426–433 (1985). DOI:10.1016/0022-3115(85)90329-0.
194. Pellegrini, K. L. *et al.* Chemical and Isotopic Characterization of Noble Metal Phase from Commercial UO_2 Fuel. *Anal. Chem.* **91**, 6522–6529 (2019). DOI:10.1021/acs.analchem.8b05549.
195. McClane, D. L., Fahrenholtz, W. G. & Hilmas, G. E. Thermal Properties of (Zr,TM)B_2 Solid Solutions with TM = Hf, Nb, W, Ti, and Y. *J. Am. Ceram. Soc.* **97**, 1552–1558 (2014). DOI:10.1111/jace.12893.
196. Manelis, R. M. *et al.* Vacuum-thermal preparation of yttrium and gadolinium borides, and some of their properties. *Sov. Powder Metall. Met. Ceram.* **5**, 904–909 (1966). DOI:10.1007/BF00775505.
197. Takagiwa, H. *et al.* Relationship between superconductivity and crystal structure in NbB_{2+x}. *Sci. Technol. Adv. Mater.* **7**, 22–25 (2006). DOI:10.1016/j.stam.2005.11.015.
198. Jossou, E. *et al.* First-principles study of defects and fission product behavior in uranium diboride. *J. Nucl. Mater.* **494**, 147–156 (2017). DOI:10.1016/J.JNUCMAT.2017.07.027.

199. Bolgar, A. S., Serbova, M. I., Serebryakova, T. I., Isaeva, L. P. & Fesenko, V. V. High-temperature enthalpy and heat capacity of borides of the niobium-boron system. *Sov. Powder Metall. Met. Ceram.* **22**, 207–211 (1983). DOI:10.1007/BF00793920.

200. Blinder, A. V. & Bolgar, A. S. Heat capacity and enthalpy of transition-metal borides in a broad range of temperatures. *Sov. Powder Metall. Met. Ceram.* **30**, 1053–1056 (1991). DOI:10.1007/BF00794439.

201. Trzebiatowski, W. & Rudzinski, J. The composition and structure of technetium nitride and technetium borides. *J. Less Common Met.* **6**, 244–245 (1964). DOI:10.1016/0022-5088(64)90106-7.

202. Frotscher, M., Senyshyn, A. & Albert, B. Neutron Diffraction at Metal Borides, Ru_2B_3 and Os_2B_3. *Zeitschrift für Anorg. und Allg. Chemie* **638**, 2078–2080 (2012). DOI:10.1002/zaac.201200350.

203. Frotscher, M., Hölzel, M. & Albert, B. Crystal Structures of the Metal Diborides ReB_2, RuB_2, and OsB_2 from Neutron Powder Diffraction. *Zeitschrift für Anorg. und Allg. Chemie* **636**, 1783–1786 (2010). DOI:10.1002/zaac.201000101.

204. Raghavan, V. Al-B-Rh (Aluminum-Boron-Rhodium). *J. Phase Equilibria Diffus.* **29**, 43–43 (2008). DOI:10.1007/s11669-007-9209-4.

205. Griffith, W. P., Robinson, S. D. & Swars, K. Palladium and Boron. in *Pd Palladium* 256–261 (Springer Berlin Heidelberg, 1989). doi:10.1007/978-3-662-09188-3_10. DOI:10.1007/978-3-662-09188-3_10.

206. Kleykamp, H. Thermodynamics of the uranium-platinum metals systems. *Pure Appl. Chem.* **63**, 1401–1408 (1991). DOI:10.1351/pac199163101401.

207. Benson, M. T. *et al.* Out-of-pile and postirradiated examination of lanthanide and lanthanide-palladium interactions for metallic fuel. *J. Nucl. Mater.* **544**, 152727 (2021). DOI:10.1016/j.jnucmat.2020.152727.

208. Obrowski, W. Die Struktur der Diboride von Gold und Silber. *Naturwissenschaften 1961 4811* **48**, 428–428 (1961). DOI:10.1007/BF00621674.

209. Muetterties, E. L. Notizen: Boron-Metal Interactions in Boride. *Zeitschrift für Naturforsch. B* **12**, 411–412 (1957). DOI:10.1515/znb-1957-0611.

210. Morrow, H. Cadmium and Cadmium Alloys. in *Kirk-Othmer Encyclopedia of Chemical Technology* (John Wiley & Sons, Inc., 2010). doi:10.1002/0471238961.0301041303011818.a01.pub3. DOI:10.1002/0471238961.0301041303011818.a01.pub3.

211. Akopov, G., Yeung, M. T. & Kaner, R. B. Rediscovering the Crystal Chemistry of Borides. *Adv. Mater.* **29**, 1604506 (2017). DOI:10.1002/adma.201604506.

212. Etourneau, J., Mercurio, J.-P. & Hagenmuller, P. Compounds Based on Octahedral B_6 Units: Hexaborides and Tetraborides. in *Boron and Refractory Borides* 115–138 (Springer Berlin Heidelberg, 1977). doi:10.1007/978-3-642-66620-9_10. DOI:10.1007/978-3-642-66620-9_10.

213. Otto, F., Yang, Y., Bei, H. & George, E. P. Relative effects of enthalpy and entropy on the phase stability of equiatomic high-entropy alloys. *Acta Mater.* **61**, 2628–2638 (2013). DOI:10.1016/j.actamat.2013.01.042.

214. Schlesinger, M. E. The Lesser-Known B-Ln (Boron-Lanthanide) Systems: B-Dy (Boron-Dysprosium), B-Ho (Boron-Holmium), B-Lu (Boron-Lutetium), B-Pr (Boron-Praseodymium), B-Tm (Boron-Thulium), and B-Yb (Boron-Ytterbium). *J. Phase Equilibria Diffus.* **19**, 49–55 (1998). DOI:10.1007/s11669-006-5004-x.

215. Spear, K. E. Rare Earth-Boron Phase Equilibria. in *Boron and Refractory Borides* 439–456 (Springer Berlin Heidelberg, 1977). doi:10.1007/978-3-642-66620-9_24. DOI:10.1007/978-3-642-66620-9_24.

216. Xie, Y. *et al.* Lanthanide migration and immobilization in metallic fuels. *Prog. Nucl. Energy* **109**, 233–238 (2018). DOI:10.1016/j.pnucene.2018.08.019.

217. Eick, H. A. Plutonium Borides. *Inorg. Chem.* **4**, 1237–1239 (1965). DOI:10.1021/ic50030a037.

218. Eick, H. A. & Mulford, R. N. R. Americium and neptunium borides. *J. Inorg. Nucl. Chem.* **31**, 371–375 (1969). DOI:10.1016/0022-1902(69)80480-X.

219. Chipaux, R., Larroque, J. & Beauvy, M. Studies of the neptunium-plutonium diboride system. *J. Less Common Met.* **153**, 1–7 (1989). DOI:10.1016/0022-5088(89)90526-2.

220. Zhao, J.-T., Dong, Z.-C., Vaughey, J. T., Ostenson, J. E. & Corbett, J. D. Synthesis, structures and properties of cubic R_3In and R_3InZ phases (R = Y, La; Z = B, C, N, O). *J. Alloys Compd.* **230**, 1–12 (1995). DOI:10.1016/0925-8388(95)01909-X.

221. Kwon, Y. U. & Corbett, J. D. Chemistry in polar intermetallic compounds. The interstitial chemistry of zirconium-tin (Zr_5Sn_3). *Chem. Mater.* **4**, 1348–1355 (1992). DOI:10.1021/cm00024a040.

222. Kluenter, W. & Jung, W. Die Zinn-Rhodiumboride $SnRh_3B_{1-x}$, Sn_4Rh_6B und $Sn_5Rh_6B_2$. *Zeitschrift fur Anorg. und Allg. Chemie* **622**, 2099–2106 (1996). DOI:10.1002/zaac.19966221218.

223. Bagnall, K. W., Brown, D., Jones, P. J. & Du Preez, J. G. H. 52. Iodo-complexes of thorium (IV) and uranium (IV). *J. Chem. Soc.* 350 (1965) doi:10.1039/jr9650000350. DOI:10.1039/jr9650000350.

224. Sidky, P. S. Iodine stress corrosion cracking of Zircaloy reactor cladding: Iodine chemistry (a review). *J. Nucl. Mater.* **256**, 1–17 (1998). DOI:10.1016/S0022-3115(98)00044-0.

225. Yamawaki, M., Yoneoka, T., Kaneko, H. & Konashi, K. Reactivity of cesium iodide vapor under irradiation. *J. Nucl. Mater.* **154**, 47–52 (1988). DOI:10.1016/0022-3115(88)90117-1.

226. Ustinov, O. A. *et al.* Tritium in Nitride Fuel of Fast Reactors. *At. Energy* **125**, 244–249 (2019). DOI:10.1007/s10512-019-00474-9.

227. Middleburgh, S. C., Parfitt, D. C., Blair, P. R. & Grimes, R. W. Atomic Scale Modeling of Point Defects in Zirconium Diboride. *J. Am. Ceram. Soc.* **94**, 2225–2229 (2011). DOI:10.1111/j.1551-2916.2010.04360.x.

228. Loukusa, H., Ikonen, T., Valtavirta, V. & Tulkki, V. Thermochemical modeling of nuclear fuel and the effects of oxygen potential buffers. *J. Nucl. Mater.* **481**, 101–110 (2016). DOI:10.1016/j.jnucmat.2016.09.014.

229. Holleck, H., Benesovsky, F., Laube, E. & Nowotny, H. Ein Beitrag zu hochschmelzenden Systemen. *Monatshefte für Chemie und verwandte Teile anderer Wissenschaften 1962 935* **93**, 1075–1079 (1962). DOI:10.1007/BF00905907.

230. Jossou, E. *et al.* First-principles study of defects and fission product behavior in uranium diboride. *J. Nucl. Mater.* **494**, 147–156 (2017). DOI:10.1016/J.JNUCMAT.2017.07.027.

231. Beckman, G. & Kiessling, R. Thermal Expansion Coefficients for Uranium Boride and β-Uranium Silicide. *Nature* **178**, 1341 (1956). DOI:10.1038/1781341a0.

232. Wang, K. & Reeber, R. R. Thermal defects and thermal expansion of ionic crystals at high temperatures. *Phys. Status Solidi* **146**, 621–627 (1994). DOI:10.1002/pssa.2211460207.

233. Paxton, W. A. *et al.* Anisotropic Thermal Expansion of Zirconium Diboride: An Energy-Dispersive X-Ray Diffraction Study. *J. Ceram.* **2016**, 1–5 (2016). DOI:10.1155/2016/8346563.

234. Beeler, B., Mahbuba, K., Wang, Y. & Jokisaari, A. Determination of Thermal Expansion, Defect Formation Energy, and Defect-Induced Strain of α-U Via ab Initio Molecular Dynamics. *Front. Mater.* **8**, (2021). DOI:10.3389/fmats.2021.661387.

235. Chung, T. E. & Davies, T. J. The superplastic creep of uranium dioxide. *J. Nucl. Mater.* **79**, 143–153 (1979). DOI:10.1016/0022-3115(79)90441-0.

236. Masuki, R., Nomoto, T., Arita, R. & Tadano, T. Anharmonic Grüneisen theory based on self-

consistent phonon theory: Impact of phonon-phonon interactions neglected in the quasiharmonic theory. *Phys. Rev. B* **105**, 064112 (2022). DOI:10.1103/PhysRevB.105.064112.

237. Williamson, R. L. *et al.* Multidimensional multiphysics simulation of nuclear fuel behavior. *J. Nucl. Mater.* **423**, 149–163 (2012). DOI:https://doi.org/10.1016/j.jnucmat.2012.01.012.
238. Tekce, H. S., Kumlutas, D. & Tavman, I. H. Effect of Particle Shape on Thermal Conductivity of Copper Reinforced Polymer Composites. *J. Reinf. Plast. Compos.* **26**, 113–121 (2007). DOI:10.1177/0731684407072522.
239. Petti, D. A., Buongiorno, J., Maki, J. T., Hobbins, R. R. & Miller, G. K. Key differences in the fabrication, irradiation and high temperature accident testing of US and German TRISO-coated particle fuel, and their implications on fuel performance. *Nucl. Eng. Des.* **222**, 281–297 (2003). DOI:10.1016/S0029-5493(03)00033-5.
240. Nan, W., Ghadiri, M. & Wang, Y. Analysis of powder rheometry of FT4: Effect of particle shape. *Chem. Eng. Sci.* **173**, 374–383 (2017). DOI:10.1016/j.ces.2017.08.004.
241. Mella, R. & Wenman, M. R. Modelling explicit fracture of nuclear fuel pellets using peridynamics. *J. Nucl. Mater.* **467**, 58–67 (2015). DOI:10.1016/j.jnucmat.2015.08.037.
242. Turner, J. & Abram, T. Steam performance of UB_2/U_3Si_2 composite fuel pellets, compared to U_3Si_2 reference behaviour. *J. Nucl. Mater.* **529**, 151919 (2020). DOI:10.1016/j.jnucmat.2019.151919.
243. Watkins, J. K., Butt, D. P. & Jaques, B. J. Microstructural degradation of UN and UN-UO_2 composites in hydrothermal oxidation conditions. *J. Nucl. Mater.* **518**, 30–40 (2019). DOI:10.1016/j.jnucmat.2019.02.027.
244. Wu, L., Liu, N., Qin, Z. & Shoesmith, D. W. Modeling the Radiolytic Corrosion of Fractured Nuclear Fuel under Permanent Disposal Conditions. *J. Electrochem. Soc.* **161**, E3259–E3266 (2014). DOI:10.1149/2.032408jes.
245. Sattonnay, G., Vincent, L., Garrido, F. & Thomé, L. Xenon versus helium behavior in UO_2 single crystals: A TEM investigation. *J. Nucl. Mater.* **355**, 131–135 (2006). DOI:10.1016/j.jnucmat.2006.04.013.
246. Rondinella, V. V. & Wiss, T. The high burn-up structure in nuclear fuel. *Mater. Today* **13**, 24–32 (2010). DOI:10.1016/S1369-7021(10)70221-2.
247. Li, T. *et al.* Preliminary Investigation of Preparing High Burn-Up Structure in Nuclear Fuel by Flash Sintering Using CeO_2 as a Surrogate. *Acta Metall. Sin. (English Lett.* **34**, 1758–1768 (2021). DOI:10.1007/s40195-021-01230-4.

248. Parant, P., Picart, S., Lhuissier, P. & Martin, C. L. Strength of porous oxide microspheres: The role of internal porosity and defects. *J. Eur. Ceram. Soc.* **40**, 1613–1619 (2020). DOI:10.1016/j.jeurceramsoc.2019.11.075.

249. Parker, H. M. O. D. & Joyce, M. J. The use of ionising radiation to image nuclear fuel: A review. *Progress in Nuclear Energy* vol. 85 297–318 (2015). DOI:10.1016/j.pnucene.2015.06.006.

250. Degueldre, C., Bertsch, J. & Martin, M. Post irradiation examination of nuclear fuel: Toward a complete analysis. *Prog. Nucl. Energy* **92**, 242–253 (2016). DOI:10.1016/j.pnucene.2016.03.025.

251. Abdollahi, M. & Ahmadi, S. J. Application of ideal temperature gradient technology to optimize the chemical exchange and distillation process of boron isotopes separation by $(CH_3)_2O$-BF_3 complex. *Chem. Eng. Process. Process Intensif.* **76**, 26–32 (2014). DOI:https://doi.org/10.1016/j.cep.2013.12.002.

252. Naefe, P. & Zimmer, E. Preparation of Uranium Kernels By an External Gelation Process. *Nucl Technol* **42**, 163–171 (1979). DOI:10.13182/NT79-A32147.

253. Mistarihi, Q. M. *et al.* Fabrication of oxide pellets containing lumped Gd_2O_3 using Y_2O_3-stabilized ZrO_2 for burnable absorber fuel applications. *Int. J. Energy Res.* **42**, 2141–2151 (2018). DOI:10.1002/er.3995.

254. Greil, P. Near Net Shape Manufacturing of Polymer Derived Ceramics. *J. Eur. Ceram. Soc.* **18**, 1905–1914 (1998). DOI:10.1016/S0955-2219(98)00129-0.

255. Nishide, H., Oki, N. & Tsuchida, E. Complexation of poly(acrylic acid)s with uranyl ion. *Eur. Polym. J.* **18**, 799–802 (1982). DOI:https://doi.org/10.1016/0014-3057(82)90149-5.

256. Qiusheng, Z., Xiaoyan, L., Jin, Q., Jing, W. & Xuegang, L. Porous zirconium alginate beads adsorbent for fluoride adsorption from aqueous solutions. *RSC Adv.* **5**, 2100–2112 (2015). DOI:10.1039/C4RA12036A.

257. Li, X. *et al.* Novel magnetic beads based on sodium alginate gel crosslinked by zirconium (IV) and their effective removal for Pb^{2+} in aqueous solutions by using a batch and continuous systems. *Bioresour. Technol.* **142**, 611–619 (2013). DOI:10.1016/j.biortech.2013.05.081.

258. Wang, H.-H., Shyr, T.-W. & Hu, M.-S. The elastic property of polyvinyl alcohol gel with boric acid as a crosslinking agent. *J. Appl. Polym. Sci.* **74**, 3046–3052 (1999). DOI:https://doi.org/10.1002/(SICI)1097-4628(19991220)74:13<3046::AID-APP6>3.0.CO;2-1.

259. Ji, H. *et al.* Low-temperature synthesis of ZrB_2 nano-powders using a sorbitol modified sol–gel processing route. *Adv. Powder Technol.* **25**, 910–915 (2014). DOI:https://doi.org/10.1016/j.apt.2014.01.005.

260. La Lumia, F. *et al.* Dense and homogeneous MOX fuel pellets manufactured using the freeze granulation route. *J. Am. Ceram. Soc.* **103**, 3020–3029 (2020). DOI:10.1111/jace.17005.

261. Stunda-Zujeva, A., Irbe, Z. & Berzina-Cimdina, L. Controlling the morphology of ceramic and composite powders obtained via spray drying – A review. *Ceram. Int.* **43**, 11543–11551 (2017). DOI:10.1016/j.ceramint.2017.05.023.

262. Liu, R., Liu, M., Chang, J., Shao, Y. & Liu, B. An improved design of TRISO particle with porous SiC inner layer by fluidized bed-chemical vapor deposition. *J. Nucl. Mater.* **467**, 917–926 (2015). DOI:10.1016/j.jnucmat.2015.10.055.

263. Oxley, J. H. & Blocher, J. M. Coating Uranium Dioxide Powders with Metallic Tungsten. **51**, (1959). DOI:10.1021/ie50599a045.

264. Lai, K. K. & Lamb, H. H. Tungsten chemical vapor deposition using tungsten hexacarbonyl: microstructure of as-deposited and annealed films. *Thin Solid Films* **370**, 114–121 (2000). DOI:https://doi.org/10.1016/S0040-6090(00)00943-3.

265. Wilken, T. R., Morcom, W. R., Wert, C. A. & Woodhouse, J. B. Reduction of tungsten oxide to tungsten metal. *Metall. Trans. B* **7**, 589–597 (1976).

266. Gurinsky, D. H. & Samuel, S. Coating uranium from carbonyls. U.S. Patent Application No. 2,894,320 (1949).

267. Abate, D. G. & Amato, I. Sintered nuclear fuel containing molybdenum coated gadolinium oxide microspheres. U.S. Patent Application No. 00885524A (1973).

268. Ou, N. C., Su, X., Bock, D. C. & McElwee-White, L. Precursors for chemical vapor deposition of tungsten oxide and molybdenum oxide. *Coord. Chem. Rev.* **421**, 213459 (2020). DOI:https://doi.org/10.1016/j.ccr.2020.213459.

269. Latifi, M. & Chaouki, J. A novel induction heating fluidized bed reactor: Its design and applications in high temperature screening tests with solid feedstocks and prediction of defluidization state. *AIChE J.* **61**, 1507–1523 (2015). DOI:https://doi.org/10.1002/aic.14749.

270. Idakiev, V. V., Lazarova, P. V., Bück, A., Tsotsas, E. & Mörl, L. Inductive heating of fluidized beds: Drying of particulate solids. *Powder Technol.* **306**, 26–33 (2017). DOI:10.1016/j.powtec.2016.11.011.

271. Zhou, Y., Shi, Q., Huang, Z., Wang, J. & Yang, Y. Particle agglomeration and control of gas-solid fluidized bed reactor with liquid bridge and solid bridge coupling actions. *Chem. Eng.*

J. **330**, 840–851 (2017). DOI:10.1016/j.cej.2017.07.117.

272. Di Kang, Nadim, A. & Chugunova, M. Marangoni effects on a thin liquid film coating a sphere with axial or radial thermal gradients. *Phys. Fluids* **29**, (2017). DOI:10.1063/1.4991580.
273. Hay, J. O. & Grodek, R. J. Process for converting ammonium paratungstate to a more soluble form. U.S. Patent application No. 536274A (1969).
274. Hunyadi, D., Sajó, I. & Szilágyi, I. M. Structure and thermal decomposition of ammonium metatungstate. *J. Therm. Anal. Calorim.* **116**, 329–337 (2014). DOI:10.1007/s10973-013-3586-1.
275. Murau, P. C. Dissolution of tungsten by hydrogen peroxide. *Anal. Chem.* **33**, 1125–1126 (1961).
276. Smith, K. & Dean, J. R. Investigation into the spontaneous dissolution of tungsten using acid media. *Analyst* **118**, 1445–1447 (1993).
277. Volgin, V. M., Kabanova, T. B. & Davydov, A. D. Theoretical analysis of mass transfer during anodic dissolution of tungsten rotating disk electrode in alkaline solutions. *Electrochim. Acta* **336**, 135705 (2020). DOI:https://doi.org/10.1016/j.electacta.2020.135705.
278. Chase, M. W., Davies, C. A., Downey, J. R., Frurip, D. J. & McDonald, R. A. J. Phys. Chem. Ref. Data. *JANAF Thermochem. Tables* **4**, (1998).
279. Mirković, D., Gröbner, J., Schmid-Fetzer, R., Fabrichnaya, O. & Lukas, H. L. Experimental study and thermodynamic re-assessment of the Al-B system. *J. Alloys Compd.* **384**, 168–174 (2004). DOI:10.1016/J.JALLCOM.2004.04.100.
280. Butland, A. T. D. & Maddison, R. J. The specific heat of graphite: An evaluation of measurements. *J. Nucl. Mater.* **49**, 45–56 (1973). DOI:10.1016/0022-3115(73)90060-3.
281. Yamada, K., Ohtani, H. & Hasebe, M. Thermodynamic analysis of the Fe-Cr-B ternary system. *High Temp. Mater. Process.* **27**, 269–283 (2008). DOI:10.1515/HTMP.2008.27.4.269/.
282. Wagman, D. D. *et al. The NBS tables of chemical thermodynamic properties. Selected values for inorganic and C1 and C2 organic substances in SI units*. (1982).
283. Chong, X., Jiang, Y., Zhou, R. & Feng, J. Stability, chemical bonding behavior, elastic properties and lattice thermal conductivity of molybdenum and tungsten borides under hydrostatic pressure. *Ceram. Int.* **42**, 2117–2132 (2016). DOI:10.1016/J.CERAMINT.2015.09.105.
284. Lavut, E. G., Chelovskaya, N. V. & Kashireninov, O. E. Direct determination of the enthalpy

of formation of MoB in synthesis from simple substances in an SHS system. *J. Eng. Phys. Thermophys.* **65**, 971–973 (1993). DOI:10.1007/BF00862768.

285. Colinet, C. & Tedenac, J. C. Enthalpies of Formation of Transition Metal Diborides: A First Principles Study. *Cryst. 2015, Vol. 5, Pages 562-582* **5**, 562–582 (2015). DOI:10.3390/CRYST5040562.
286. Guillaumont, R. *Update on the chemical thermodynamics of uranium, neptunium, plutonium, americium and technetium*. vol. 5 (Elsevier).
287. Brady, P., Chand, K., Warren, D. & Vandersall, J. *Assessment of UF_6 Equation of State*. https://www.osti.gov/servlets/purl/948653/ (2009) doi:10.2172/948653. DOI:10.2172/948653.
288. Chevalier, P. Y., Fischer, E. & Cheynet, B. Thermodynamic modelling of the N-U system. *J. Nucl. Mater.* **280**, 136–150 (2000). DOI:10.1016/S0022-3115(00)00043-X.
289. Guo, X. *et al.* Enthalpy of formation of U_3Si_2: A high-temperature drop calorimetry study. *J. Nucl. Mater.* **507**, 44–49 (2018). DOI:10.1016/J.JNUCMAT.2018.04.032.
290. Blinder, A. V. & Bolgar, A. S. Thermodynamic properties of tungsten borides in a broad temperature range. *TVT* **28**, 501–505 (1990).